X-ray properties and activity of cool stars
The view of XMM-Newton

Dissertation
zur Erlangung des Doktorgrades
des Fachbereichs Physik
der Universität Hamburg

vorgelegt von

Jan Robrade

aus Krefeld

Hamburg
2005

Gutachter der Dissertation:	Prof. Dr. J.H.M.M. Schmitt
	Prof. Dr. S. Sciortino
Gutachter der Disputation:	Prof. Dr. J.H.M.M. Schmitt
	Prof. Dr. P.H. Hauschildt
Datum der Disputation:	17. 02. 2006
Vorsitzender des Prüfungsausschusses:	Dr. habil. F.-J. Zickgraf
Vorsitzender des Promotionsausschusses:	Prof. Dr. G. Huber
Dekan des Fachbereichs Physik:	Prof. Dr. G. Huber

Zusammenfassung

Die Entdeckung und Untersuchung von Sonnenflecken und der Korona der Sonne im sichtbaren Licht und später bei höheren Energien eröffnete ein neues Feld der Astronomie. Die Entstehung dieser Strukturen ist eng mit der Existenz vom starken Magnetfeldern verknüpft, welche durch Dynamoprozesse im Inneren der Sonne erzeugt werden. Veränderliche magnetischen Strukturen sind mit einer ganzen Reihe von Erscheinungen verbunden, welche als solare bzw. stellare Aktivität bezeichnet werden. Die sehr hohen Temperaturen der koronalen Plasmen ermöglichen das Studium von stellarer Aktivität und der zugrunde liegenden Physik insbesondere durch Untersuchung ihrer Röntgenstrahlung. Da kühle Sterne einen vergleichbaren inneren Aufbau wie die Sonne besitzen und ihre Röntgenemission ebenfalls mit magnetischen Prozessen verknüpft ist, können ihre Aktivitätsphänomene ähnlich denen der Sonne beschrieben werden. Allerdings übersteigt das Ausmaß stellarer Aktivität das solare Niveau um das bis zu tausendfache. Da eine räumliche Auflösung von koronalen Strukturen bisher nur auf der Sonne möglich ist, basieren die Erkenntnisse über stellare Aktivität hauptsächlich auf der Untersuchung von Leuchtkräften, Lichtkurven und Spektren.

Mit den neuen Röntgensatelliten wie z.B. XMM-Newton, welcher eine hohe Empfindlichkeit sowie eine hohe spektrale Auflösung besitzt, wurde die Untersuchung von Sternen in diesen Energiebereich mit bisher unbekannter Präzision möglich. Diese Arbeit beschäftigt sich mit der Aktivität von kühlen Sternen und beruht auf Daten, welche mit den Instrumenten an Bord von XMM-Newton aufgenommen wurden. Verschiedene Aspekte der stellaren Röntgenemission in unterschiedlichen Sterntypen werden untersucht.

Nach einer Einführung werden im ersten Teil dieser Arbeit werden aktive M Sterne besprochen. Diese recht kühlen und massearmen Sterne sind starke und variable Röntgenquellen mit extremen Eigenschaften ihrer Koronen. So sind die beobachteten koronalen Temperaturen wesentlich höher als bei der Sonne, der relative Anteil der im Röntgenbereich abgestrahlten Energie übertrifft den anderer Arten kühler Sterne oft deutlich und starke Energieausbrüche werden regelmäßig beobachtet. Die Röntgeneigenschaften einer Auswahl von aktiven M Sternen werden in unterschiedlichen Aktivitätsphasen untersucht, hierzu gehören die Doppelsternsysteme AT Mic und EQ Peg sowie die Einzelsterne AD Leo und EV Lac. Obwohl sich ihr Aktivitätsniveau deutlich unterscheidet, sind wesentliche Eigenschaften ihrer Koronen vergleichbar.

Im zweiten Teil wird die Röntgenemission von jungen Sternen behandelt, wobei der Schwerpunkt auf klassischen T Tauri Sternen liegt. Diese sehr jungen Sterne haben ihre Entwicklung zum Hauptreihenstern noch nicht vollständig abgeschlossen, sind ebenfalls als starke Röntgenstrahler bekannt und besitzen eine den Stern umgebende Scheibe aus Gas und Staub. Zusätzlich zu koronaler Aktivität kann ihre Röntgenstrahlung daher auch durch magnetische Akkretion des den Stern umgebenden Materials, welche zu starken Schocks auf der Sternoberfläche führt, erzeugt werden. Die Entstehungsmechanismen der Röntgenstrahlung werden in klassischen T Tauri Sternen unterschiedlichen Alters und spektraler Eigenschaften anhand der Sterne BP Tau, CR Cha, SU Aur und TW Hya untersucht. Akkretionsschocks und koronale Aktivität tragen zu der beobachteten Röntgenstrahlung bei, allerdings unterscheidet sich die Bedeutung der beiden Prozesse in den verschiedenen Objekten deutlich. Es wird weiterhin der Nachweis von Beta Pictoris im Röntgenlicht berichtet und deren mögliche Erzeugungsmechanismen diskutiert.

Der dritte Teil dieser Arbeit beschäftigt sich mit älteren und nur mäßig aktiven, sonnenähnlichen Sternen und ist insbesondere der Untersuchung von zyklischem Aktivitätsverhalten gewidmet. Einer der wesentlichen Merkmale der Sonnenaktivität ist ihr 11-jähriger Zyklus, welcher mit seinen Einfluss auf das Erdklima von wesentlicher Bedeutung ist. Koronale Aktivitätszyklen von Sternen sind dagegen nur bei wenigen Objekte bekannt, da entsprechende Langzeitbeobachtungen in Röntgenbereich fehlen. Die Sternensysteme Alpha Centauri A/B und 61 Cygni A/B wurden über Jahre regelmäßig mit XMM-Newton beobachtet. Die beobachtete Veränderlichkeit der Röntgenleuchtkraft und damit verbundene Veränderungen der koronalen Eigenschaften werden untersucht. Anzeichen für möglich koronale Aktivitätszyklen, insbesondere des solaren Zwillingssternes Alpha Cen A, werden in dieser Arbeit vorgestellt.

Abstract

The discovery and succeeding detailed studies of sunspots and the solar corona first in visible light and later at higher energies gave birth to a new field in astronomy. The formation of a corona around the Sun and other cool stars is directly linked to the existence of strong magnetic fields, which are generated by dynamo processes in their interior. Magnetic fields and its changing configurations are responsible for a variety of phenomena, summarised as solar or stellar activity. The high temperatures of the coronal plasma make the X-ray domain ideal to investigate stellar activity and its underlying physics. Since cool stars have in common a comparable internal structure and their X-ray emission and activity is likewise related to magnetic processes, they are described in a similar way and solar results can often transfered into the stellar context. The levels of activity observed in stars exceed the solar one by up to a factor of thousand, but only on the Sun coronal structures can be spatially resolved. Investigation of stellar activity is therefore based on the study of light curves, X-ray brightness and especially on spectral analysis.

With the advent of the new generation X-ray missions like XMM-Newton and its ability to provide high sensitivity and high spectral resolution, the study of the energetic phenomena on other stars was put on a new level. This thesis deals with the activity of cool stars and is based on data obtained with the instruments onboard XMM-Newton. Several aspects of stellar X-ray emission are investigated in different types of cool stars. These include among others active M dwarfs, classical T Tauri stars and solar-like stars.

After introducing the topic, in the first part of this thesis the coronal activity of active M dwarfs is investigated. These low-mass stars at the cool end of the main sequence are strong and variable X-ray sources with extreme coronal conditions. Coronal temperatures are much higher than on the Sun, the relative amount of energy emitted in X-rays exceeds that of most of the others cool star and flaring is observed on a regular basis. Their coronal properties are investigated for different phases of activity for a sample of mid M dwarfs, which includes the binary systems AT Mic and EQ Peg as well as in the single stars AD Leo and EV Lac. Despite the observed different level of activity, many coronal properties of the sample stars are found to be comparable.

The second part of this thesis deals with the X-ray emission from very young stars, mainly from classical T Tauri stars. These are the pre-main sequence equivalents of cool stars which are in the process of evolving towards the main sequence. Classical T Tauri stars still possess a disk with significant amounts of matter and are actively accreting. They are strong X-ray sources and additionally to coronal activity X-rays may be generated by magnetically funneled accretion, a mechanism that leads to strong shocks at the stellar surface. High and medium resolution spectra from several classical T Tauri stars are studied to investigate their X-ray generation mechanisms and plasma properties. The sample contains objects of various age, namely BP Tau, CR Cha, SU Aur and TW Hya, which exhibit quite different X-ray properties. Accretion shocks and coronal activity contribute to the observed X-ray emission, whereas the fraction for each process differs significantly between the individual objects. In the context of young stellar systems also the X-ray detection of Beta Pictoris is presented and implications on possible X-ray generating mechanisms are discussed.

Part three of this thesis deals with older and only moderately active solar-like stars and is mainly devoted to the investigation of cyclic activity behaviour. The 11-year cycle is one of the characteristic features of the Suns activity and is of great importance, since solar activity also influences terrestial climate conditions. The indications for coronal activity cycles on stars are still limited to very few objects due to nonexistent long-term X-ray monitoring data. The stellar systems Alpha Centauri A/B and 61 Cygni A/B were monitored over several years with XMM-Newton. The observed variations in their X-ray luminosity and related changes of coronal properties are studied. Indications for cyclic activity, especially of the solar twin Alpha Cen A, are presented in this work.

Contents

Chapter 1

Introduction

1.1 General overview

1.1.1 History of X-ray astronomy

The progress in X-ray astronomy is, like the progress in astronomy and other sciences, often linked to the invention of new technologies which allow new methods for studying physical properties of the universe or of certain objects within. While ancient astronomical observations started several millenia ago and modern astronomy began with the invention of the telescope in the 17th century, X-ray astronomy is in comparison a fairly young, but fast evolving field of science.

On the evening of November 8, 1895 Wilhelm Conrad Röntgen discovered X-rays and on this account he got the first Nobel Price in Physics in 1901. Because X-rays are absorbed by the Earth's atmosphere, it was not until the invention of the rocket that astronomers could observe the the sky at these wavelengths. In the late 1940s the Sun, whose outer atmosphere was already thought to be extremely hot and therefore should emit radiation at high energies, was detected in X-rays with the help of captured V2 rockets. In June 1962 a rocket equipped with rotatable Geiger counters was launched and flew at a height of 220 km for a few minutes above the Earth's atmosphere. It was intended to detect X-rays from the Moon, but didn't see the Moon at all. Instead, beside a dim glow from the total sky, it detected a bright X-ray source in the constellation Scorpius at a position where no bright star exists. Now known as Sco X-1, it was the first X-ray source that was detected outside the solar system – X-ray astronomy was born. This event triggered its further development and Riccardo Giacconi, a leading scientist of these and further X-ray missions, was awarded with the Nobel Price in
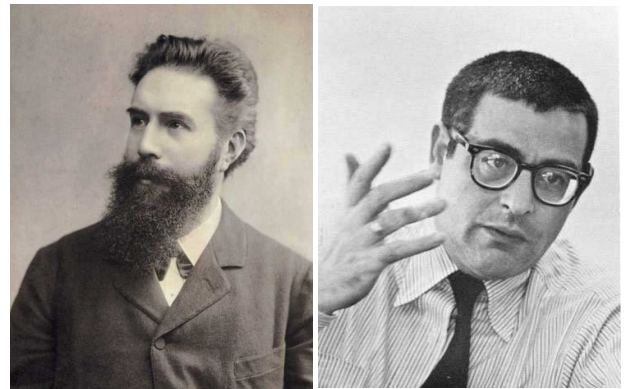
Figure 1.1: Nobel Price winners. Left: Röntgen (discovery of X-rays), right: Giacconi (X-ray astronomy)

Physics in 2002 for his pioneering work.

With the advent of rockets and later satellites one condition for X-ray astronomy was fulfilled and detectors could be brought above the Earth's atmosphere; but some further problems had to be solved. X-rays cannot be focused like optical light with lenses or mirrors, since X-rays will be rather absorbed than reflected. The invention of the Wolter-telescope in the 1950s by H. Wolter, who actually wanted to build an X-ray microscope, allowed the focusing of X-rays. In the classical Walter type-1 design that is used in X-ray telescopes, this is accomplished by two successive grazing-incidence reflections on a parabolic and a hyperbolic shaped metal surface. The last piece on the technical side was the development of the X-ray detectors. Very early missions used Geiger-counter or proportional chambers, sometimes combined with collimators. A proportional chamber is filled with a counting gas like argon and not only detects incoming X-rays, but also measures its energy. Later a technical enhanced version containing wire-grid layers, known as position

sensitive proportional chamber was commonly used. It allows the measurement of three important characteristics of the incoming X-ray photons, i.e time, energy and position. Likewise some mission were also equipped with solid state and crystal detectors. Another type of detector consists of micro-channel plates, which allow to very accurately determine the position of incoming X-rays. It has the disadvantage of having no intrinsic spectral resolution, but in combination with a filter or a refraction device spectral information can be extracted. X-rays were refracted with Bragg-crystals in early missions, which were followed by transmission and reflection gratings. Another big step was the invention of X-ray sensitive CCD detectors, which is frequently used nowadays. It likewise allows the simultaneous determination of the position, time and energy of incoming X-ray photons. A combination of a modern detector, i.e. an X-ray CCD or micro-channel plate, with a grating provides the high resolution X-ray spectroscopy of today's X-ray missions.

1.1.2 Cool stars

Stars are classified according to their position in the Hertzsprung-Russell diagram (HDR), as shown in Fig. 1.2. The HRD is based on spectral classifications and each star is assigned to a spectral type according to its surface temperature and to a luminosity class according to its brightness. In the HRD cool stars include the spectral types F, G, K and M, further subdivided by appending a number from $0-9$. Most stars are located on the main sequence, which corresponds to luminosity class V, but the term dwarf is as well commonly used. Beside the spectral type according to the HRD, a variety of other termini are in use for the different kinds of stars. Cool stars exhibit surface temperatures from around $7500\,\mathrm{K}$ for early F stars down to $2500\,\mathrm{K}$ for late M stars. Historically $F-M$ stars, sometimes only K and M stars, are often named late-type stars and with masses ranging from around $2\,\mathrm{M}_\odot$ for early F stars down to $0.1\,\mathrm{M}_\odot$ for late M stars, they are also known as low-mass stars. Since their internal structure is comparable to the Sun, they are also called solar-like stars, but this term is not, as well as the term solar analog, strictly linked to spectral classifications in the HRD.

Activity is commonly found among cool dwarf stars and likewise on the Sun, a typical G2V star with
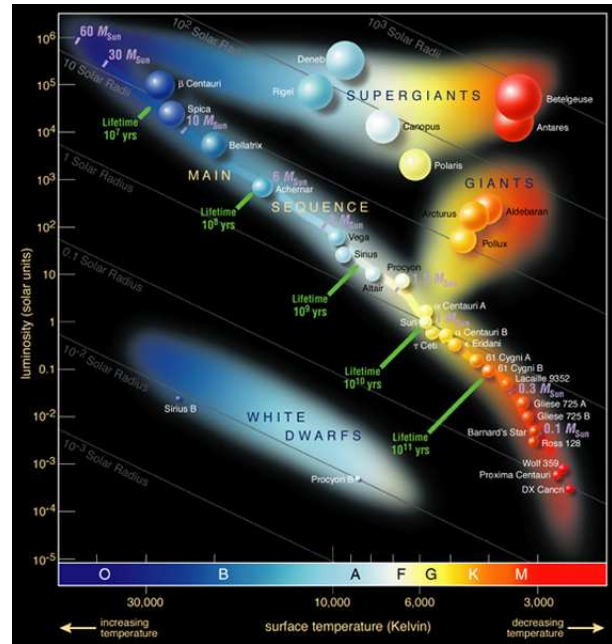
Figure 1.2: The Hertzsprung-Russell diagram. The cool stars $(F-M)$ discussed in this work can be found at the right part of the main sequence.

an age of $4.5\,\mathrm{Gyr}$. This activity is related to the generation of magnetic fields in the stellar interior and it creates a variety of dynamic phenomena that are well observable in the domain of high energy radiation. The X-ray emission of a cool main sequence star is produced by very hot matter in the outer stellar atmosphere interacting with the magnetic field, the so called corona. Very young stars are known as pre-main sequence stars, they are are still contracting and are therefore located slightly above the main sequence. Young cool stars are named after their prototype T Tauri stars. They likewise exhibit coronal activity, but the presence of an accretion disk may modify their X-ray properties. Further above the main sequence the evolved cool giants can be found. Giants are, like hot stars whose X-ray emission is not related to the presence of a corona but connected to stellar winds and shocks, not discussed in this work.

1.1.3 Solar & stellar X-ray missions

After several rocket flights and orbiting observatories an important progress in solar studies was made in 1973 with the Skylab mission. It provided amongst others X-ray imaging and spectroscopy of the Sun,

that revealed the structured and dynamic appearance of the solar corona and features like coronal holes, active regions or flares could be studied. Several dedicated missions followed, which were either focussed on observing the Sun or on observing other astronomical objects. Major succeeding solar missions were Yohkoh (jp. Sunbeam, 1991 – 2001), which observed solar activity nearly over a complete solar cycle in X-rays, the SOHO (Solar and Heliospheric Observatory, 1995) satellite equipped with the EIT (Extreme ultraviolet Imaging Telescope) and other instruments and TRACE (Transition Region and Coronal Explorer, 1998). They explored the activity of the Sun in numerous aspects and revealed more details of its complex and transient character.

Since the Sun is only one star out of billions, fundamental questions arise in this context. Are the properties observed for the Sun typical for cool stars in general? How does activity evolve with stellar age? What is the dependence on stellar mass or spectral type? What are the conditions in stellar coronae and how they are generated? How does stellar activity influence the process of planetary formation and evolution of life? All these questions can be addressed by observing the X-ray properties of stars with different age, mass, activity level and other relevant parameters.

The launch of the the first astronomical X-ray satellite Uhuru (swh. Freedom) in 1970 initiated the real space-age of X-ray astronomy. The first stellar X-ray source, the active binary Capella, was discovered again with a rocket flight in 1974 (Catura et al. 1975), but only a few stars were detected in X-rays until HEAO-1 (High Energy Astronomy Observatory, 1977 – 1979) observed and monitored large areas of the sky and detected further stellar X-ray sources, including several cool stars. An important missions contributing to the field of stellar coronal astronomy was *Einstein* (1978 – 1981), an imaging X-ray observatory equipped with different types of detectors. It discovered already hundreds of normal stars and demonstrated that X-ray emission is common for nearly all classes of stars. Later on, ROSAT (1990 – 1999) scanned the whole sky and discovered over 100.000 X-ray sources, including tens of thousands coronal sources. It also performed numerous pointed observations of stars. Accompanied and followed by missions like EXOSAT, ASCA, RXTE and
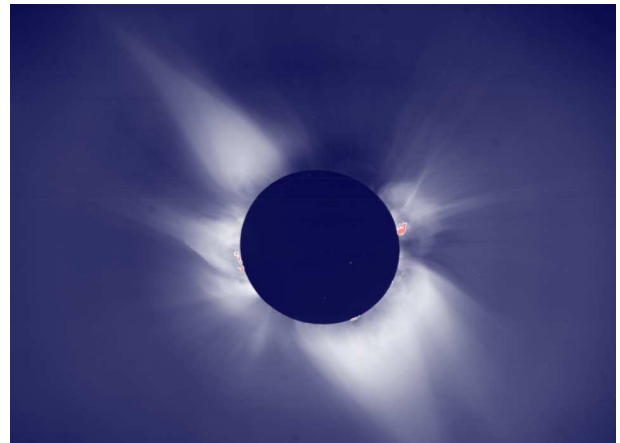
Figure 1.3: The corona is visible during a total solar eclipse, here observed from Hawaii in 1991.

BeppoSax, the launch of the technically enhanced, complementary designed, new generation X-ray missions *Chandra* (optimized for high spatial resolution) and XMM-Newton (optimized for high sensitivity) in 1999 set up promising opportunities for the further development of X-ray astronomy in the 20th century.

1.2 Magnetic activity of the Sun

In the following sections the progress in understanding the activity of the Sun and its application to coronal physics and cool stars in general is outlined. An introduction to solar coronal physics is e.g. given in Golub & Pasachoff (1997), a review of solar and stellar magnetic activity in Schrijver & Zwaan (2000).

1.2.1 The Sunspots and the photosphere

The investigation of stellar activity was limited to the Sun for centuries and the Sun is due to its vicinity still the best studied case. Sunspots, which are cooler and consequently darker than the photosphere, are the imprints of solar magnetic activity in the visible surface and therefore a good tracer for its respective activity level. Sunspots as a phenomenon were already known more than 2000 years ago and around 400 BC the Greek astronomer Meton speculated about the Sun – Earth connection based on sunspot observations. However, things changed and only with the invention of the telescope in the 17th century detailed studies of the Sun by Galilei re-

vealed again that its surface is not uniform but features dark spots, the sunspots. Observations continued and soon it was discovered that sunspots evolve and move along the visible surface due to the Sun's rotation. Long-term observations leaded to the discovery of the 11-year solar cycle around 1850 by H. Schwabe, whereas number and latitude of the sunspots follow a regular patter; the recent sunspot history is shown in Fig. 1.4. However, the cycle length of 11 years is only a mean and there are variations both in the length and amplitude of the solar cycle and even longer periods with allover stronger or weaker activity are known.
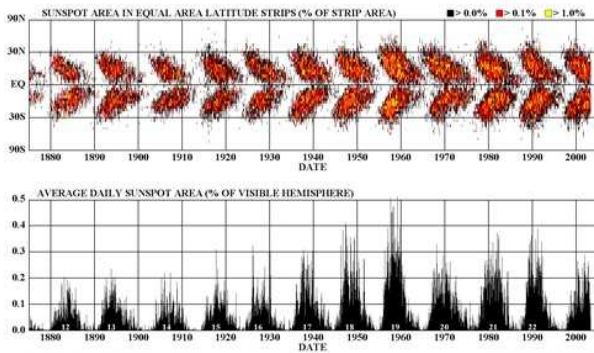
Figure 1.4: The solar activity cycle over the last 130 years. Top: The butterfly diagram, showing the location of sunspots. Bottom: Sunspot number which are an indicator for the respective activity of the Sun. See Fig. 1.11 for an X-ray view of the solar cycle.

Due to the vicinity of the Sun these variations may also affect the Earth as part of the planetary system. There is strong evidence that solar activity influences the Earth's atmosphere and therefore terrestial climate conditions, see e.g Hoyt and Schatten (1997) for a review of this field. Most famous is the so-called Maunder-Minimum which coincides with a little ice-age, a period of 70 years around the second half of the 17th century when solar activity was very low and only few sunspots where observed. Periods of stronger activity are supposed to be related to global warming, i.e. in the Medieval Maximum, as deduced from cosmogenic isotopes (Usoskin et al. 2004) whose production correlates with solar activity.

A great step further in understanding sunspots was made in the early 20th century by G.E. Hale,
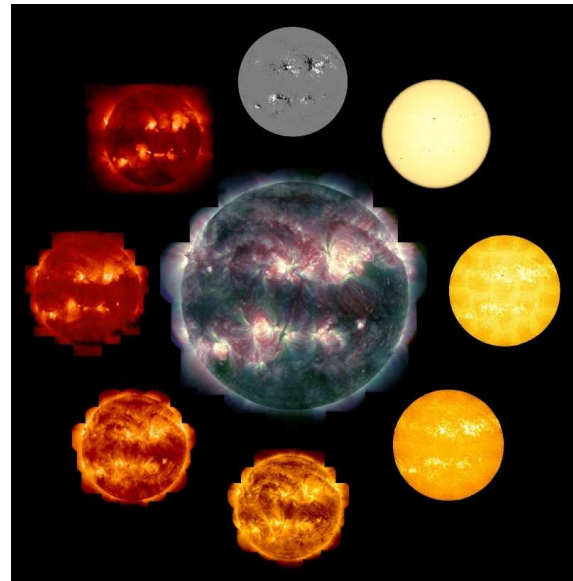
Figure 1.5: Views of the Sun as observed with SOHO, TRACE and Yohkoh. Central image: composite mosaic of the solar corona from TRACE, green (171 Å / 1 MK), blue (195 Å / 1.5 MK) and red (284 Å / 2 MK). Surrounding images, clockwise starting from the top: SOHO/MDI magnetic map, white light, TRACE (1700 Å continuum, Ly α, 171 Å, 195 Å, 284 Å, Yohkoh/SXT (0.25 − 4.0 keV X-ray). Image composed by Joe Covington.

who discovered by spectroscopic methods via the Zeeman effect, that strong magnetic fields exist in sunspots, revealing the magnetic origin of the activity phenomena. Sunspots usually come in east-west orientated pairs of opposite polarity, whereas the leading spot is slightly closer to the equator and has the polarity of the pole of the same hemisphere at the previous maximum. Larger sunspots appear in complex groups that are much bigger than the Earth and may last up to months. Current models predict sunspots to occur, when a bundle of magnetic flux tubes breaks through the photosphere and the strong magnetic fields interferes with the underlying convection zone and disturbs the upward motion of the hot plasma and therfore energy transport. Subsequent detailed studies revealed, that the magnetic field of the Sun changes polarity after each 11-year cycle, therfore a full magnetic cycle takes 22 years. The top image in Fig. 1.5 is a magnetic map of the Sun, showing the spatial correlation of the magnetic field with sunspots and active regions, displayed in

the other surrounding images.

1.2.2 Chromosphere and Corona

Magnetic activity influences the photosphere, but its impact on other layers of the atmosphere is much stronger. On the Sun these outer layers are usually outshone in optical light by the bright photosphere, but during total solar eclipses they become visible. Above the solar limb the chromosphere and fire-like structures known as prominences and spicules are visible and even further out up to several solar radii the corona (lat. crown) appears (see Fig.1.3). Prominences are large structures of cooler ($\sim 10^4$ K) and denser plasma embedded in the corona. They are supported by the magnetic field and hang above the solar surface; viewed on disk they are known as filaments. The chromosphere is a 2000 km thin layer above the photosphere where temperatures start to rise outwards followed by the even thinner transition region where temperature increases dramatically and finally the extremely hot ($\gtrsim 10^6$ K) corona that stretches out to several solar radii and dilutes into interstellar space. Total eclipses are rare and nowadays the light from the solar disk is blocked artificially by a coronagraph to allow permanent observations.

The investigation of these outer regions revealed several unknown spectral lines in the emitted light of the chromosphere and corona. Chromospheric spectra led even to the discovery of a new element. Helium, named after its site of discovery, was previously unknown on Earth. Contrary, the coronal lines are not related to unknown elements and its true explanation was found around 1940, when W. Grotian and B. Edlén showed that these lines originate from metastable levels in highly ionized iron and other metals. This discovery revealed that the corona must have temperatures above 10^6 K (1 MK), while the temperature of the photosphere is only 5800 K, setting up the puzzling question why the corona is so hot. On the other hand, only a small fraction of the energy output of the Sun is needed to heat the corona since the coronal plasma has a very low density. The coronal heating requires non-thermal processes and while details of the heating mechanism are still debated, a magnetic origin is supposed to be responsible. Beside various models involving magneto-hydrodynamic waves generated in the upper convection zone, another possibility is that the
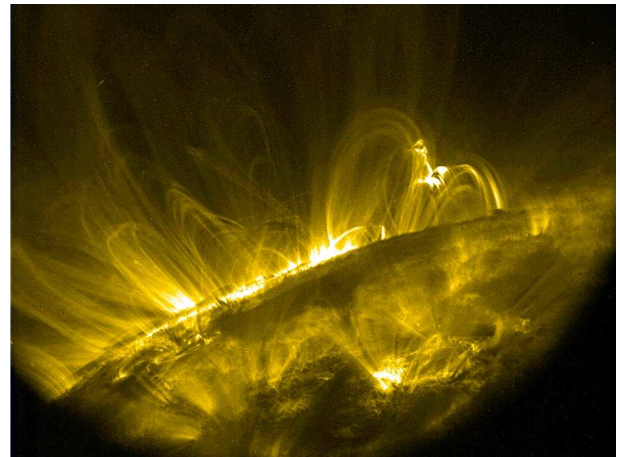
Figure 1.6: The highly structured corona of the Sun at roughly 1 million degree is visible in this TRACE image taken in the 171Å bandpass that covers a strong emission line of Fe IX.

coronal heating mechanism is due to magnetic reconnection events, analogue to the energy release in flares. In these models a large number of unresolved small flares, consequently called micro- and nano-flares, supplies a quasi-continuous energy input to the corona (Parker 1988).

The extreme temperatures of the outer stellar atmospheric layers and especially the corona cause the radiation of the hot plasma to be predominantly in the (E)UV and X-ray regime. X-ray observations of the Sun and other cool stars therefore contributed strongly to our knowledge of coronal physics. Again, Fig. 1.5 shows the Sun observed at different wavelength; the outer images give an impression of the appearance with increasing temperature, while the central image shows the corona in 'true' X-ray colours.

1.2.3 Coronal structures

The Sun is so far the only star where structures of the corona can be spatially resolved. Several complementary space missions were launched in the 1990s to explore the outer layers of the Sun, including Yohkoh, SOHO and TRACE. These missions observe(d) the Sun with high spatial resolution and allow the detailed study of solar coronal structures. These structures are dominated by their magnetic properties and therefore the Sun appears in X-rays very different from the optical, the regions of dark

Figure 1.7: Sequence of a solar flare event observed with TRACE (171Å), the field of view is 155000 km x 115000 km each. Left: A bright, flaring loop 15 min after onset of the flare. Later a post-flare loop system shows up that is growing and brightening. Middle: About 1.5 h later, tangled, high loops showing typical bright tops have appeared. Right: Nearly 3 h after flare onset the magnetic field configuration has simplified and the loops have started to cool and drain. Several smaller flares accompanied these event.

sunspots are visible as bright active regions. Other areas of the surface, like the undisturbed photosphere or the polar regions, where the magnetic field configuration is open, are X-ray dark.

Closer inspection of active regions exhibits very complex structures, an example of an active region at the solar limb is shown in Fig. 1.6. The hot coronal plasma is predominantly found in loops and loop arcades which evolve and change appearance constantly. Since the X-ray emitting plasma is confined in closed magnetic structures and co-evolves with the field, the configuration of the magnetic field is traced by the observed plasma. The universal appearance of loops in the corona asked for a global description. For solar loops a scaling law, assuming hydrostatic equilibrium, uniform heating and constant cross section, was developed by Rosner et al. (1978) (RTV-loops). It relates the product of loop (semi)-length and loop pressure with the maximum temperature at the loop-top. This simple loop model was extended with fine-tuning like variable cross-section, foot-point heating (Vesecky et al. 1979; Serio et al. 1981) and also successfully applied in the modelling of stellar coronae.

1.2.4   Flares, winds and transients

Beside long-term variations of the overall activity level like the solar cycle, important short-term, energetic events related to magnetic fields are flares. They involve only small areas of the surface and take place on timescales of minutes to hours. Flares come in a multitude and each one evolves a bit differently, an example is shown in Fig.1.7. However, in a general schema solar flares can be divided into two groups, compact flares and long-duration events, the so-called two-ribbon flares (Pallavicini et al. 1977). Compact flares are short, small, high-density and overall less energetic events, that are connected with the interaction of individual loops. Two-ribbon flares are related to larger scale magnetic field structures and complex loop arcades, they last longer, are larger with a greater height and are more energetic. A schematic illustration of such a flare is shown in Fig.1.8.

Energetic flares occur in active regions, when magnetic reconnection takes place in a discontinuity between nearby antiparallel fields, the so-called current sheet. The trigger of a flare event could be the rise of existing filaments or flux tubes, the photospheric motion of the loop foot points or the emergence of new magnetic field from the solar interior. In any case the previously more complex, sheared and twisted magnetic field ends up in a more simple geometry and stored magnetic energy is transformed into kinetic energy and heat. Hard X-rays are generated during flares when accelerated material impacts the chromosphere, while the soft X-ray emission is generated predominantly by the cooling of plasma in post-flare loops. Flares are accompanied by a significant X-ray brightening and a plasma temperature increase from the quiescent solar corona value of $\sim 2\,\mathrm{MK}$ to temperatures of up to $10\,\mathrm{MK}$. In the course of these events often mass is ejected by the

eruption, but heated chromospheric material evaporates and refills the corona.

Not all short duration transients are that violent, for example X-ray bright points appear in the corona only for several hours up to a day. Spatially located at small magnetically bipolar regions, they are a kind of miniature version of an active region. While their individual X-ray luminosity is small, a large number of hundreds up to thousand is present at the same time and summed they are a major contributor to the solar X-ray luminosity at cycle minimum.
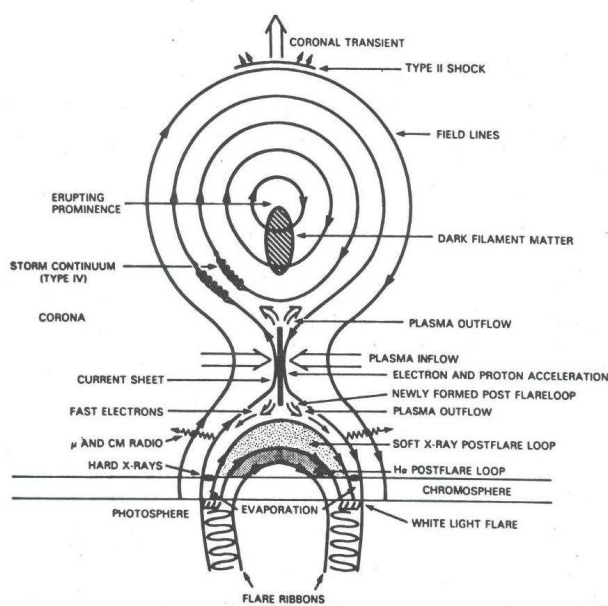
Figure 1.8: Cartoon of a reconnection event; the shown two-ribbon flares are the most energetic flares observed on the Sun (from Martens & Kuin 1989).

A large variety of transient phenomena and structures is present in the solar corona, whereas the timescale of lifetimes and variability covers an enormous range. Short-term variability like flares takes place on timescales from minutes to hours, the small X-ray bright points last for hours up to a few days, active regions may persist up to months and polar coronal holes are present for years, they only weaken or temporary disappear around cycle maximum.

Additionally solar activity is connected to the emission of high energy particles, the so-called solar wind, which escapes from coronal holes. It has a direct impact on terrestial conditions through the interaction of the Earth's atmosphere with particles emitted from the Sun. To describe its current properties nowadays the term 'space weather' is used. The solar wind escapes constantly from the polar coronal holes, but is particularly strong subsequent to flares, mass ejections and during activity maxima. When captured by the Earth's magnetic field it produces beautiful aurorae but is a threat to sensitive modern technology, especially when placed in space.

1.2.5 Dynamo models

The origin of the solar magnetic field is related to dynamo processes in the interior of the Sun. A solar dynamo model has not only to describe the existence of the magnetic field, but also the migration of sunspots and the polarity reversal. Its fundamental physics were developed by Parker (1955) and subsequently upgraded to account for the observed solar behaviour. The basic ingredients of a solar-type dynamo, the so-called $\alpha\Omega$-dynamo (see Parker 1979) are the interaction between inner radiative core and the twisting motions in the outer convective layers producing a poloidal field (α-effect) and the differential rotation, implying both latitudinal and radial component, that shears and amplifies the poloidal magnetic field to a toroidal magnetic field (ω-effect).

An empirical dynamo model was developed by Babcock (1961) to describe the dynamic aspects of the 22-year magnetic solar cycle. In the beginning a weak initial poloidal field is amplified and converted by differential rotation into a stronger toroidal field which is stored at the border of radiative core and outer convection zone. Magnetic buoyancy brings the flux tubes up through the convection zone if certain threshold values of the magnetic field are reached and they emerge from the surface and extent outwards to form the coronal structures and release magnetic energy via reconnection. Beside the change of fluid motions induced by the magnetic field in a way diminishing the dynamo efficiency, this mechanism is thought to be responsible that the amplification is stopped at some point. Sunspots appear first at high latitudes and migrate over a cycle towards the equator. In the Sun's convective interior the magnetic field, trapped in the up-and-down moving plasma, is twisted over the migration period by the Coriolis force and again turns into a weak but reversed poloidal field. A new cycle minimum has arrived and a 11-year solar activity cycle is completed.

The next 11-year cycle follows analogue, but with reversed magnetic polarity, completing a magnetic cycle. However, these models are simplifications and details are under debate since e.g. the fluid motions in the solar interior are not known precisely.

The conversion of rotational and internal kinetic energy into magnetic energy leads not only to coronal activity phenomena but also to magnetic braking. The star slows down and its rotational period increases with age. This diminishes its dynamo power and reduces the level of activity.

A solar-type dynamo is thought to be a common feature for cool main sequence stars, i.e for spectral classes F – M. Therefore their magnetic structures and coronal activity are in principle supposed to be similar to the solar case. However, the spectral classification is not related to dynamo properties but to surface temperature and late A stars are supposed to likewise possess a magnetic dynamo (Schmitt et al. 1985). Also somewhere in the mid to late M dwarf regime stars are thought to become fully convective. Likewise pre-main sequence stars are supposably deeply or even fully convective, but both types are very active. Completely different, e.g. a turbulent, dynamo mechanism may be at work or internal convection is suppressed somehow. Moreover, methods like Doppler imaging in the optical revealed very different surface features like large polar spots on active stars. Therefore the analogy with the Sun should not be overstretched and even different solar-type dynamos may lead to very different appearances of the coronae.

1.3   Stellar coronae in X-rays

The omnipresence of X-ray emission among cool stars and their dependence on rotation strongly suggests a magnetic character of their activity analogue to the Sun, whereas the amount of energy emitted in the X-ray regime differs strongly between individual stars and can be everything from a small side-effect up to an important contributor in the total energy budget. The similarity of stellar and solar X-ray emission and flares suggests similar basic physical mechanisms, with more active stars possessing more active regions and showing more frequent and larger flares. Extending the solar analogy, one might conclude that all these cool stars possess a solar-like
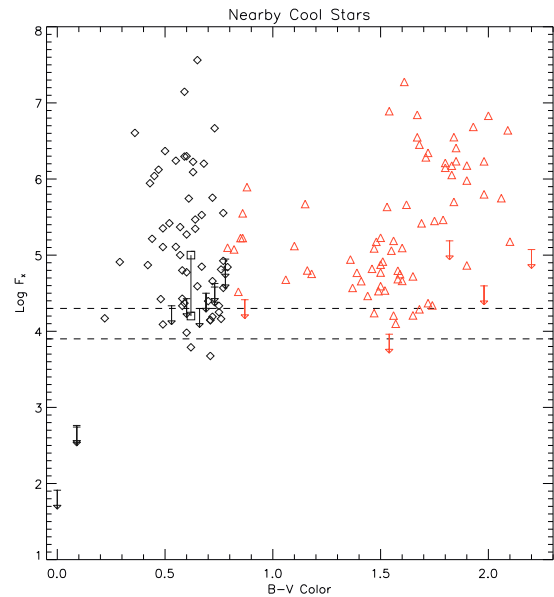
Figure 1.9: X-ray surface flux in $\mathrm{erg\,cm^{-2}\,s^{-1}}$ vs. B – V colour of a volume limited, complete sample of nearby stars as measured with ROSAT PSPC. F and G stars (diamonds), K and M stars (triangles) and A stars upper limits. The dashed lines indicate the flux from solar coronal holes, the squares denote the average Sun at minimum and maximum of the solar cycle. Original from Schmitt et al. (1997).

dynamo, a magnetically induced corona, solar-like loops and so on – but caution is advised. Stellar coronal astronomy covers a wide range of phenomena which cannot be covered completely in this introduction, for extensive reviews of the field see e.g. Favata & Micela (2003) or Güdel (2004). The aspects of stellar activity covered in this thesis are introduced in the following sections in more detail and its relation to the Sun is briefly mentioned. Further information on relevant topics is given in the respective chapters.

1.3.1   X-ray brightness & temperatures

The breakthrough in stellar X-ray astronomy arrived with the observations made with the *Einstein* satellite, which revealed that X-ray emitting stars can be found in nearly all spectral and luminosity classes (Vaiana et al. 1981). It was found, that the activity level of cool stars is not related to their bolometric luminosity, but is strongly correlated with stellar ro-

tation (Pallavicini et al. 1981), whereas faster rotating stars exhibit higher X-ray luminosities. The onset of X-ray emission related to stellar coronae and therefore magnetic activity begins around late A to early F stars, where stars begin to develop an outer convective envelope, with a rapid increase of the activity level towards cooler stars (Schmitt et al. 1985). Especially relatively cool, late-type stars were found to be quite active, revealing thermal X-ray emission from very hot plasma and exhibiting a bimodal coronal temperature structure, but with very different activity levels and temperatures (Schmitt et al. 1990). Flares were also commonly observed on other cool stars and many share common properties with solar ones while others have no solar counterparts, but they are thought to be likewise caused by magnetic energy release. The frequency and energy release of flaring correlates again with the stellar activity level. The RASS (ROSAT All Sky Survey) increased the number of known stellar X-ray sources significantly (Hünsch et al. 1999), allowing more detailed population studies. Observations of complete samples of cool, main-sequence stars with ROSAT have shown the formation of X-ray emitting coronae around stars with outer convection zones to be universal (Schmitt et al. 1995, 1997).

The ubiquitous occurrence of coronae in stars with spectral types F–M as shown in Fig.1.9 was one of the mayor discoveries in stellar X-ray astronomy. X-ray surface fluxes F_X span a broad range over three to four orders of magnitude and the Sun was found to be a rather inactive star at the lower end of the distribution of stellar surface fluxes. The lower boundary of observed X-ray surface fluxes is roughly set by the flux from solar coronal holes, i.e. when only open magnetic field topology is present. Observed activity levels of cool stars, as measured by the ratio of X-ray to bolometric luminosity (L_X/L_{bol}), span an even broader range of values from $\sim 10^{-8}$ to $\sim 10^{-3}$ and L_X correlates tightly with rotation or more precisely dynamo efficiency.

The efficiency of a solar-like dynamo is characterised by the inverse of the so-called 'Rossby-Number' (Ro), defined as the ratio between rotational period and convective turnover time. The activity-rotation relation $L_X/L_{bol} \sim Ro^{-2}$ saturates at $L_X/L_{bol} \sim 10^{-3}$ for all cool stars, a level > 1000

times higher than that of the Sun. At a certain Rossby number, whose value depends on stellar type, very fast rotating stars enter the supersaturation regime and L_X/L_{bol} decreases again for faster rotating stars.

The ROSAT observations also confirmed that X-ray brighter stars tend to exhibit harder spectra, consequently they must have higher average plasma temperatures, but a larger scatter is present in this correlation. Since the observed activity levels depend on rotation and stars slow down during their lifetime, it is not surprising that young stars were found to be much more active than older, more slowly rotating stars. This finding suggests, that also the young Sun was much more active than it is at present times. A study of the 'Sun in Time', i.e. of solar analogs at different age (70 Myr – 8 Gyr) was performed and their X-ray properties determined (Güdel et al. 1997). It was found that activity again spans an enormous range. X-ray luminosity, temperature and emission measure of the hot plasma component strongly decreases with age, especially during the first 500 Myr, an evolution that has important consequences on the development of young planets in the solar system.

1.3.2 Properties of coronal plasma

Since stellar coronal structures are not spatially resolved, one has to disentangle the time- and disk-averaged measurements. Time-averaging may at least partly be compensated by sensitivity, and e.g. in the cases of stronger flares the spectral evolution of dominant plasma components can be investigated for short time periods, but disk-averaging is always present. Only in particular cases eclipse mapping of binaries give some hints on the surface distribution of the coronal structures.

However, stellar coronae can be described by appropriate parameters. The emitting volume ($V = 4\pi R^2 l f$) of a stellar corona is given by the available volume and its filling factor. The available volume is the geometrical extend of the corona and depends on the stellar radius (R) and the height of the coronal structures (l), the so-called semi-loop length, while the filling factor (f) describes the amount of the available volumed actually filled with coronal plasma. The plasma itself is described by the emission measure ($EM = \int n_e n_H dV$), that denotes the amount of plasma emissivity that is present, usually at a certain temperature EM(T). The emission

measure distribution (EMD) describes the emissivity and temperatures of the coronal plasma, whereas the underlying temperature-structures is approximated by multi-temperature models, temperature grids or functions. The EMD is of course also a function of time. Different or variable X-ray brightness can thus be produced in various ways; the emitting volume and respectively the filling factor or the height of the corona can differ, likewise the coronal plasma can be at higher densities. These interdependences are hard to disentangle and several effects, i.e. more numerous, larger or X-ray brighter coronal structures, are thought to contribute to the large X-ray luminosities in very active stars.

Another property of the coronal plasma that has to be addressed and which also affects the observed, line-dominated spectra of stars are the coronal elemental abundances. Unfortunately the earlier X-ray missions suffered from possessing only moderate spectral resolution or low sensitivity. Although *Einstein* already provided some higher resolution spectra of brighter stars, necessary for the identification of the stronger emission lines, only with *Chandra* and XMM-Newton high resolution spectra with sufficient signal became available for a larger sample of stars, allowing the determination of coronal abundance pattern and densities. The Sun exhibit a coronal abundance pattern named the FIP (First Ionization Potential) effect, i.e. an enhancement of low-FIP elements, see e.g. Laming et al. (1995). Contrary, the inverse FIP effect was discovered in active stars (Brinkman et al. 2001) and a systematic trend appears to be present, with low-activity stars showing a FIP-like pattern, while moderate active stars show no clear trend and very active stars exhibit the inverse FIP-effect (Güdel et al. 2002; Audard et al. 2003).

Density analysis became likewise possible with high resolution spectra. It exploits density sensitive lines or line ratios, e.g. in He-like triplets. A comprehensive study with He-like triplets of several elements indicated coronal densities for active stars about an order of magnitude higher than in the Sun, while densities of inactive stars are comparable to solar values (Ness et al. 2002). A combination of coronal densities and EMD can be used to derive information on the dimensions of the coronal structure. X-ray sizes of stellar coronae derived from solar scaling laws lead to filling factors of about 0.1 of the re-

spective available volume (Ness et al. 2004).

Combined these findings indicate that inactive stars are dominated by cool, low density plasma that covers only small parts of the stellar surface. On the other hand active stars also possess cool coronal structures which are at higher densities and might cover a quite large fraction of the surface, but they additionally exhibit hotter coronal structures which are probably either located in high density, compact structures or more extended ones, but with moderate density. The hot plasma is reminiscent of solar flare plasma, but found even in quiescence, indicating different coronal structures to be permanently present on the same star. In general stellar coronal structures appear to resemble solar ones, but size and location of magnetic structures as well as temperatures, densities and chemical composition of the plasma strongly depend on the levels of activity that are present on the individual stars.

1.3.3 Active M dwarfs

This section deals with the coronal activity at the end of the main sequence, i.e. in the domain of M dwarfs. Active M dwarfs are known for their high activity levels and can help to test underlying physics and theories of coronal activity and its driving mechanisms.

M dwarfs, also named red dwarfs, are the coolest of the cool stars with surface temperatures around $2500 - 3500$ K. Their masses range from about $0.5\,\mathrm{M}_\odot$ to the sub-stellar boundary at $0.08\,\mathrm{M}_\odot$ and they dominate the number density of stars in the Galaxy. Active M dwarfs show the chromospheric H_α-line in emission, the H_α-line is accessible at optical wavelengths and used as a tracer for activity. This fact is sometimes denoted in the spectral classification by an appendix, i.e. they are called Me stars. Of course, as activity decreases slowly with age, also inactive M dwarfs exist in the old disk and halo population (Giampapa & Liebert 1986).

Active M dwarfs are particularly strong coronal X-ray sources and generally tend to be more active than solar-like stars since they have larger spin-down times. They are well studied with all major X-ray missions and exhibit a high $L_\mathrm{X}/L_\mathrm{bol}$ ratio often at the saturation limit of 10^{-3}. Moreover, during strong flares in the $L_\mathrm{X}/L_\mathrm{bol}$-ratio in active M dwarfs approaches unity. Frequent and strong flaring is

observed regularly and typically show high coronal temperatures even outside large flaring events. Due to their frequent flaring, that was first discovered in the optical regime, later in EUV and X-ray, these stars are also classified as flare-stars. In X-rays flaring M dwarfs were already detected with missions like HEAO-1 (Kahn et al. 1979). Extreme flares with increases in X-ray brightness by factors of up to hundreds are observed for example on the M dwarfs EV Lac (Favata et al. 2000) and, accompanied by a density increase, on Proxima Centauri (Güdel et al. 2004). Beside the stronger flares additional persistent X-ray variability is observed. A large number of power-law distributed flares with different energy output have been proposed as a possible major coronal heating mechanism analogue to the above mentioned nano-flares on the Sun also for other cool stars including M dwarfs, see Kashyap et al. (2002) or Güdel et al. (2003). Active M dwarfs are not only known to be X-ray bright they also possess strong magnetic fields. Photospheric magnetic field strength of the active M dwarfs AD Leo and EV Lac were determined to $3-4\,$kG (Saar & Linsky 1985; Johns-Krull & Valenti 1996) with surface filling factors of about $50-70\%$; both stars are also investigated in this work.

M dwarfs of spectral types later than approximately $M3-M5$ are expected to be fully convective and therefore lack an interface between radiative and convective zones. The observed high levels of activity then require the onset of alternative dynamo mechanisms different to that of the Sun. However, no transition in the activity around this spectral type has ever been noticed, at least up to M8 concerning quiescent emission (Fleming et al. 1993). Two possible explanations are invoked. Either the $\alpha\Omega$-dynamo is smoothly replaced by another dynamo mechanism with the magnetic field stored and strengthened in deep layers of the convection zone or a strong magnetic field blocks convection and consequently stars down to $0.1\,M_\odot$ may possess a radiative core, consequently the transition to fully convective stars would occur at much later spectral type. This could explain the finding by Mohanty & Basri (2003), who discovered a drop in activity around spectral class M9 despite the high observed rotational velocities in these objects, but change of resistivity or or dust formation in its atmospheres are also possible explanations.

1.3.4   Classical T Tauri stars

The mechanisms of X-ray generation in classical T Tauri stars, i.e accreting pre-main sequence stars are a debated topic of actual research. Young late-type stars are strong X-ray sources and their high energy emission influences stellar environments and planetary formation in its very early phases.

T Tauri stars are young, low-mass pre-main sequence stars and copiously found in or near star forming regions. Two subgroups are distinguished according to the strength of the Hα line, the classical T Tauri stars (CTTS) and the weak line T Tauri stars (WTTS). The principal physical differences that distinguish these two classes are that CTTS are thought to be in an earlier evolutionary stage, still possess a disk containing dust and gas and are accreting significant amounts of matter, see Fig. 1.10 for a basic sketch of a CTTS. WTTS are thought to be more evolved and they have mainly lost their disks (or at least are no longer accreting matter). CTTS are generally younger with ages of a few up to $\sim 10\,$Myr and the overall fraction of CTTS in a given star-forming region decreases with age, but both types of T Tauri stars are commonly found in the same star-forming regions, indicating the presence of individual evolutionary time scales. The existence of a disk containing significant amounts of matter and the ongoing accretion onto the host star leads to different spectral properties of CTTS and WTTS. The historical classification is based on the Hα equivalent width, with the dividing border at 10 Å, but since the Hα-line is often time-variable a classification solely based on its strength is sometimes misleading. A suitable energy band where the emission from warm, circumstellar dust is visible, is the infrared and the different infrared designations of CTTS (Class II) and WTTS (Class III) due to the additional near-infrared emission in CTTS makes up an important indicator for its classification. The different criteria used for the identification of CTTS also introduces selection effects in the respective samples. In the domain of X-rays, the disk and other circumstellar material is noticeable by its absorption effect, predominantly of soft photons.

Strong and variable X-ray emission is observed for both type of T Tauri stars and large numbers of these objects were detected in various star forming regions observed with *Einstein* (Feigelson & De-
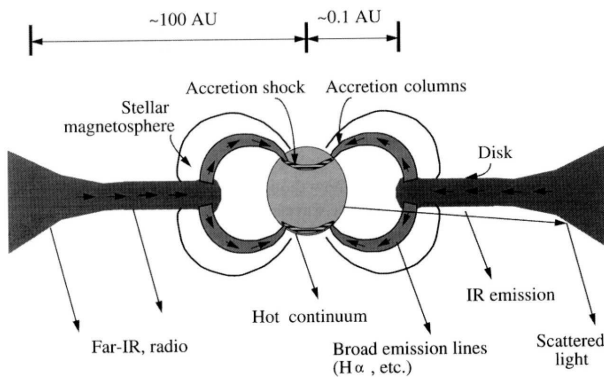
Figure 1.10: A cartoon of a CTTS, indicating the regions where emission at different wavelength originates. X-rays are thought to be generated by magnetic activity, i.e. coronal activity and/or star-disk interaction or in an accretion spot via magnetically funneled accretion. Original from Hartmann (1998).

Campli 1981; Feigelson & Kriss 1989) and ROSAT (Feigelson et al. 1993; Neuhäuser et al. 1995). Their X-ray emission was usually interpreted as an scaled-up version of magnetic activity in analogy to cool main sequence stars and the X-ray emission from WTTS is still thought to originate exclusively from coronal activity. Likewise other spectral properties of WTTS are comparable to active main sequence stars, see e.g Walter et al. (1988) who named theses stars consequently Naked T Tauri stars. On the other hand, T Tauri stars are thought to be at least in their early stages fully convective, therefore the question arises if the analogy with main sequence stars holds and what are the underlying processes for the generation of the magnetic field. A comprehensive review of high energy processes and underlying physics in young stellar objects that summarises the results of the era prior to *Chandra* and XMM-Newton is presented by Feigelson & Montmerle (1999).

Using observations of the Orion Nebula Cloud performed with *Chandra*, Feigelson et al. (2003) analysed a sample of 500 PMS stars with known basic properties. Their X-ray luminosity was found to be correlated with bolometric luminosity, but its values are significantly below the saturation value for main sequence stars. Further on, no strong correlation is found between L_X and rotation as it is observed for main sequence stars, indicating either the presence of a different, e.g. turbulent, dynamo or of

supersaturation effects in solar-type dynamos. The deep COUP (*Chandra* Orion Ultradeep Project) exposure of $\sim$ 10 days showed that in CTTS accretion suppresses activity on average and also introduces a large scatter in the correlation between X-ray activity and stellar parameters like mass or L_{bol} (Preibisch et al. 2005). In CTTS magnetic activity phenomena may involve the circumstellar material, e.g. via star-disk interaction, but the topology of their magnetic fields is virtually unknown. The bulk of X-ray emission seen in the COUP sources is of coronal origin, but Favata et al. (2005) found evidence that magnetic star-disk interaction may be involved in the origin of bright X-ray flares.

High-resolution spectroscopy of CTTS performed with *Chandra* and XMM-Newton indicated accretion shocks as an additional mechanism for the generation of X-rays in CTTS. In this scenario the X-ray emission is produced by a magnetically funneled accretion stream falling onto small areas of the stellar surface producing shocked high density plasma (Shu et al. 1994; Calvet & Gullbring 1998). In magnetospheric accretion matter falls from several stellar radii at nearly free-fall velocity, leading to strong shocks that form sufficiently hot plasma to emit in the X-ray regime. TW Hya was the first example of a CTTS, where observational evidence for accretion was found in X-ray data (Kastner et al. 2002; Stelzer & Schmitt 2004). The analysis of density sensitive line-ratios in He-like triplets indicated very high densities for the X-ray emitting plasma of TW Hya, exceeding by far the densities previously found in coronal plasma from any other star. The investigation of further accreting young stars and their X-ray properties, combining high resolution spectroscopy and very sensitive observations for a sample of CTTS, is presented in this work.

1.3.5 Coronal activity cycles

Stars as old as the Sun are only moderately active, but as chromospheric measurements showed they often exhibit cyclic activity behaviour. The here studied stars are solar-like in the sense that they have moderate to low activity levels, approximately the same spectral type and age as the Sun. Beside its strong astrophysical interest, solar activity is due to its influence on the terrestrial climate also important for evolution of life and therefore our own future.

The physics of activity cycles may hold a key to understanding the future evolution of life conditions on Earth.

The best known example of cyclic activity is of course the already mentioned solar-cycle. On the Sun many activity-related phenomena, such as sunspot number, extend of the corona, EUV and X-ray coronal emission are strongly modulated throughout the 11-year solar cycle (the magnetic reversal is disregarded) and the cyclic behavior is one of the most characteristic feature of the magnetic activity of the Sun. The degree of modulation in the energetic radiation during the cycle is very large, between solar minimum and maximum the X-ray flux varies by a factor of $\simeq$ 10 to 100, depending on the considered energy band. The huge variations in X-ray flux which occur within the solar cycle have been already observed with missions like Yohkoh (Acton 1996) and GOES. A sequence of Yohkoh X-ray images taken over half a solar cycle is shown in Fig. 1.11. The Yohkoh data shows that the variability of the solar X-ray luminosity is mainly caused by a strong decrease of the emission measure, whereas the average coronal temperature decreases from $\sim 3\,\mathrm{MK}$ to $\sim 2\,\mathrm{MK}$.

Understanding cyclic activity profoundly can only be obtained by expanding the investigation to studies beyond those of the Sun alone and to check if other stars exhibit cyclic behaviour and with what properties, i.e. cycle amplitude, period, spectral variations, etc.. The question, if the Sun's cyclic behaviour is rather typical or anomalous, can be addressed by observing parameters that change in the course of an activity cycle in a variety of stars with different characteristics that allow to determine the relationship between cycle behaviour and other relevant physical parameters.

Our knowledge of activity cycles in other stars is largely based on the Mt. Wilson program of optical monitoring the Ca II H+K chromospheric flux (S-index) in a large sample of cool stars. Ongoing since the 1960s for roughly 100 stars the Ca II emission has been monitored over decades and the program has already shed light on important characteristics of the chromospheric cyclic behaviour (Baliunas et al. 1995). The chromospheric variations of cool stars can be interpreted as an evolutionary sequence. Young, fast rotating active stars show large variations
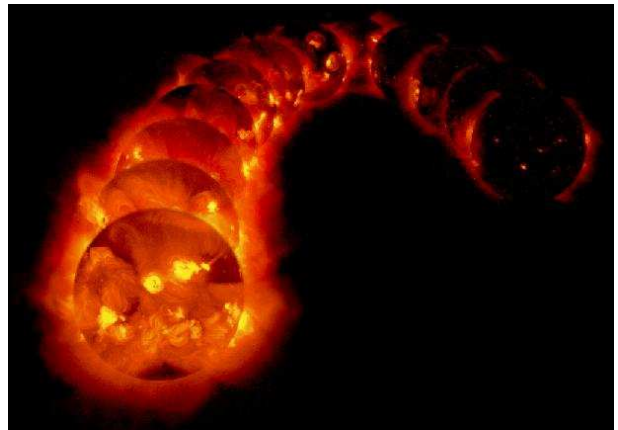
Figure 1.11: The Sun in X-rays observed over half a solar cycle 1991-1995 (Yohkoh SXT, $0.25 - 4\,\mathrm{keV}$). Active regions are numerous during solar maximum and nearly absent during minimum.

in their Ca II flux, but no evidence of cycles. With stars of intermediate age exhibiting more moderate activity and occasionally cyclic behaviour, the lowest active stars show even smaller variations, but often a smooth cyclic behavior with periods ranging from ~ 3 to ~ 20 yr. Some stars, mostly with the lowest activity levels, show very little if any variability with no cyclic behaviour and could be in long-term activity minimum, comparable to the Maunder-like state on the Sun. While the Ca II flux is a convenient proxy of the activity level for solar-type stars, the modulation by only $\simeq 20\%$ is much weaker than in X-rays.

Contrary, clear indications for coronal activity cycles on other stars than the Sun were only recently found on a few objects. The absence of frequent long-term observations of individual stars in X-rays prevented a study of coronal activity cycles so far. Repetitive X-ray observations, usually of more active stars, showed no evidence for strong coronal cyclic variations. As with chromospheric activity, the search for X-ray activity cycles is most promising in moderate and low activity stars, which are consequently not very X-ray bright and therefore nearby objects are favourable. The analysis of ROSAT HRI observations of the binary 61 Cyg already showed some evidence of X-ray cyclic behaviour correlated with chromospheric activity (Hempelmann et al. 2003), but its amplitude of a factor $2 - 3$ is rather small compared to the Sun.

To shed some sight on the topic of coronal activity cycles of solar-like stars, a long-term monitoring program with XMM-Newton was initiated. A breakthrough has come from the analysis of the first three years of XMM-Newton data of HD 81809 published by Favata et al. (2004). While its strong long-term order of magnitude modulation is analog to the solar case, HD 81809 differs in other aspects. A lag appears be present between the chromospheric and the coronal maximum and the X-ray spectral variations are not as strong as observed for the Sun over the solar cycle. The stars α Cen A/B and 61 Cyg A/B are part of this observation program and possible coronal activity cycles are investigated in this work.

1.4 The XMM-Newton satellite

1.4.1 Mission overview

XMM-Newton was launched in December 1999 and is named after its design of X-ray Multiple Mirrors and to honour Isaac Newton for inventing spectroscopy and his association with the theory of gravity. See Fig. 1.12 for a view of the satellite. Its highly eccentric orbit allows to observe targets continuously up to about 40 hours. XMM-Newton is equipped with three co-aligned X-ray telescopes with a focal length of 7.5 m accompanied by an optical 30 cm telescope. The X-ray telescopes are Wolter type-1 telescopes to focus the incoming X-rays via two grazing-incidence reflections on a parabolic and a hyperbolic surface. Each X-ray mirror module consists of 58 gold-coated, nested mirrors providing an effective area of 1550 cm^2, making it the most sensitive X-ray telescope so far. XMM-Newton has three types of instruments to collect scientific data, the EPIC (European Photon Imaging Camera) and RGS (Reflection Grating Spectrometer) are X-ray detectors while the OM (Optical Monitor) measures optical/UV radiation. The EPIC consists of three CCD cameras, namely two MOS and one PN detector. Both types provide imaging with intrinsic medium spectral resolution, but they differ in its technical specifications like CCD layout, pixel size etc. To provide high spectral resolution two RGS detectors are onboard of XMM-Newton. Thus five simultaneously operated X-ray instruments are in use. Two X-ray telescopes are equipped with a MOS and a

Figure 1.12: An artistic view of XMM-Newton. The satellite has a length of 10 m, a span of 18 m, a weight of 18 t and an orbiting time of two days.

RGS detector and one X-ray telescope is equipped with the PN detector. Three different optical blocking filters as well as several read-out modes allow to adapt the instruments to the particular observation. Each detector operates in the photon counting mode, providing its individual event list which contains attributes of the events like position, arrival time and energy.

Altogether the main characteristics featuring XMM-Newton are the possibility of simultaneous observations of X-ray sources with high and medium spectral resolution additionally providing high sensitivity and good angular resolution. These features make XMM-Newton an unique instrument for the exploration of the X-ray sky. In the context of this work primarily data taken with X-ray detectors onboard XMM-Newton are used.

1.4.2 Scientific X-ray instruments

The EPIC instruments provide imaging with a field of view of 30 $'$ and allow medium resolution spectroscopy with $\Delta E/E \sim 20 - 50$. The PN operates in the energy range of $0.2 - 15.0$ keV and is by far the most sensitive instrument, mainly because it gets the full light of an X-ray telescope. Moreover, its outstanding quantum efficiency allows to effectively detect photons with higher energies. It is ideal to investigate everything that is otherwise limited by its photon statistic, i.e. faint sources and short exposures, time variability in different energy bands or photons
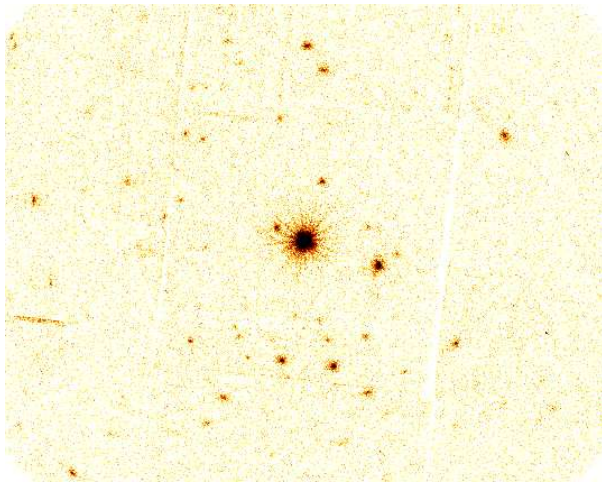
Figure 1.13: The Aurigae star forming region with SU Aur in the center of the image taken with MOS1.

with higher energies. It provides a spectral resolution of 80 eV (at 1.0 keV energy) and an angular resolution of 6″ FWHM, PSF (Point Spread Function), the corresponding pixel size is $\sim 4″$. The MOS detectors operate in the energy range of 0.2–12.0 keV. While the sensitivity of the MOS detectors is lower compared to PN, each MOS gets roughly 45% of the light of an X-ray telescope, its angular (5″ FWHM, PSF) and spectral resolution (70 eV at 1 keV) are slightly better. Further on its corresponding pixel size of 1″ is much smaller and images are fully sampled. It is therefore ideal for imaging, resolution of close binaries and analysis of moderate resolution spectra if the targets are sufficiently bright. XMM-Newtons large field of view also allows the observation of extended or multiple targets, see Fig. 1.13.

The second X-ray instrument is the RGS, which provides high resolution spectroscopy. For the two RGS detectors the X-rays are refracted by grating plates and detected by a strip of CCDs which are of the same type as used in the MOS detector, whereas the intrinsic energy resolution of the CCDs allows to distinguish the spectral orders. The energy range of 0.35–2.5 keV (5–35 Å) covered by the RGS contains a large number of emission lines, the spectral resolution is 0.04 Å (3.2 eV) at 1.0 keV in first order. With an $\Delta\lambda/\lambda$ of several hundreds depending on the wavelength of interest, most of the stronger emission lines are resolved. It is essential for density analysis and ideal to investigate the physical conditions and

the composition of the X-ray emitting plasma at low to medium energies. A detailed description of the instruments onboard XMM-Newton can be found in Ehle et al. (2005).

1.4.3 Data and Analysis

The specific methods used in data analysis are described in the respective chapters and only a brief overview is given here to indicate the methods that are used throughout this work.

The simultaneous observation of the targets with several complementary detectors permits the choice to use either the multiple data-sets separately for scientific tasks or to combine the data. Each detector is used in this work mainly for individual analysis tasks, utilising its own special features. Combined data is usually used only from the same type of instrument, i.e. both RGS or MOS, to account for calibration uncertainties and to cross-check the results. See also Chapter 2 for a comparison of the instruments and further discussion. When detector gaps are present, when the signal to noise is low or the spectral range has to be extended, also a combined analysis is performed or results from one instrument, e.g. in spectral analysis elemental abundances determined with the RGS, can be used as input for further modelling.

Event selection is usually the first step after processing the raw data. To select good events, i.e. the desired X-ray photons, various steps are applied for filtering the data. A description of the SAS (Science Analysis System), the standard software used for extracting data products like images, light curves and spectra from XMM-Newton data as well as an explanation of the standard selection criteria used for filtering the data is given in Loiseau et al. (2004). Since the X-ray data are stored in event lists, this further allows the selection of individual X-ray photons according to the scientific purpose based on the properties of individual events. For example, the background can be suppressed effectively by selecting events in spatial regions and energy intervals, which is for example utilized in the work on Beta Pic for source detection (Chapter 6). Time-resolved spectroscopy and light curves, which are essential for analysis of transient events like flares, utilize the event lists scheme, see e.g. the works on M dwarfs (Chapter 2) or on CTTS (Chapter 5) . The knowledge

of the instrumental PSF (Point Spread Function) can be used to determine the brightness of the individual components in close binary systems, utilized in the PSF fitting algorithm developed during the course of this work. It allows to disentangle overlapping PSFs by fitting two instrumental PSFs to the event distribution in the sky plane, a method applied in the work on EQ Peg (Chapter 3) and Alpha Centauri (Chapter 7) to accurately determine the X-ray brightness of the components. For spectral analysis the XSPEC software (Arnaud 1996) is used and multi-temperature spectral models are applied to the data. Such models assume the emission spectrum of a collisionally-ionized diffuse optically-thin gas as calculated with the APEC code, see e.g. Smith et al. (2001). Plasma densities are investigated with density sensitive line ratios in He-like triplets (e.g. O VII, Ne IX), the theory and applications of He-like triplets are described e.g. in Porquet et al. (2001). The strength of individual emission lines used in this analysis was determined with the CORA program (Ness & Wichmann 2002).

1.5   Outline

My thesis deals with the X-ray emission of cool stars as observed with XMM-Newton. It is a cumulative work on several subtopics of the field, but all analysis are related to stellar activity and the studied stars have in common the presence of activity phenomena involving magnetic fields. However, levels of activity, the mechanisms for X-ray generation in the individual targets as well as stellar properties like age or mass often differ quite strongly. Therefore I introduce the following grouping of the work according to physical topics instead of following a chronological order.

Chapter 2 deals with the coronal activity of active M dwarfs. The analysed M dwarfs, namely the single stars AD Leo and EV Lac as well as the binaries AT Mic and EQ Peg, are strong X-ray emitters in the solar vicinity, ensuring high data quality in all instruments. It is a comparative work of their X-ray properties as a class, here dealing with four M dwarfs of spectral type M 3.5 − M 4.5, i.e. the region where stars are thought to become fully convective. In Chapter 3 an initial work on the spatially resolved X-ray emission of the M dwarf binary system EQ Peg is presented.

Chapter 4 and 5 deal with the X-ray generating mechanisms in late-type, pre-main sequence stars which still accrete matter, so called classical T Tauri stars. This includes Chapter 4, which discusses mainly RGS data of the target BP Tau and implications derived from the simultaneous UV observation as well as Chapter 5 that presents a study of X-ray properties of classical T Tauri stars as a class, covering the sources BP Tau, CR Cha, SU Aur and TW Hya. Chapter 6 is also devoted to a young star surrounded by a disk. It reports the detection of weak X-ray emission from the young A5V star Beta Pictoris. The mechanism of the X-ray generation is unclear, accretion or the presence of a cool corona as possible explanations are discussed therein. The sections on BP Tau and Beta Pic are collaborations with me as the second author. My contribution to these paper is mainly the analysis of the X-ray data and corresponding tables, figures and the accompanying writing; in Chapter 4 mostly in Sect. 2.2 and in Chapter 6 mostly in Sect. 2 and especially the source detection with the MOS detector (Sect. 2.2 and Table 2).

The subject of Chapter 7 and 8 is the study of coronal activity cycles of rather inactive late-type stars, analoguesly to the one observed for the Sun. In the context of this work the binary systems Alpha Centauri A/B, consisting of a G2V and a K1V star, is investigated in Chapter 7 and indications for activity cycles are presented. Chapter 8 reports preliminary results of the 61 Cyg A/B (K5V and K7V) observations and includes a recent observation from the ongoing campaign on Alpha Centauri.

Finally, a summary can be found in Chapter 9 as well as an outlook to future work.

Bibliography

Acton, L.W. 1996, ASP Conf. Series, 109, 45

Arnaud, K.A. 1996, ASP Conf. Series, 101, 17

Audard, M., Güdel, M., Sres, A., et al. 2003, A&A, 398, 1137

Babcock, H.W. 1961, ApJ, 133, 572

Baliunas, S.L., Donahue, R.A., Soon, W.H., et al. 1995, ApJ, 438, 269

Brinkman, A.C., Behar, E., Güedel, M., et al. 2001, A&A, 365, L324

Calvet, N., Gullbring, E. 1998, ApJ, 509,802

Catura, R.C., Acton, L.W., Johnson, H.M. 1975, ApJ, 196, L47

Ehle, M., Breitfellner, M., Gonzales Riestra, R., et al. 2005, XMM-Newton User's Handbook Issue 2.3

Favata, F., Reale, F., Micela, et al. 2000, A&A, 353, 987

Favata, F., Micela, G. 2003, SSR, 108, 577

Favata, F., Micela, G., Baliunas, S.L. et al. 2004, A&A, 418, L13

Favata, F., Flaccomio, E., Reale, F., et al. 2005, ApJS, 160, 469

Feigelson, E.D., DeCampli, W.M. 1981, ApJ, 243, L89

Feigelson, E.D., Kriss, G.A. 1989, ApJ, 338, 262

Feigelson, E.D., Casanova, S., Montmerle, T., Guibert, J. 1993, ApJ, 416, 623

Feigelson, E.D., Montmerle, T. 1999, Ann. Rev. A&A, 37, 363

Feigelson, E.D., Gaffney, J.A., Garmire, G. et al. 2003, ApJ, 584, 911

Fleming, T.A., Giampapa, M.S., Schmitt, J.H.M.M., et al. 1993, ApJ, 410, 387

Giampapa, M.S., Liebert, J. 1986, ApJ, 305, 784

Golub, L., Pasachoff, J.M. 1997, The Solar Corona, Ca.Ü.P.

Güdel, M., Guinan, E.F.,, Skinner, S.L. 1997, ApJ, 483, 947

Güdel, M., Audard, M., Sres, A., et al. 2002, ASPC, 277, 497

Güdel, M., Audard, M., Kashyap, V.L., et al. 2003, ApJ, 582, 423

Güdel, M. 2004, A&ARv, 12, 71

Güdel, M., Audard, M., Reale, F. et al. 2004, A&A, 416, 713

Hartmann, L. 1998, Accretion Processes in Star Formation 1998, Ca. U. P.

Hempelmann, A., Schmitt, J.H.M.M., Baliunas, S.L., Donahue, R.A., A&A, 406, L39

Hoyt and Schatten 1997, The Role of the Sun in Climate Change, Ox. U. P.

Hünsch, M., Schmitt, J.H.M.M., Sterzik, M.F., et al. 1999, A&A Sup. Ser., 135, 319

Johns-Krull, C.M. and Valenti, J.A., ApJ, 459, L95

Kahn, S.M., Linsky, J.L., Mason, K.O., et al. 1979, ApJ, 234, L111

Kashyap, V.L., Drake, J.J., Güdel, M., Audard, M. 2002, ApJ, 580, 1118

Kastner, J.H., Huenemoerder, D.P., Schulz, N.S., et al. 2002, ApJ, 567, 434

Laming, J.M., Drake, J.J., Widing, K.G. 1995, ApJ, 443, 416

Loiseau, N. (edt.), Ehle, M., Pollock, A.M.T., et al. 2004, User's Guide to XMM-Newton Science Analysis System Issue 3.1

Martens, P.C.H., Kuin, N.P.M. 1989, SoPh, 122, 263

Mohanty, S., Basri, G. 2003, ApJ, 583, 451

Ness, J.-U., Wichmann, R. 2002, AN, 323, 129

Ness, J.-U., Schmitt, J.H.M.M., Burwitz, V., et al. 2002, A&A, 394, 911

Ness, J.-U., Güdel, M., Schmitt, J.H.M.M., et al. 2004, A&A, 427, 667

Neuhäuser, R., Sterzik, M.F., Schmitt, J.H.M.M. et al. 1995, A&A, 297, 391

Pallavicini, R., Serio, S., Vaiana, G.S. 1977, ApJ, 216, 108

Pallavicini, R., Golub, L., Rosner, R. et al. 1981, ApJ, 248, 279

Parker, E.N. 1955, ApJ, 122, 293

Parker, E.N. 1979, Cosmical Magnetic Fields, Ox. U. P.

Parker, E.N. 1988, ApJ, 330, 474

Porquet, D., Mewe, R., Dubau, J., et al. 2001, A&A, 376, 1113

Preibisch, T., Kim, Y.-C., Favata, F., et al. 2005, ApJS, 160, 401

Rosner, R., Tucker, W.H., Vaiana, G.S. 1978, ApJ, 220, 643

Saar, S.H., Linsky, J.L. 1985, ApJ, 299, L47

Schmitt, J.H.M.M., Golub, L., Harnden, F.R., et al. 1985, ApJ, 290, 307

Schmitt, J.H.M.M., Collura, A., Sciortino, S., et al. 1990, ApJ, 365, 704

Schmitt, J.H.M.M., Fleming, T.A., & Giampapa, M.S. 1995, ApJ, 450, 392

Schmitt, J.H.M.M. 1997, A&A, 318, 215

Schrijver, J.C., Zwaan, C. 2000, Solar and Stellar Magnetic Activity, Cam. U. P.

Serio, S., Peres, G., Vaiana, G.S., et al. 1981, ApJ, 243, 288

Shu, F.H., Najita, J., Ostriker, E., et al. 1994, ApJ, 429, 781

Smith, R.K., Brickhouse, N.S., Liedahl, D.A., Raymond, J.C. 2001, ASP Conf. Series, 247, 161

Stelzer, B., Schmitt, J.H.M.M. 2004, A&A, 418, 687

Usoskin, I.G., Mursula, K., Solanski, S., et al. 2004, A&A, 413, 745

Vaiana, G.S., Cassinelli, J.P., Fabbiano, R., et al. 1981, ApJ, 244, 163

Vesecky, J.F., Antiochos, S.K. and Underwood, J.H. 1979, ApJ, 233, 987

Walter, F.M., Brown, A., Mathieu, R.D., et al. 1988, AJ, 96, 297

Chapter 2

X-ray properties of active M dwarfs as observed by XMM-Newton

J. Robrade and J. H. H. M. Schmitt

**Astronomy
&
Astrophysics**

X-ray properties of active M dwarfs as observed by XMM-Newton

J. Robrade and J. H. M. M. Schmitt

Hamburger Sternwarte, Universität Hamburg, Gojenbergsweg 112, 21029 Hamburg, Germany
e-mail: jrobrade@hs.uni-hamburg.de

Abstract. We present a comparative study of X-ray emission from a sample of active M dwarfs with spectral types M3.5–M4.5 using XMM-Newton observations of two single stars, AD Leonis and EV Lacertae, and two unresolved binary systems, AT Microscopii and EQ Pegasi. The light curves reveal frequent flaring during all four observations. We perform a uniform spectral analysis and determine plasma temperatures, abundances and emission measures in different states of activity. Applying multi-temperature models with variable abundances separately to data obtained with the EPIC and RGS detectors we are able to investigate the consistency of the results obtained by the different instruments onboard XMM-Newton. We find that the X-ray properties of the sample M dwarfs are very similar, with the coronal abundances of all sample stars following a trend of increasing abundance with increasing first ionization potential, the inverse FIP effect. The overall metallicities are below solar photospheric ones but appear consistent with the measured photospheric abundances of M dwarfs like these. A significant increase in the prominence of the hotter plasma components is observed during flares while the cool plasma component is only marginally affected by flaring, pointing to different coronal structures. AT Mic, probably a young pre-main-sequence system, has the highest X-ray luminosity and exhibits also the hottest corona. While results of EQ Peg and EV Lac are presented here for the first time, AT Mic and AD Leo have been investigated before with different analysis approaches, allowing a comparison of the results.

Key words. stars: activity – stars: coronae – stars: flare – stars: late-type – X-rays: stars

1. Introduction

Observations with ROSAT have shown the formation of X-ray emitting coronae around late-type cool dwarf stars with outer convection zones to be universal (Schmitt et al. 1995; Schmitt & Liefke 2004). Coronal structures on the Sun are dominated by their magnetic properties with closed structures, the coronal loops or loop arcades, containing predominantly the X-ray emitting, confined hot high-density plasma and being the location of flare events. In the Sun the interaction between the radiative and the outer convective zones powers a dynamo, leading to coronal activity. The ubiquitous occurrence of X-ray emission among cool stars and their dependence on rotation strongly suggests also a magnetic character of their activity. Observed activity levels of cool stars, as measured by the ratio of bolometric and X-ray luminosities, span a range of values from $\sim 10^{-8}$ to $\sim 10^{-3}$ that are correlated with dynamo efficiency. The efficiency of a solar-like magnetic dynamo is characterised by the inverse of the so-called "Rossby-Number", defined as the ratio between rotational period and convective turnover time. This activity-rotation relation saturates at $L_X/L_{bol} \sim 10^{-3}$, a level >1000 times higher than that of the Sun. The similarity of stellar and solar X-ray emission and flares suggests similar basic physical mechanisms, with more active stars showing more frequent and larger flares. Flaring has been proposed as a possible major coronal heating

mechanism for the Sun via nanoflares (Parker 1988) as well as for other cool stars including M dwarfs. For recent reviews on this topic, see Kashyap et al. (2002) or Güdel et al. (2003).

Active M dwarfs, belonging to the so-called flare stars, turned out to be particularly strong coronal X-ray sources. Frequent flaring on these objects was first discovered in the optical regime, later in EUV and X-rays. These late-type dwarf stars are generally more active than solar-like stars since they have larger spin-down times. They also typically show higher coronal temperatures. M dwarfs of spectral types later than approximately M3–M5 are expected to be fully convective and therefore lack an interface between radiative and convective zones. The observed high levels of activity then require the onset of alternative dynamo mechanisms different to that of the Sun.

The stars chosen here for analysis are known high X-ray emitters with spectral types in the range M3.5–M4.5 and are located in the immediate solar vicinity (distance 5−10 pc). EQ Peg (Gl 896A, Gl 896B) is a visual binary consisting of two M dwarfs of spectral type M3.5 and M4.5, both of which are flare stars, as well as AT Mic (Gl 799A, Gl 799B), an active binary system consisting of a M4.5 and a M4 star. Both binaries are separated by roughly 30 AU, making interaction between the components quite unlikely. On the other hand, AD Leo (Gl 388) is a single M3.5 star similar to EV Lac (Gl 873). Our sample M dwarfs are also all fast rotators

Table 1. Stellar parameters; $v \sin i$ from Delfosse et al. (1998) except AT Mic (Fuhrmeister et al. 2004) and EQ Peg (Stauffer & Hartmann 1986), J from 2MASS point source catalog, L_{bol} calculated from J using values of Kenyon & Hartmann (1995), L_{bol}/L_X with L_X (this work, PN).

Star	d (pc)	$v \sin i$ (km s^{-1})	J (mag)	log L_{bol}	log L_{bol}/L_X
AT Mic A+B	10.2	11.7(A)	5.81	32.46	–3.00
EQ Peg A+B	6.2	12/18(A/B)	5.79	32.04	–3.22
AD Leo	4.7	6.2	5.45	31.94	–3.21
EV Lac	5.0	6.9	6.11	31.73	–2.99

Table 2. Observation log.

Target	Instrument (mode)	Dur. (s)	Obs. time
EQ Peg	MOS (FF, thick F.)	14 600	2000-07-09T11:39–15:43
"	PN (FF, thick F.)	12 410	2000-07-09T12:20–15:47
"	RGS (HER/SES)	15 610	2000-07-09T11:31–15:51
AT Mic	MOS1 (SW, med. F.)	25 400	2000-10-16T00:28–07:32
"	PN (SW, med. F.)	25 100	2000-10-16T00:42–07:40
"	RGS (HER/SES)	28 310	2000-10-16T00:20–08:11
AD Leo	MOS2 (LW, thick F.)	35 800	2001-05-14T20:55–06:52
"	PN (SW, med. F.)	35 000	2001-05-14T21:11–06:54
"	RGS (HER/SES)	36 400	2001-05-14T20:48–06:55
EV Lac	MOS2 (SW, med. F.)	32 260	2001-06-03T07:55–16:53
"	PN (SW, med. F.)	31 470	2001-06-03T08:11–16:55
"	RGS (HER/SES)	32 860	2001-06-03T07:49–16:56

($v \sin i > 5$ km s^{-1}) (Delfosse et al. 1998; Fuhrmeister et al. 2004) in the saturated regime, i.e. $L_X/L_{bol} \sim 10^{-3}$. Stellar parameters important for this work are summarized in Table 1. Note that the spectral classification in the literature is not unique for all M dwarfs in our sample and may differ by one spectral subclass; the values listed here are taken from the SIMBAD database.

While X-ray emission from AD Leo and AT Mic was already detected by HEAO 1 (Kahn et al. 1979) and EQ Peg is contained in the *Einstein* Stellar Survey (Vaiana et al. 1981), EV Lac was first detected by EXOSAT (Schmitt & Rosso 1988). All stars in our sample were also detected in the ROSAT all-sky survey (Hünsch et al. 1999) and were observed by various other X-ray missions. A comparative analysis of X-ray spectra from AD Leo and EV Lac obtained with BeppoSAX and ROSAT PSPC was performed by Sciortino et al. (1999). Favata et al. (2000a) presented a study of an extreme X-ray flare on EV Lac observed with ASCA. Favata et al. (2000b) studied AD Leo data taken by *Einstein*, ROSAT and ASCA and found the coronal structures to be compact and the quiescent coronal luminosity remarkably constant over decades.

Parts of the XMM-Newton data of AT Mic were previously analysed with special focus on elemental abundances and emission measures during flaring and quiescent state (Raassen et al. 2003). While the coronae of low activity stars like the Sun (Laming et al. 1995) show an enhancement of low-FIP elements, the so-called FIP (First Ionization Potential) effect, Raassen et al. (2003) discovered in the corona of the highly active star AT Mic an inverse FIP effect, which appears to flatten during the flare state. A comparative study of flares on AD Leo observed with XMM-Newton and *Chandra* was performed by Besselaar et al. (2003) and again an inverse FIP effect was found. An analysis of spatially resolved X-ray emission of the EQ Peg system was presented by Robrade et al. (2004). A comparative study on coronal density diagnostics with He-like triplets that includes work on our sample stars can be found in Ness et al. (2002) and with special focus on the X-ray sizes of coronae in Ness et al. (2004).

The above listed M dwarfs were observed with XMM-Newton and the goal of this paper is to present a comparative analysis of these X-ray observations and to determine those properties that are typical for active M dwarfs as a class and those attributed to individual objects. In Sect. 2 we describe the observations and the methods used for data

analysis. In Sect. 3 we present the results subdivided into different physical topics which is followed by a summary and our conclusions in Sect. 4.

2. Observation and data analysis

The four targets, AD Leo, AT Mic, EV Lac and EQ Peg, were observed with XMM-Newton using varying detector setups and exposure times in the range of 15–35 ks. No attempts were made to separate the binaries in this work, therefore data from AT Mic and EQ Peg is a superposition of the respective system components. A detailed description of the observations is provided in Table 2. Useful data were collected in all X-ray detectors onboard XMM-Newton, respectively the EPIC (European Photon Imaging Camera) and RGS (Reflection Grating Spectrometer) detectors which are operated simultaneously. The EPIC instrument consists of three CCD cameras with two different CCD designs, two MOS and one PN, providing imaging and spectroscopy in the energy range from 0.15 to 15 keV with good angular and moderate spectral resolution. In this work EPIC data is used only when the detectors observed in the imaging mode and therefore data from both MOS detectors are presented only for EQ Peg. The RGS is a grating spectrometer with high spectral resolution consisting of two identical spectrometers. The RGS operates in the energy range from 0.35 to 2.5 keV (5–35 Å) with a spectral resolution of ~4.0 eV (0.06 Å, *FWHM*) at 1.0 keV in first order. A detailed description of the XMM-Newton instruments is given by Ehle et al. (2003).

The data were reduced with the standard XMM-Newton Science Analysis System (SAS) software, version 5.4.1 with calibration files updated in January 2004. Light curves and spectra were produced with standard SAS tools and standard selection criteria were applied for filtering the data (see Ehle et al. 2004). Spectral analysis was done with XSPEC V11.3 (Arnaud 1996).

Data from the detectors of different type were fitted separately to allow comparison of the results and to check for possible cross-calibration problems. Spectral analysis

of EPIC data is performed in the energy band between $0.2-12.0$ keV. RGS first order spectra in the full energy range, i.e. $0.35-2.5$ keV $(5-35$ Å) are used. Data of the same detector type, e.g. RGS1 and RGS2, and in the EQ Peg case MOS1 and MOS2, were analyzed simultaneously but not co-added. For spectral analysis the data was cleaned of proton flares by removing the affected time periods, and in the EQ Peg case the data was additionally cleaned for pile-up by excluding the inner part of the source emission. The applied selection criteria were adjusted according to observation mode. The background was taken from source-free regions on the detectors.

We apply the same type of spectral model to all data to perform a self-consistent analysis. Therefore we use the global fitting approach, where the whole spectrum is fitted instead of a line-based method which would be applicable only to RGS data. Audard et al. (2004) applied both methods to data of YY Mensae taken by *Chandra* and XMM-Newton and found consistent results. These authors fitted data from RGS and MOS in selected energy ranges simultaneously, similar to our joint fits, which are briefly discussed in Sect. 3.2.2. Larger deviations were found when using data of different detectors, a problem also affecting our analysis. However, Sanz-Forcada et al. (2003) analysed *Chandra* and XMM-Newton data of AB Dor, a highly active near-main-sequence K star, and found the line-based method to be better suited to fit their high resolution spectra, leading to slightly higher abundances and lower emission measures to be present in the derived models compared to the global fitting approach. Güdel et al. (2001) analysed EPIC and RGS spectra from different observations of AB Dor using the global approach and found different absolute abundance values but a pattern (increasing depletion of abundance of low FIP elements up to iron followed by the inverse pattern for elements with higher FIP) overall consistent with the results derived by Sanz-Forcada et al. (2003), demonstrating the robustness of abundance ratios in general.

For the analysis of the X-ray spectra we specifically use multi-temperature models with variable but tied abundances, i.e. the same abundance pattern in all temperature components. Such models assume the emission spectrum of a collisionally-ionized diffuse optically-thin gas as calculated with the APEC code (see Smith et al. 2001). Abundances are calculated relative to solar photospheric values as given by Anders & Grevesse (1989). For iron and oxygen we use the updated values of Grevesse & Sauval (1998). Comparing stellar coronal with solar photospheric abundances is of course crude, but precise photospheric abundances are unknown for the observed targets; a detailed discussion of the abundances is given in Sect. 3.2.3. Due to the proximity of the stars, absorption in the interstellar medium is negligible at the wavelengths of interest and was not applied in our modelling. Our fit procedure is based on χ^2 minimization, therefore spectra are rebinned to satisfy the statistical demand of a minimum value of counts per spectral bin; 25 for data with an average count rate above 5 cts s^{-1} and 15 for data with an average count rate below 5 cts s^{-1} and for all data used in time resolved analysis. Bad channels are always excluded from the fit; these include channels at high energy in the EPIC spectra that contain insufficient source counts (see Fig. 3). The first model uses

three temperature components (3-T model) with free temperatures and emission measures. Models with additional temperature components were checked, but did not improve the fit results significantly. In order to approximate physically more realistic continuous temperature distributions of the plasma, we use a 6-T model on a logarithmic, almost equidistant grid $(0.2, 0.3, 0.6, 1.2, 2.4, 4.8$ keV), which covers roughly the temperature range from 2 to 60 MK and samples those spectral regions where the XMM-Newton detectors are most sensitive.

Consider next the different spectral resolution, $\Delta E/E$, and energy range of the EPIC and RGS instruments. Especially at low energies, $\Delta E/E$ is quite large for the EPIC detectors, while in the RGS most of the strongest emission lines are separated in this energy range, thus permitting a more accurate determination of plasma parameters. Some elements, in particular C and N, show prominent features only in the RGS. Therefore, to fit the EPIC data the abundances of these elements were set to the RGS value in order to avoid unphysical solutions. For elements such as Al, Ca and Ni, whose abundances in the solar photosphere are an order of magnitude lower than that of Fe and which show only very weak features in the X-ray spectrum, we adopted a coronal abundance of 0.4 times the solar photospheric abundance (a typical value for Fe in this sample). The EPIC detectors are able to measure higher energy X-rays, important for a reliable determination of the properties of the hotter plasma components, with the MOS detectors providing a slightly better spectral resolution and the PN detector providing greater sensitivity.

An important feature of the considered spectral models is the interdependency between the emission measure $(EM = \int n_e n_H dV)$ of temperature components on the one hand and elemental abundances with temperature sensitive emission lines in the considered temperature range on the other hand. This is especially true for EPIC data with their moderate spectral resolution. Another general source of uncertainties is the incomplete knowledge of atomic data used to calculate the spectral models, see e.g. Porquet et al. (2001) and references therein.

3. Results

3.1. Investigation of light curves

The PN light curves of the four observations are shown in Fig. 1; these light curves were extracted from a circle with 50″ radius around each source and the temporal binning is 100 s for all sources. Light curves were cleaned (AD Leo, AT Mic, EV Lac) for obvious data dropouts and high proton flare background was subtracted from the light curve (EV Lac). As the PN exposure of AD Leo began during a flare, we included scaled data from the MOS2 exposure, which started ∼1 ks earlier, to show the peak of the flare.

The light curves of the individual targets show obvious variability in all sources. The largest flares that occurred in these observations involve X-ray flux increases of factors $2-3$, which is considered moderate in view of flux increases of factors $10-300$ that have been observed in flares on EQ Peg (Katsova et al. 2002) and EV Lac (Favata et al. 2000a). For an analysis of a larger flare on the M dwarf Proxima Centauri with

Table 3. Selection of flaring data (PN).

	EQ Peg	AT Mic	AD Leo	EV Lac
Median rate	6.42	9.40	8.60	7.58
Min. flare rate	7.0	12.0 (high)	9.5	8.5
		10.0 (med)		
Flare intervals	5.5–11.6	14.7–19.1 (h)	0.0–7.7	0.5–2.3
(ks after		9.7–12.1 (m)	12.2–14.9	8.4–12.2
start of		19.2–25.0 (m)	24.1–25.7	19.4–24.0
observation)			27.4–28.4	
			32.0–33.8	

regularly on timescales of a few hours, these larger events are much rarer.

Weaker flaring (flux changes of around ten percent or lower) on timescales of a few minutes is visible throughout all four observations. In this phase the stars are in a state of low but permanent activity. This continual weak flaring makes it, in addition to the larger flares, difficult to determine a minimum or baseline flux level. This flux or activity level is denoted here as the quasi-quiescent level. It has been suggested that this emission can be interpreted as a superposition of a large number of even smaller flares with a power law distribution (Hudson 1991; Kashyap et al. 2002; Güdel et al. 2003).

The flare light curves exhibit a variety of shapes and often show substructure. The observed rise times are only somewhat shorter than the decay times for the larger impulsive flares during the AT Mic and the EV Lac observation, pointing to relatively compact flaring structures. The different types of flares as observed on the Sun are described in e.g. Feldman et al. (1995) and references therein. The rise times from quasi-quiescent to flare maximum are typically in the range of 1 ks for the largest flares with the rise steepening towards maximum. The binaries are not resolved in these light curves, but all components are expected to be flare stars. For EQ Peg it was shown by Robrade et al. (2004) that both stars contribute to the flaring, with EQ Peg A being brighter than B by a factor of 3−4. The separation of AT Mic is too small to resolve the components.

Flaring involves significant amounts of energy release and matter transfer into the corona and may therefore involve changes in the physical properties of the coronal plasma, e.g. temperatures, emission measures, densities and abundances, a well known phenomenon from previous analyses of stellar flares. Therefore we introduce "flaring" and "quasi-quiescent" phases for each star; an interval is selected as flaring if the count rate of the time bins exceed the median count rate and the peak count rate within the interval exceeds a "minimum flare value", chosen to separate clear flare events and flickering. The selection of two phases of activity is of course somewhat arbitrary, and observations with stronger flares may be separated into three or more phases of in- or decreasing activity. With our data this was only done for the AT Mic observation, which is separated in three states of activity, the quasi-quiescent phase (QQ), the medium activity phase and the outstanding large flare. The count rates, selection criteria and selected flaring periods are summarized in Table 3.

Fig. 1. Light curves of the binaries EQ Peg and AT Mic and the single stars AD Leo and EV Lac; PN (+MOS2/red) data, 100 s binning. Frequent flaring is observed on various timescales; selected flaring periods are indicated by horizontal arrows.

XMM-Newton see Güdel et al. (2004). While our observations indicate that flaring with flux increases of factors 2−3 appears
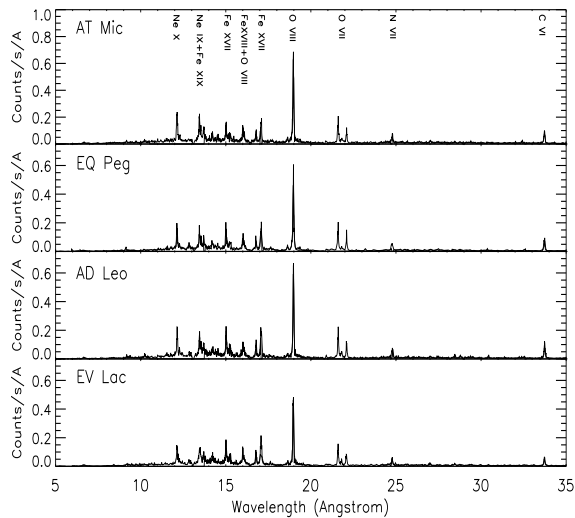
Fig. 2. RGS spectra of the sample stars, the most prominent emission features are labelled.

Fig. 3. PN spectra of the analysed M dwarfs; *top to bottom*: AT Mic (red), AD Leo (green), EV Lac (blue), EQ Peg (black). (*Colour figure in electronic version.*)

3.2. Spectral analysis

3.2.1. RGS and EPIC spectra

The high resolution RGS spectra of our sources in the wavelength range 5−35 Å are shown in Fig. 2. In this energy range the X-ray spectra of our M dwarfs are remarkably similar, all being strongly dominated by emission lines. The positions of the most prominent emission features are labelled; i.e., the H-like lines of C VI, N VII, O VIII and Ne X, the strong He-like triplets of O VII and Ne IX as well as a number of Fe XVII - Fe XIX lines. The peak formation temperatures of these lines cover temperatures from ∼1.5 MK (C VI) over ∼3 MK (O VIII) and ∼6 MK (Ne X) up to ∼8 MK (Fe XIX) but plasma with temperatures up to 30 MK can contribute to these lines.

The EPIC PN data, with moderate spectral resolution, are displayed in Fig. 3 for our target stars; note that the EQ Peg EPIC spectra were extracted from an annulus because of pile up. In addition to the features mentioned in the RGS section the continuum at high energies and lines due to highly ionized iron (up to Fe XXV at 6.7 keV) and H-like/He-like magnesium, silicon and sulfur are detectable. The observed features cover roughly the temperature range from 2 to 70 MK in terms of peak formation temperatures. Inspection of the PN spectra of the sample M dwarfs shows differences in the high energy slopes, the obviously shallower slope of the AT Mic spectrum indicates the higher coronal temperatures of this source.

3.2.2. Spectral fits and coronal temperatures

Closer inspection of the M-dwarf spectra and their individual lines reveals further differences. To quantify these differences the spectra from each type of detector were fitted separately with the 3-T model and the 6-T model. Integration times of the spectra may differ due to varying exposure times and the influence of high background periods on the individual
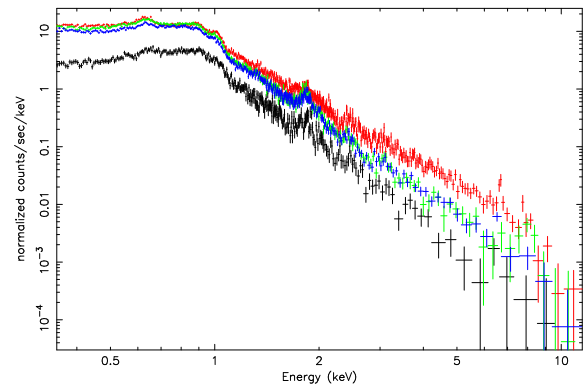
detectors. We examined the influence of flaring on the temperatures, emission measures and abundances of the plasma. For this purpose we extracted spectra from flaring and quasi-quiescent intervals as defined in Table 3 and modelled the PN spectra for the different phases of activity, keeping all model parameters as free parameters. The results of this fitting procedure are summarized in Table 4; all errors denote 90% confidence range and were calculated by allowing variations of all other free model parameters. Note the corrected flux for EQ Peg compared to Robrade et al. (2004). The quality of these fits in terms of the χ^2 test statistic did not improve when further components were added to the model. We point out that the calculated errors are statistical errors only and additional uncertainties are introduced by the atomic data and instrumental calibration.

Comparing the fit results for the different instruments one finds good agreement in general, but deviations of particular results are obvious. One source of uncertainty is based on the interdependence of emission measure (EM) and elemental abundances; a higher EM of a temperature component leads to the reduction of the abundance of elements producing the strongest lines in this temperature range and vice versa. The difference in fit quality between two models is often only marginal. This is especially true for EPIC data, where the best-fitting models result sometimes in higher EM with lower abundances compared to RGS data. However, a combination of these properties is in good agreement, e.g. a simple scaling of the summed EM with the summed abundances of iron and oxygen (see Table 5). Iron and oxygen are the major contributing elements of the emission of M dwarfs in the considered energy range; their abundances can therefore be determined best. Similar results were obtained when using the oxygen abundance for the cooler components and iron for the hotter components. Also the emission measure is in reality a continuous distribution which results in an additional interdependence between temperatures and strength of the respective EM components, noticeably in larger, often dependent, errors affecting neighbouring components. The 3-T and the 6-T model lead to fully-consistent results on abundances for all targets; differences are within the errors and

Table 4. Results on temperatures (keV), emission measures ($10^{51}\,\mathrm{cm}^{-3}$) and abundances relative to solar photospheric values, errors are 90% conf. range. (d.o.f. given in brackets). L_X ($10^{28}\,\mathrm{erg\,s}^{-1}$) indicates the 0.2–10.0 keV luminosity. The 6-T model grid is 0.2, 0.3, 0.6, 1.2, 2.4, 4.8 keV which corresponds to 2.3, 3.5, 7.0, 14.0, 28.0, 56.0 MK.

Par.	RGS	MOS	PN	PN (low)	PN (high)	RGS	MOS	PN	PN (low)	PN (high)
	EQ Peg – 3-T model					EQ Peg – 6-T model				
C	$0.71^{+0.17}_{-0.14}$	–	–	–	–	$0.70^{+0.18}_{-0.13}$	–	–	–	–
N	$0.69^{+0.19}_{-0.16}$	–	–	–	–	$0.68^{+0.22}_{-0.15}$	–	–	–	–
O	$0.54^{+0.09}_{-0.08}$	$0.37^{+0.05}_{-0.04}$	$0.58^{+0.09}_{-0.08}$	$0.70^{+0.18}_{-0.14}$	$0.48^{+0.10}_{-0.07}$	$0.59^{+0.11}_{-0.06}$	$0.37^{+0.06}_{-0.05}$	$0.58^{+0.09}_{-0.08}$	$0.73^{+0.18}_{-0.15}$	$0.48^{+0.08}_{-0.07}$
Ne	$0.96^{+0.16}_{-0.13}$	$0.73^{+0.14}_{-0.12}$	$0.93^{+0.19}_{-0.18}$	$0.92^{+0.32}_{-0.37}$	$1.01^{+0.27}_{-0.22}$	$0.96^{+0.15}_{-0.13}$	$0.69^{+0.09}_{-0.109}$	$1.00^{+0.16}_{-0.13}$	$0.96^{+0.26}_{-0.21}$	$1.11^{+0.20}_{-0.17}$
Mg	$0.30^{+0.14}_{-0.14}$	$0.32^{+0.08}_{-0.07}$	$0.25^{+0.11}_{-0.09}$	$0.22^{+0.19}_{-0.15}$	$0.27^{+0.15}_{-0.11}$	$0.27^{+0.15}_{-0.13}$	$0.33^{+0.08}_{-0.08}$	$0.28^{+0.11}_{-0.09}$	$0.22^{+0.17}_{-0.14}$	$0.33^{+0.14}_{-0.12}$
Si	$0.58^{+0.31}_{-0.29}$	$0.58^{+0.10}_{-0.09}$	$0.40^{+0.12}_{-0.10}$	$0.55^{+0.23}_{-0.18}$	$0.29^{+0.15}_{-0.11}$	$0.56^{+0.34}_{-0.28}$	$0.60^{+0.10}_{-0.11}$	$0.45^{+0.13}_{-0.11}$	$0.58^{+0.23}_{-0.19}$	$0.37^{+0.15}_{-0.13}$
S	$0.27^{+0.18}_{-0.15}$	$0.68^{+0.17}_{-0.16}$	$0.27^{+0.21}_{-0.20}$	$0.63^{+0.40}_{-0.34}$	$0.00^{+0.18}_{-0.00}$	$0.28^{+0.23}_{-0.17}$	$0.69^{+0.18}_{-0.16}$	$0.27^{+0.24}_{-0.22}$	$0.69^{+0.44}_{-0.37}$	$0.00^{+0.17}_{-0.00}$
Fe	$0.46^{+0.08}_{-0.06}$	$0.31^{+0.05}_{-0.04}$	$0.47^{+0.08}_{-0.07}$	$0.54^{+0.16}_{-0.12}$	$0.43^{+0.11}_{-0.07}$	$0.43^{+0.08}_{-0.04}$	$0.32^{+0.05}_{-0.05}$	$0.46^{+0.08}_{-0.06}$	$0.52^{+0.13}_{-0.11}$	$0.45^{+0.09}_{-0.08}$
kT1	$0.26^{+0.01}_{-0.01}$	$0.29^{+0.03}_{-0.02}$	$0.26^{+0.01}_{-0.01}$	$0.27^{+0.04}_{-0.02}$	$0.24^{+0.02}_{-0.02}$	–	–	–	–	–
EM1	$1.62^{+0.32}_{-0.28}$	$2.81^{+0.81}_{-0.53}$	$1.81^{+0.41}_{-0.39}$	$1.63^{+0.81}_{-0.48}$	$2.06^{+0.56}_{-0.54}$	$0.52^{+0.15}_{-0.15}$	$0.17^{+0.37}_{-0.12}$	$0.56^{+0.21}_{-0.20}$	$0.30^{+0.22}_{-0.23}$	$0.96^{+0.37}_{-0.36}$
kT2	$0.63^{+0.02}_{-0.02}$	$0.60^{+0.02}_{-0.02}$	$0.64^{+0.02}_{-0.02}$	$0.64^{+0.10}_{-0.04}$	$0.64^{+0.03}_{-0.03}$	–	–	–	–	–
EM2	$2.18^{+0.36}_{-0.31}$	$3.26^{+0.63}_{-0.66}$	$2.57^{+0.54}_{-0.48}$	$1.70^{+0.68}_{-0.70}$	$3.33^{+0.80}_{-0.82}$	$0.99^{+0.26}_{-0.29}$	$2.88^{+0.63}_{-0.69}$	$1.37^{+0.51}_{-0.46}$	$1.31^{+0.62}_{-0.59}$	$1.37^{+0.70}_{-0.65}$
kT3	$1.20^{+0.14}_{-0.15}$	$1.53^{+0.16}_{-0.12}$	$1.43^{+0.14}_{-0.12}$	$1.35^{+0.13}_{-0.15}$	$1.64^{+0.28}_{-0.21}$	–	–	–	–	–
EM3	$0.96^{+0.18}_{-0.19}$	$1.02^{+0.17}_{-0.18}$	$0.99^{+0.17}_{-0.18}$	$0.94^{+0.23}_{-0.22}$	$1.01^{+0.28}_{-0.28}$	$2.14^{+0.29}_{-0.34}$	$2.82^{+0.50}_{-0.45}$	$2.31^{+0.49}_{-0.45}$	$1.70^{+0.64}_{-0.49}$	$2.74^{+0.78}_{-0.64}$
EM4	–	–	–	–	–	$1.14^{+0.15}_{-0.20}$	$0.92^{+0.23}_{-0.29}$	$0.90^{+0.21}_{-0.20}$	$0.92^{+0.25}_{-0.22}$	$0.77^{+0.32}_{-0.39}$
EM5	–	–	–	–	–	$0.00^{+0.20}_{-0.00}$	$0.27^{+0.10}_{-0.22}$	$0.23^{+0.11}_{-0.15}$	$0.11^{+0.13}_{-0.11}$	$0.44^{+0.18}_{-0.24}$
EM6	–	–	–	–	–	$0.00^{+0.10}_{-0.00}$	$0.00^{+0.10}_{-0.00}$	$0.00^{+0.04}_{-0.00}$	$0.00^{+0.07}_{-0.00}$	$0.00^{+0.10}_{-0.00}$
red. χ^2	1.26 (731)	0.99 (291)	1.17 (365)	0.97 (287)	1.06 (303)	1.29 (731)	0.99 (291)	1.22 (365)	1.00 (287)	1.10 (303)
L_X	5.83	7.25	6.59	5.87	7.30	5.86	7.27	6.61	5.88	7.33
	AT Mic									
C	$0.80^{+0.13}_{-0.11}$	–	–	–	–	$0.79^{+0.13}_{-0.11}$	–	–	–	-
N	$0.65^{+0.13}_{-0.11}$	–	–	–	–	$0.66^{+0.13}_{-0.11}$	–	–	–	–
O	$0.58^{+0.07}_{-0.06}$	$0.37^{+0.04}_{-0.03}$	$0.45^{+0.06}_{-0.04}$	$0.44^{+0.05}_{-0.04}$	$0.46^{+0.09}_{-0.07}$	$0.62^{+0.08}_{-0.06}$	$0.37^{+0.04}_{-0.03}$	$0.43^{+0.03}_{-0.03}$	$0.43^{+0.05}_{-0.04}$	$0.45^{+0.06}_{-0.06}$
Ne	$1.31^{+0.16}_{-0.14}$	$0.83^{+0.08}_{-0.10}$	$0.67^{+0.07}_{-0.09}$	$0.63^{+0.09}_{-0.08}$	$0.72^{+0.24}_{-0.16}$	$1.26^{+0.15}_{-0.14}$	$0.85^{+0.08}_{-0.06}$	$0.78^{+0.05}_{-0.05}$	$0.73^{+0.08}_{-0.07}$	$0.74^{+0.13}_{-0.11}$
Mg	$0.30^{+0.10}_{-0.09}$	$0.24^{+0.05}_{-0.05}$	$0.14^{+0.04}_{-0.04}$	$0.14^{+0.06}_{-0.05}$	$0.13^{+0.09}_{-0.09}$	$0.27^{+0.09}_{-0.09}$	$0.28^{+0.06}_{-0.06}$	$0.20^{+0.04}_{-0.04}$	$0.20^{+0.05}_{-0.06}$	$0.20^{+0.10}_{-0.09}$
Si	$0.40^{+0.19}_{-0.19}$	$0.49^{+0.09}_{-0.08}$	$0.25^{+0.05}_{-0.04}$	$0.28^{+0.07}_{-0.06}$	$0.21^{+0.10}_{-0.09}$	$0.39^{+0.19}_{-0.19}$	$0.47^{+0.08}_{-0.07}$	$0.31^{+0.05}_{-0.05}$	$0.37^{+0.07}_{-0.07}$	$0.28^{+0.11}_{-0.10}$
S	$0.17^{+0.11}_{-0.10}$	$0.44^{+0.14}_{-0.14}$	$0.27^{+0.11}_{-0.11}$	$0.27^{+0.15}_{-0.14}$	$0.11^{+0.24}_{-0.11}$	$0.18^{+0.12}_{-0.11}$	$0.50^{+0.14}_{-0.13}$	$0.22^{+0.11}_{-0.10}$	$0.25^{+0.18}_{-0.15}$	$0.16^{+0.20}_{-0.16}$
Fe	$0.35^{+0.05}_{-0.04}$	$0.18^{+0.03}_{-0.02}$	$0.21^{+0.02}_{-0.02}$	$0.23^{+0.07}_{-0.08}$	$0.20^{+0.06}_{-0.03}$	$0.32^{+0.04}_{-0.04}$	$0.23^{+0.03}_{-0.03}$	$0.23^{+0.02}_{-0.02}$	$0.24^{+0.03}_{-0.03}$	$0.27^{+0.06}_{-0.04}$
kT1	$0.27^{+0.01}_{-0.01}$	$0.36^{+0.04}_{-0.03}$	$0.25^{+0.01}_{-0.01}$	$0.26^{+0.01}_{-0.01}$	$0.24^{+0.02}_{-0.03}$	–	–	–	–	–
EM1	$4.97^{+0.79}_{-0.69}$	$11.20^{+5.64}_{-2.39}$	$7.42^{+1.01}_{-1.60}$	$8.20^{+1.33}_{-1.23}$	$6.50^{+2.30}_{-3.23}$	$0.73^{+0.31}_{-0.26}$	$0.00^{+0.23}_{-0.00}$	$2.61^{+0.54}_{-0.49}$	$2.40^{+0.75}_{-0.65}$	$3.06^{+1.11}_{-1.10}$
kT2	$0.63^{+0.02}_{-0.01}$	$0.60^{+0.18}_{-0.04}$	$0.64^{+0.02}_{-0.01}$	$0.65^{+0.02}_{-0.02}$	$0.62^{+0.03}_{-0.03}$	–	–	–	–	–
EM2	$7.34^{+1.01}_{-0.93}$	$9.19^{+3.26}_{-5.42}$	$16.01^{+2.46}_{-1.49}$	$13.91^{+1.66}_{-1.81}$	$19.15^{+4.75}_{-6.17}$	$4.06^{+0.80}_{-0.78}$	$8.46^{+1.6}_{-1.07}$	$6.58^{+0.96}_{-1.11}$	$6.92^{+1.66}_{-1.81}$	$6.72^{+2.75}_{-2.56}$
kT3	$1.98^{+0.39}_{-0.28}$	$2.06^{+0.27}_{-0.12}$	$2.56^{+0.48}_{-0.19}$	$2.04^{+1.34}_{-1.84}$	$3.00^{+0.04}_{-0.03}$	–	–	–	–	–
EM3	$6.55^{+0.66}_{-0.69}$	$7.93^{+0.71}_{-1.08}$	$5.52^{+0.65}_{-1.09}$	$2.39^{+0.74}_{-0.59}$	$11.86^{+2.78}_{-2.18}$	$7.28^{+1.12}_{-0.96}$	$10.16^{+1.94}_{-1.68}$	$12.71^{+1.60}_{-0.84}$	$11.51^{+2.15}_{-1.33}$	$11.12^{+3.19}_{-2.93}$
EM4	–	–	–	–	–	$1.78^{+1.18}_{-1.15}$	$4.57^{+1.00}_{-1.79}$	$0.84^{+0.72}_{-0.84}$	$1.49^{+0.72}_{-0.72}$	$4.98^{+2.11}_{-2.14}$
EM5	–	–	–	–	–	$4.02^{+2.39}_{-4.02}$	$2.24^{+2.16}_{-1.28}$	$5.74^{+0.99}_{-0.59}$	$1.85^{+0.42}_{-0.32}$	$6.27^{+3.19}_{-3.11}$
EM6	–	–	–	–	–	$2.39^{+3.17}_{-2.39}$	$1.62^{+0.60}_{-0.99}$	$0.21^{+0.47}_{-0.21}$	$0.00^{+0.09}_{-0.00}$	$4.02^{+1.44}_{-1.48}$
red. χ^2	1.15 (1299)	1.39 (231)	1.31 (537)	1.14 (424)	1.10 (511)	1.16 (1299)	1.38 (231)	1.34 (537)	1.23 (424)	1.06 (511)
L_X	22.71	27.64	28.95	23.61	39.65	23.49	27.87	29.01	23.68	39.75

negligible when compared to the uncertainties arising from the use of different detectors.

One effect of calibration uncertainties is that the best fit models of the different detectors do vary in X-ray flux, especially below 1.0 keV. Typical RGS models result in a ~20% lower X-ray flux, mainly in the energy range 0.2–1.0 keV compared to EPIC, whereas the PN models are a few percent more luminous than the MOS models. The RGS luminosities in Table 4 have been extrapolated to the 0.2–10.0 keV band for comparison with the EPIC luminosities. Smaller

Table 4. continued.

Param.	RGS	MOS	PN	PN (low)	PN (high)	RGS	MOS	PN	PN (low)	PN (high)
			AD Leo							
C	$0.83^{+0.10}_{-0.09}$	–	–	–	–	$0.85^{+0.11}_{-0.10}$	–	–	–	–
N	$0.73^{+0.11}_{-0.10}$	–	–	–	–	$0.76^{+0.12}_{-0.10}$	–	–	–	-
O	$0.52^{+0.05}_{-0.05}$	$0.41^{+0.04}_{-0.03}$	$0.45^{+0.04}_{-0.03}$	$0.44^{+0.06}_{-0.05}$	$0.44^{+0.06}_{-0.04}$	$0.58^{+0.06}_{-0.05}$	$0.41^{+0.04}_{-0.03}$	$0.46^{+0.04}_{-0.04}$	$0.47^{+0.06}_{-0.06}$	$0.44^{+0.05}_{-0.04}$
Ne	$1.08^{+0.11}_{-0.10}$	$0.86^{+0.11}_{-0.08}$	$0.68^{+0.07}_{-0.07}$	$0.68^{+0.10}_{-0.11}$	$0.71^{+0.10}_{-0.10}$	$1.07^{+0.12}_{-0.10}$	$0.83^{+0.06}_{-0.05}$	$0.74^{+0.06}_{-0.06}$	$0.71^{+0.10}_{-0.08}$	$0.75^{+0.08}_{-0.06}$
Mg	$0.44^{+0.09}_{-0.09}$	$0.30^{+0.06}_{-0.05}$	$0.14^{+0.04}_{-0.04}$	$0.14^{+0.05}_{-0.05}$	$0.13^{+0.06}_{-0.05}$	$0.41^{+0.08}_{-0.08}$	$0.30^{+0.05}_{-0.05}$	$0.17^{+0.04}_{-0.04}$	$0.15^{+0.06}_{-0.04}$	$0.17^{+0.07}_{-0.05}$
Si	$0.56^{+0.17}_{-0.16}$	$0.67^{+0.08}_{-0.07}$	$0.40^{+0.06}_{-0.05}$	$0.40^{+0.08}_{-0.08}$	$0.41^{+0.09}_{-0.08}$	$0.56^{+0.17}_{-0.17}$	$0.67^{+0.07}_{-0.07}$	$0.45^{+0.06}_{-0.06}$	$0.42^{+0.09}_{-0.07}$	$0.46^{+0.09}_{-0.07}$
S	$0.41^{+0.10}_{-0.09}$	$0.61^{+0.11}_{-0.12}$	$0.36^{+0.12}_{-0.12}$	$0.40^{+0.21}_{-0.18}$	$0.26^{+0.17}_{-0.13}$	$0.46^{+0.12}_{-0.11}$	$0.63^{+0.12}_{-0.12}$	$0.36^{+0.14}_{-0.13}$	$0.43^{+0.22}_{-0.20}$	$0.26^{+0.17}_{-0.14}$
Fe	$0.47^{+0.04}_{-0.04}$	$0.30^{+0.03}_{-0.03}$	$0.27^{+0.03}_{-0.03}$	$0.29^{+0.03}_{-0.03}$	$0.27^{+0.03}_{-0.03}$	$0.44^{+0.05}_{-0.04}$	$0.31^{+0.03}_{-0.02}$	$0.28^{+0.02}_{-0.02}$	$0.29^{+0.03}_{-0.03}$	$0.29^{+0.04}_{-0.03}$
kT1	$0.26^{+0.01}_{-0.01}$	$0.31^{+0.02}_{-0.03}$	$0.24^{+0.01}_{-0.01}$	$0.24^{+0.01}_{-0.01}$	$0.25^{+0.01}_{-0.01}$	–	–	–	–	–
EM1	$1.23^{+0.15}_{-0.14}$	$1.82^{+0.28}_{-0.32}$	$1.63^{+0.21}_{-0.21}$	$1.75^{+0.27}_{-0.30}$	$1.69^{+0.29}_{-0.39}$	$0.29^{+0.12}_{-0.10}$	$0.00^{+0.02}_{-0.00}$	$0.78^{+0.11}_{-0.11}$	$0.83^{+0.14}_{-0.14}$	$0.71^{+0.16}_{-0.17}$
kT2	$0.63^{+0.02}_{-0.02}$	$0.61^{+0.02}_{-0.02}$	$0.62^{+0.01}_{-0.01}$	$0.60^{+0.02}_{-0.02}$	$0.62^{+0.02}_{-0.02}$	–	–	–	–	–
EM2	$1.41^{+0.15}_{-0.13}$	$2.06^{+0.27}_{-0.29}$	$3.22^{+0.30}_{-0.29}$	$2.66^{+0.35}_{-0.27}$	$3.71^{+0.62}_{-0.48}$	$0.85^{+0.13}_{-0.13}$	$1.73^{+0.15}_{-0.19}$	$0.98^{+0.29}_{-0.23}$	$1.00^{+0.35}_{-0.27}$	$1.19^{+0.46}_{-0.36}$
kT3	$1.33^{+0.15}_{-0.10}$	$1.54^{+0.09}_{-0.08}$	$2.18^{+0.50}_{-0.64}$	$2.65^{+2.64}_{-0.23}$	$1.96^{+0.50}_{-0.23}$	–	–	–	–	–
EM3	$0.67^{+0.08}_{-0.09}$	$0.82^{+0.08}_{-0.09}$	$0.43^{+0.10}_{-0.10}$	$0.22^{+0.10}_{-0.010}$	$0.77^{+0.17}_{-0.23}$	$1.40^{+0.17}_{-0.14}$	$2.02^{+0.26}_{-0.24}$	$2.97^{+0.18}_{-0.38}$	$2.50^{+0.30}_{-0.31}$	$3.19^{+0.36}_{-0.55}$
EM4	–	–	–	–	–	$0.64^{+0.12}_{-0.16}$	$0.69^{+0.21}_{-0.13}$	$0.08^{+0.21}_{-0.08}$	$0.00^{+0.22}_{-0.00}$	$0.46^{+0.30}_{-0.21}$
EM5	–	–	–	–	–	$0.00^{+0.27}_{-0.00}$	$0.23^{+0.05}_{-0.09}$	$0.41^{+0.06}_{-0.13}$	$0.21^{+0.10}_{-0.15}$	$0.51^{+0.09}_{-0.29}$
EM6	–	–	–	–	–	$0.09^{+0.16}_{-0.09}$	$0.00^{+0.04}_{-0.00}$	$0.00^{+0.04}_{-0.00}$	$0.00^{+0.09}_{-0.00}$	$0.00^{+0.12}_{-0.00}$
red. χ^2	1.29 (1444)	1.31 (206)	1.27 (442)	1.13 (395)	1.15 (435)	1.30 (1444)	1.31 (206)	1.29 (442)	1.12 (395)	1.17 (435)
L_X	4.12	4.96	5.39	4.71	6.28	4.13	4.97	5.41	4.71	6.30
			EV Lac							
C	$0.51^{+0.08}_{-0.07}$	–	–	–	–	$0.54^{+0.08}_{-0.07}$	–	–	–	–
N	$0.45^{+0.08}_{-0.08}$	–	–	–	–	$0.47^{+0.09}_{-0.08}$	–	–	–	–
O	$0.39^{+0.05}_{-0.04}$	$0.31^{+0.03}_{-0.03}$	$0.34^{+0.03}_{-0.03}$	$0.35^{+0.04}_{-0.03}$	$0.32^{+0.06}_{-0.04}$	$0.45^{+0.05}_{-0.05}$	$0.31^{+0.03}_{-0.03}$	$0.35^{+0.03}_{-0.02}$	$0.36^{+0.04}_{-0.03}$	$0.34^{+0.04}_{-0.04}$
Ne	$0.69^{+0.09}_{-0.08}$	$0.56^{+0.09}_{-0.08}$	$0.48^{+0.05}_{-0.05}$	$0.50^{+0.06}_{-0.06}$	$0.49^{+0.09}_{-0.10}$	$0.68^{+0.08}_{-0.08}$	$0.62^{+0.06}_{-0.05}$	$0.51^{+0.04}_{-0.03}$	$0.52^{+0.05}_{-0.05}$	$0.49^{+0.06}_{-0.06}$
Mg	$0.35^{+0.08}_{-0.08}$	$0.26^{+0.06}_{-0.05}$	$0.16^{+0.03}_{-0.03}$	$0.20^{+0.04}_{-0.03}$	$0.12^{+0.06}_{-0.04}$	$0.31^{+0.08}_{-0.07}$	$0.29^{+0.05}_{-0.05}$	$0.19^{+0.03}_{-0.02}$	$0.22^{+0.04}_{-0.04}$	$0.13^{+0.06}_{-0.04}$
Si	$0.63^{+0.17}_{-0.17}$	$0.49^{+0.08}_{-0.07}$	$0.36^{+0.05}_{-0.04}$	$0.42^{+0.06}_{-0.06}$	$0.30^{+0.07}_{-0.07}$	$0.62^{+0.17}_{-0.17}$	$0.52^{+0.07}_{-0.07}$	$0.40^{+0.04}_{-0.04}$	$0.45^{+0.06}_{-0.06}$	$0.32^{+0.08}_{-0.05}$
S	$0.18^{+0.09}_{-0.08}$	$0.48^{+0.13}_{-0.12}$	$0.32^{+0.10}_{-0.09}$	$0.40^{+0.13}_{-0.13}$	$0.18^{+0.14}_{-0.13}$	$0.21^{+0.10}_{-0.09}$	$0.51^{+0.13}_{-0.12}$	$0.33^{+0.10}_{-0.09}$	$0.41^{+0.12}_{-0.12}$	$0.19^{+0.15}_{-0.12}$
Fe	$0.38^{+0.04}_{-0.04}$	$0.24^{+0.03}_{-0.03}$	$0.24^{+0.02}_{-0.02}$	$0.27^{+0.02}_{-0.02}$	$0.22^{+0.03}_{-0.03}$	$0.35^{+0.04}_{-0.04}$	$0.26^{+0.03}_{-0.03}$	$0.26^{+0.02}_{-0.02}$	$0.28^{+0.02}_{-0.02}$	$0.23^{+0.04}_{-0.02}$
kT1	$0.27^{+0.01}_{-0.01}$	$0.33^{+0.04}_{-0.03}$	$0.25^{+0.02}_{-0.02}$	$0.26^{+0.01}_{-0.01}$	$0.25^{+0.01}_{-0.01}$	–	–	–	–	–
EM1	$1.42^{+0.27}_{-0.21}$	$2.41^{+0.95}_{-0.48}$	$2.01^{+0.27}_{-0.24}$	$2.07^{+0.29}_{-0.27}$	$2.06^{+0.51}_{-0.69}$	$0.23^{+0.08}_{-0.08}$	$0.00^{+0.09}_{-0.00}$	$0.72^{+0.12}_{-0.12}$	$0.63^{+0.13}_{-0.13}$	$0.92^{+0.23}_{-0.24}$
kT2	$0.63^{+0.02}_{-0.01}$	$0.64^{+0.07}_{-0.03}$	$0.61^{+0.01}_{-0.01}$	$0.61^{+0.01}_{-0.01}$	$0.61^{+0.02}_{-0.02}$	–	–	–	–	–
EM2	$2.04^{+0.24}_{-0.25}$	$2.74^{+0.46}_{-0.87}$	$3.62^{+0.30}_{-0.34}$	$3.10^{+0.31}_{-0.31}$	$4.41^{+0.95}_{-0.68}$	$0.99^{+0.21}_{-0.22}$	$2.00^{+0.26}_{-0.27}$	$1.54^{+0.30}_{-0.32}$	$1.69^{+0.35}_{-0.38}$	$1.28^{+0.70}_{-0.37}$
kT3	$1.62^{+0.55}_{-0.27}$	$1.85^{+0.24}_{-0.17}$	$2.18^{+0.30}_{-0.21}$	$2.24^{+0.74}_{-0.39}$	$2.05^{+0.48}_{-0.22}$	–	–	–	–	–
EM3	$0.60^{+0.14}_{-0.14}$	$0.72^{+0.12}_{-0.13}$	$0.53^{+0.11}_{-0.09}$	$0.28^{+0.10}_{-0.09}$	$1.11^{+0.23}_{-0.32}$	$2.11^{+0.25}_{-0.23}$	$2.85^{+0.44}_{-0.38}$	$3.22^{+0.30}_{-0.32}$	$2.74^{+0.41}_{-0.34}$	$4.07^{+0.61}_{-0.82}$
EM4	–	–	–	–	–	$0.42^{+0.17}_{-0.22}$	$0.45^{+0.20}_{-0.21}$	$0.20^{+0.14}_{-0.17}$	$0.12^{+0.15}_{-0.12}$	$0.43^{+0.43}_{-0.15}$
EM5	–	–	–	–	–	$0.00^{+0.49}_{-0.00}$	$0.40^{+0.08}_{-0.19}$	$0.44^{+0.06}_{-0.10}$	$0.24^{+0.06}_{-0.12}$	$0.81^{+0.11}_{-0.05}$
EM6	–	–	–	–	–	$0.26^{+0.19}_{-0.26}$	$0.00^{+0.08}_{-0.00}$	$0.00^{+0.04}_{-0.00}$	$0.00^{+0.04}_{-0.00}$	$0.00^{+0.15}_{-0.00}$
red. χ^2	1.11 (1173)	1.35 (196)	1.32 (479)	1.15 (459)	1.19 (457)	1.12 (1173)	1.40 (196)	1.33 (479)	1.15 (459)	1.20 (457)
L_X	4.26	5.30	5.53	4.96	6.66	4.37	5.31	5.54	4.97	6.68

cross-calibration errors, particularly at energies below 0.5 keV, are also seen in observations made with the same detector but different setups, especially with different filters. Enclosed energy correction from annular extraction regions, necessary for piled-up sources, also influences the measured flux, which can be reduced by up to ~10%. Additional effects are expected for the X-ray flux of the binaries, but in our case they are dominated by one component and/or the separation is small
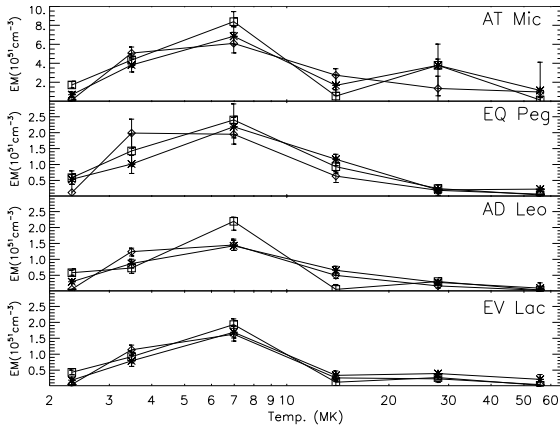
Fig. 4. EMDs as derived with the 6-T model and scaled with the summed abundance of iron and oxygen, total observation each (RGS: Asterisks, MOS: Diamonds, PN: Squares).

Table 5. Deviations of the XMM instruments from the mean scaled summed EM ($\Sigma EM * (A_{Fe} + A_0)[10^{51} \, cm^{-3}]$).

Instr.	EQ Peg	AT Mic	AD Leo	EV Lac
RGS	−5%	+3%	−4%	−5%
PN	+10%	+7%	+9%	+7%
MOS	−5%	−11%	−4%	−3%
sc. Σ EM	4.51	15.32	3.08	2.97

compared to the used extraction region. Calibration efforts are still ongoing, see e.g. Kirsch et al. (2004) for updated XMM-Newton (cross)-calibration.

We note that that the EPIC detectors are not very appropriate to measure changes in the abundance pattern for the different phases of activity as they sometimes result in unphysical solutions like a zero abundance. On the other hand, the RGS is not very sensitive to high temperature plasma and in the 6 -T models applied to RGS data sometimes plasma is put into the hottest components, that is not seen in the EPIC models. Since the contributions from these components in the RGS are also compatible with a zero value, we expect the EPIC models to give a more realistic EMD at these energies. Overall we consider the abundance determination below ~1.5 keV to be more accurate for RGS data, while properties of the hotter plasma are best determined with EPIC data. Therefore we analysed additionally for the different phases of activity the distribution of elemental abundances with RGS data, and the emission measures with PN data using a fixed abundance pattern. The results of flare-related changes will be presented in Sect. 3.3.

The derived temperature structure is consistent among the detectors, independent of the model used, when accounting for the above mentioned uncertainties. The temperature distributions of all sample stars peak consistently around 7−8 MK (1 keV ≡ 11.6 MK) with the bulk of the plasma being located between 2−20 MK for AD Leo, EQ Peg and EV Lac, whereas the AT Mic distribution extends to somewhat higher temperatures. In the EPIC 3 -T models the high temperature

component tends to be hotter and/or stronger compared to RGS.

The EMDs for the total observation of our sample stars as derived from the 6 -T model with the different detectors onboard XMM-Newton are shown in Fig. 4. Undetected components are plotted with their upper limits. The EMDs were scaled with the summed abundance of iron and oxygen and are in good agreement when comparing the individual instruments but individual temperature components are sometimes more pronounced. The shape of the distribution looks similar for our sample stars but the contributions of the hot plasma differ and are strongest for AT Mic, which is also the X-ray brightest source in our sample. AT Mic is associated with the β Pictoris moving group (Barrado y Navascues et al. 1999; Zuckerman et al. 2001), with a probable age of about 10−20 Myr whereas the other stars are members of the kinematic young disk population with ages of the order of 1 Gyr. At this age AT Mic would be a still contracting pre-main sequence system, therefore the stars are larger with higher L_{bol} and because they are in the saturated regime, they have consequently higher L_X.

We also investigated joint fits, where data of different instruments, e.g. RGS and MOS, are fitted simultaneously. While combined fits with datasets of different detectors usually turn out a weighted, intermediate result, this is not the case when taking RGS data in the full energy range and combining it with MOS data above 0.8 or 1.0 keV. This choice is reasonable because the relative energy resolution of the EPIC instruments improves towards higher energies, whereas the effective area of the RGS drops above 1.0 keV. The derived abundances in these fits increase by ~20−30%, whereas emission measure drops, compared to the pure RGS model; the derived temperatures change only marginally. The effect on individual elements and respectively emission measure components slightly depends on the chosen overlap and is similarly observed with PN data. Discarding the RGS data at higher energies, e.g. above 1.5 keV, has only minor influences on the derived models for our stars.

3.2.3. Coronal abundances

The abundance patterns of our sample stars are shown in Fig. 5, where we plot the abundances with respect to solar photospheric abundances against the FIP (First Ionization Potential) of the corresponding element. Here we show the results for the total observation that are constrained best. The data of the individual stars are separated by an offset of one on the vertical axis and a dotted line is plotted at 0.5 solar abundance to guide the eye. For elements with stronger lines in the RGS we accept these values (i.e., for Fe, C, O, N, Ne), for the other elements we use the MOS values, which has a better spectral resolution compared to PN. The higher oxygen values obtained with the solar oxygen abundance given by Allende Prieto et al. (2001) are also plotted, indicating the current uncertainties in the solar abundance pattern. A discussion of problems in determining solar photospheric abundances can be found in Holweger (2001).

The determined metallicities of our sample stars vary only moderately between the individual stars; we do not consider
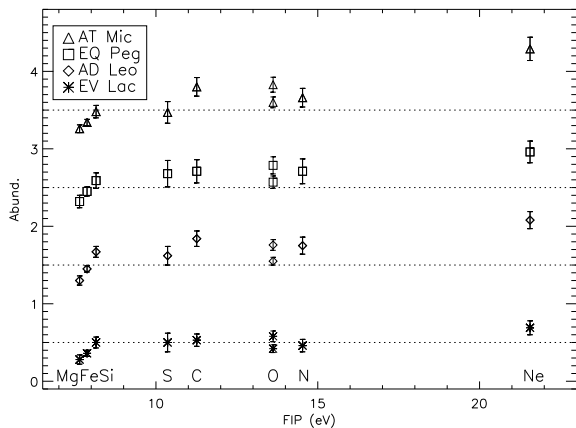
Fig. 5. Elemental abundances in stellar coronae relative to solar photospheric values vs. FIP for our sample stars; an inverse FIP effect is present in all stars. Each star is shifted by one solar abundance on the vertical axis, the dashed lines indicate 0.5 solar abundance in each case.

Fig. 6. Spectra of AT Mic during different states of activity, PN data from selected time-intervals as defined in Table 3 (high: black, medium: green, qq: red). (*Colour figure in electronic version.*)

these differences to be very significant. However, all abundances are subsolar when compared to solar photospheric values. Unfortunately, photospheric abundances for M dwarfs are usually unknown and the rare measurements have large uncertainties. Naftilan et al. (1992) published photospheric abundances for AD Leo, arguing for a metallicity of ∼0.4 solar for the analysed low FIP metals; iron was determined to ∼0.5 solar, in agreement with our coronal measurements but chromospheric contamination could not be ruled out completely. Zboril et al. (1998) published a metallicity of ∼0.6 solar for a number of K and M dwarfs from optical/IR observations. These abundance values are challenging because our sample stars are members of the kinematic young disk population (with AT Mic being even younger), that are fast rotating (Delfosse et al. 1998) and highly X-ray active, which indicates a younger age in contrast to the reduced metallicity one would associate with older stars.

If the photospheric metallicities in our sample stars are indeed as low as suggested by the authors cited above, i.e. in the range 0.4−0.6 solar, the abundances of low FIP elements would actually be consistent with the stellar photospheric values or possibly slightly depleted, while the high FIP elements would actually be enhanced in the coronal material. An overall coronal metal abundance deficiency would then not be present, rather one would find a situation reminiscent of the solar corona, i.e., an enhancement of specific (but different) elements.

When comparing star-to-star variations of abundance as a function of FIP, one finds a tendency that the variations of low FIP elements are smaller than those of high FIP elements, e.g. neon varies by more than 50% compared to iron where the effect is below 10%. Whereas the absolute values differ moderately, the observed abundance pattern looks very similar for all stars. In general, abundance ratios are more robust than absolute values because they are nearly independent of the EM. We already mentioned that while low activity stars show the FIP
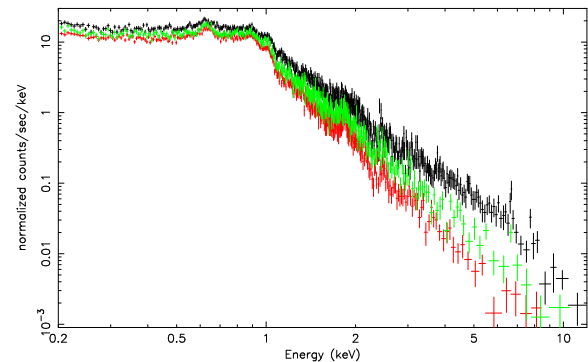
effect more active stars have shown none or an inverse FIP effect (IFIP) (Brinkman et al. 2001; Audard et al. 2003). As a major trend the inverse FIP effect is clearly present in all analysed sources but individual elements show occasional deviations, e.g. carbon, which is mainly determined by the C VI line at the low energy end of the RGS. The IFIP effect is detected with all instruments; however, the strength of the IFIP or abundances of individual elements do vary. This can be mainly attributed to instrumental properties, e.g. the often low abundance of sulfur in RGS fits. Here the detectable lines lie at the high energy end of the detector where the effective area is quite small. The inverse FIP effect is strongest for the most luminous source AT Mic and appears to be correlated with activity. Taking the abundance ratio Ne/Mg as an indicator of the strength of the IFIP effect (since these elements have the largest difference in FIP), we find the largest ratio for AT Mic, intermediate values for AD Leo and EQ Peg and the lowest ratio is found for EV Lac which also exhibits the lowest absolute abundance values. The same trend is observed for other ratios like Ne/Fe or O/Fe and likewise in the results obtained with the MOS detector.

3.3. Flare-related changes

Significant variations in the abundance pattern were not detected with the EPIC data. We also searched for variations with RGS data, which suggests an enhancement of low FIP elements like iron during strong flares, most prominent in the large flare on AT Mic when compared to the quasi-quiescent phase. While the elements with intermediate FIP show no clear trend, the high FIP element neon may also be somewhat enhanced, a trend already found by Raassen et al. (2003). We caution, however, that the measurement errors are large and that a constant abundance pattern is also acceptable within the 90% confidence range derived from the model. This effect is still weaker or undetected for the other sample stars.

In contrast to abundances, emission measures and temperatures of the coronal plasma change significantly. As an example we show the PN spectrum of the AT Mic observation in Fig. 6, separated into the three phases of activity. Not only does the

plasma emission measure increase, but the spectra also harden towards higher activity as more and more emission is found in the higher temperature components during flaring. This is also seen in the growth of the iron lines at 6.7 keV, which are predominantly formed at temperatures above 40 MK.

A quantitative study of the temporal evolution of plasma temperature during flaring was carried out via the emission measure distribution (EMD). Because the most significant changes are expected to be in the high temperature components of the plasma, we used PN data to study the changes of the EMD. For this purpose we use the 6-T model, and keep the abundances fixed at the values as determined from the total observation to derive the EMDs for the different phases of activity. The first two components represent the cool plasma (2−5 MK), followed by the medium temperature plasma (5−20 MK) and the last two account for the hot plasma (20−70 MK).

The observed sources vary in terms of X-ray luminosity and its increase during flaring. The largest increase is found for the most luminous source AT Mic, where the X-ray luminosity during the flare peak phase reaches ~44 × 10^{28} erg s^{-1}; the source brightened by nearly a factor of two for about an hour. AD Leo, EQ Peg and EV Lac are about half an order of magnitude X-ray fainter than AT Mic. A graphical representation of the results on the EMDs of the lower activity stars separated into two different phases of activity (three for the most active source AT Mic) is shown in Fig. 7.

The weakest flaring activity is found on EQ Peg, with changes in EM affecting mainly the medium temperature component. The summed EM of the cool component is constant within errors whereas the medium component increases significantly; typical flare temperatures are around 10−15 MK. The hot component is only marginally detected, contributing only 3% to the EM, and does not appear to be significantly affected by flaring. An intermediate case is observed for AD Leo and EV Lac; here the cool components again stay nearly constant, the medium components increase significantly and the hot component also increases during flaring. The flare temperatures are in the 15−40 MK range. Remarkably the existence of two more separated parts of the EMDs derived from PN data appears also in quasi-quiescence and is similarly found on other temperature grids. However, the respective plasma contributes only a few percent to the total emission measure and the EMDs derived from MOS data are likewise more compact in the sense that the plasma appears to be more concentrated at medium temperatures.

The strongest flaring is observed on AT Mic; here the cooler plasma below the main peak at ~7 MKs is nearly unaffected by the flaring. The main increase is due to the hottest plasma components and large amounts of additional plasma were detected during flaring at temperatures between 15−60 MK. In the low state a second weaker peak is visible in the EMD between 25 and 30 MK, followed by a steep decline towards higher temperatures, indicating no significant amount of plasma above 40 MK. With intermediate conditions during the medium activity phase the plasma distribution during the large flare exceeds 60 MK. The contribution of the hot component to the EMD during the flare is around 25%. The influences of possible changes of the abundance pattern on the EMD are minor and we find
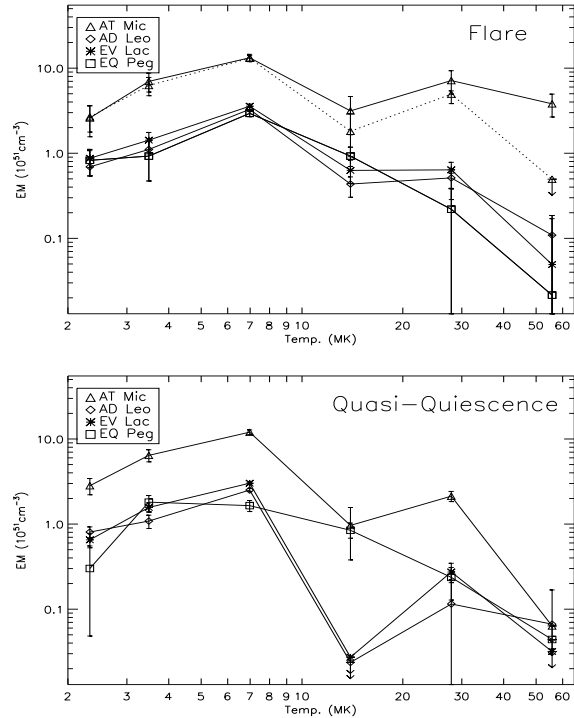
Fig. 7. EMDs of our sample M dwarfs in different states of activity derived from PN data. The upper plot shows the flaring phase, for AT Mic the medium activity phase is additionally plotted as a dashed line while the lower plot shows the quasi-quiescent state. Undetected components are plotted with their upper limits, denoted by downward arrows.

that the basic behaviour and shape of the EMD is comparable for models with free or fixed abundances.

Our analysis of the EMDs shows that flaring does not affect the cool plasma in a significant way. The shape of the EMDs are quite alike at cooler temperatures for all stars and peak at temperatures around 7−8 MK whereas the absolute value correlates with X-ray luminosity. The main influence during flares is found on the amount and temperature of the hotter plasma: stronger flaring and more active stars produce more and hotter plasma. As to the emission of the stars in the quasi-quiescent state a relation between X-ray luminosity and average plasma temperature is suggested while the overall shape of the EMDs is again similar. Only the distribution of binary system EQ Peg, whose EMD is created by two active and slightly different stars (see Robrade et al. 2004), appears broader in all detectors. A hot tail is quite common, sometimes with a second smaller peak, extending to ~30 MK in the EMD. This may indicate the existence of separated plasma components at different temperatures which are located in different coronal structures even in quasi-quiescence, i.e. the main part of the plasma in cooler, more quiescent structures and a smaller amount in hotter and more active structures. These structures would also be a natural explanation for the constant flickering observed in the light curves.

3.4. Loops

Assuming quasi-static loop-like structures as building blocks for the coronae of M dwarfs the derived EM distributions suggest coronae composed out of different loop components with different temperatures. Using the RTV scaling law (Rosner et al. 1978) for simple loops in hydrostatic equilibrium and with constant pressure and cross-section, and the densities derived by Ness et al. (2004), we are able to calculate the size of the loops. In cgs units we obtain:

$$n_{\rm e}L = 1.3 \times 10^6 \, T_{\rm max}^2,$$

with the electron density $n_{\rm e}$, the loop top temperature $T_{\rm max}$ and the (semi) loop length L. The typical electron densities of our sample stars in $\log(n_{\rm e})$ as measured from the O VII triplet are around 10.5, and for the Ne IX triplet in the range 11.1−11.5, but for Ne IX the errors are about 0.5 translating into a factor of three in linear units. The O VII triplet traces plasma around 2 MK, the Ne IX triplet plasma around 4 MK, thus indicating denser plasma at higher temperatures. However both triplets trace only the relatively cool plasma since we find average coronal temperatures of about 10 MK for the less active stars and 15 MK for AT Mic from the EMDs, in good agreement with the values calculated with a scaling law correlating X-ray luminosity and stellar radius (R_*) with average temperature (Ness et al. 2004). While the assumptions of quasi-static loops and the measured densities can be well justified for the cooler and the quiescent components, results for the hotter plasma should be taken as upper limits, especially when taking into account the plausible higher density of the hotter plasma.

Assuming stellar radii of 0.35/0.3 solar radius for spectral type M3.5/M4.5 and for the binaries for simplicity one dominant component, we determine loop lengths for the coolest plasma (2−5 MK) below $0.01\,R_*$ on all stars. Taking the mean plasma density derived from neon, the loop lengths are about $0.03−0.07\,R_*$ for the average coronal temperature of our stars and increase up to $0.3\,R_*$ for the hotter plasma components. Ness et al. (2004) find the density of the hotter plasma consistent with the low density limit ($\log n_{\rm e} \approx 12.7$) for the used line ratios of Fe XXI, so an higher density as the one derived from Ne IX in the hotter loops would further scale down the determined loop length according to the above scaling law; instead of an increased loop size, an increased density also can explain the observed temperatures. Repeating the calculations with the low density limit of Fe XXI, we derive lower limits for the length of the hotter loops, which are scaled down by a factor of 20 compared to the above derived results. Therefore we conclude that the dominating coronal structures for the cool plasma are very small, i.e. $L < 0.01\,R_*$, for the medium temperature plasma small in the sense that $L < 0.1\,R_*$ and still compact ($L \lesssim 0.3\,R_*$) for the hotter plasma observed here. Favata et al. (2000a) studied AD Leo data from various missions, analysed decay times of flare loops and likewise found its corona to be compact, even for flare structures.

In this picture the cool emission is produced in relatively small loops nearly unaffected by flaring, while medium and hot temperature loops are larger, probably have higher densities and are more numerous on more active stars or during flares.

3.5. Comparison with other results

We compare our results with other measurements and earlier works to check the consistency of the derived results and to investigate long-term behaviour. We find that the results presented here agree well with other analyses, which often used different techniques or dealt with individual objects only, leading to a rather consistent picture of the X-ray properties of active M dwarfs as a class and demonstrate the robustness of the results.

Comparison of the measured fluxes of our sample stars with e.g. the ROSAT all-sky survey values (Hünsch et al. 1999) shows agreement to within a factor less than two. This is of the same order as the variations found during the moderate activity in the XMM-Newton observations, demonstrating the stability of the X-ray emission. Favata et al. (2000a) studied the quasi-quiescent corona of AD Leo from various missions and found the X-ray luminosity to be remarkable constant with variations less than a factor of two, suggesting the absence of strong cyclic variations; our results agree well, expanding the time period of the observations to over 20 years. The X-ray luminosity of EQ Peg determined in this work agrees likewise with the measurements made with *Einstein* more than 20 years ago. Combined, these findings establish long term stability of the quasi-quiescent corona for active M dwarfs in general.

Comparing our results with previous analysis of the XMM-Newton data, our AD Leo results are in good agreement with those obtained by Besselaar et al. (2003), who also applied the global fitting approach, especially when considering the different spectral code and model, atomic database and of course the X-ray dataset used in the analyis. The same is true for the AT Mic results presented in Raassen et al. (2003) with a similar analysis; note that errors stated in these publications are only 1σ. Discrepancies concerning the absolute values of emission measure and abundances are explained by their mutual interdependence, and a combination, e.g. the product, of these properties is in much better agreement. Concerning the shape of the DEM, which is determined there with polynomial methods from MOS and RGS data, results are comparable with our EMD based on multi-temperature fits of PN data.

Maggio et al. (2004) presented a line-based analysis of AD Leo data taken with *Chandra* LETGS and also found the inverse FIP effect. However, they determined the iron abundance from the line-to-continuum ratio in the low-count spectrum to be almost as high as that in the solar photosphere. Consequently, nearly all other elements, which are scaled with the iron abundance, appear to be supersolar. On the other hand, Favata et al. (2000a) determined the iron abundance from ASCA data to ~0.2 solar, low but comparable to our EPIC values. While the abundances determined with medium resolution spectroscopy are apparently often low, the results obtained with the global fits of high resolution data in our work or in Besselaar et al. (2003) appear more reliable. We also point out that our joint fit approach, which uses a data selection comparable to Audard et al. (2004), who obtained consistent results on the abundances with line-based and global models applied to high resolution X-ray spectra, results in slightly increased but still significant subsolar abundance values.

Whereas the global metallicities were not determined uniquely in the various analysis, the inverse FIP effect is consistently found in all analysis of active M dwarfs, despite the fact that different spectral models and atomic codes were applied to medium and high resolution X-ray data, demonstrating that the inverse FIP effect is certainly a robust result.

4. Summary and conclusions

We have carried out a comparative analysis of XMM-Newton observations of M dwarfs with spectral type M3.5 – M4.5, i.e., AT Mic, EQ Peg, AD Leo and EV Lac. Light curves revealed frequent flaring of all observed sources on different timescales and with various strengths of the individual flares. While AD Leo, EQ Peg and EV Lac are comparable with respect to activity and X-ray brightness, the probably younger system AT Mic is half an order of magnitude X-ray brighter. From X-ray spectroscopy, abundance patterns and emission measure distributions were derived for the sample stars and for different states of activity. We find that many X-ray quantities, like the coronal temperature structure and the abundance pattern of the analysed M dwarfs are very similar despite the fact that the X-ray luminosity and flaring behaviour differs significantly.

All analysed M dwarf coronae show the inverse FIP effect, demonstrated in this work for the first time for EQ Peg and EV Lac, establishing this effect for the coronae of active M dwarfs as a class. The determined abundances are lower than solar photospheric abundances; however, the few available measurements of stellar photospheric metallicities for M dwarfs also point to subsolar values, comparable with our coronal measurements. This suggests that a strong coronal metal abundance deficiency may actually not be present in our sample stars. Properties like X-ray brightness, temperature of the flare plasma and thus hardness of the X-ray spectrum are highest for the most active source AT Mic, and increase during flares for all observed sources, suggesting a correlation between these properties and activity. The strength of the inverse FIP effect is also greatest in AT Mic, but does not increase during flaring. Time-resolved abundance analysis suggests that preferably low FIP elements are enhanced during flares, but this finding is not statistically significant.

We find from the derived EMDs of the stars that the plasma temperature structures of the coronae are similar, with a maximum at $7-8$ MK and a hot tail with a stronger contribution of hotter plasma in the X-ray brighter stars. The emission measures of the hotter plasma components increase significantly during flares and higher temperatures are reached in stronger flares, while the cool plasma is only marginally affected by flaring. Assuming that the coronae are composed of loop-like structures, this indicates a distribution of structures in which the cooler plasma is confined in many smaller loops while other, presumably larger and denser loops, dominate the additional hot emission generated by flare events. The coronae are found to be compact, i.e. the largest loop lengths are smaller than one third stellar radius.

From comparison with older measurements we conclude that the global X-ray properties show long-term stability while short time-scale behaviour is characterised by frequent variations on top of a level of "baseline activity". With the XMM-Newton data we are able to investigate the X-ray properties of stellar coronae to a previously unknown precision. As these observations provide only a snapshot in the life of a few M dwarfs, larger samples or longer observations may show more extreme or different phenomena. Nevertheless, the consistency and congruence makes our results appear typical for active M dwarfs.

References

Allende Prieto, C. A., Lambert, D. L., & Asplund, M. 2001, ApJ, 556, L63

Anders, E., & Grevesse, N. 1989, Geochim. Cosmochim. Acta, 53, 197

Arnaud, K. A. 1996, ASP Conf. Ser., 101, 17

Audard, M., Güdel, M., Sres, A., et al. 2003, A&A, 398, 1137

Audard, M., Telleschi, A., Güdel, M., et al. 2004, ApJ, 617, 531

Barrado y Navascues, D., Stauffer, J. R., Song, I., & Caillault, J.-P. 1999, ApJ, 520, L123

van den Besselaar, E. J. M., Raassen, A. J. J., Mewe, R., et al. 2003, A&A, 411, 587

Brinkman, A. C., Behar, E., Güdel, M., et al. 2001, A&A, 365, L324

Delfosse, X., Forveille, T., Perrier, C., & Mayor, M. 1998, A&A, 331, 581

Ehle, M., Breitfellner, M., Gonzales Riestra, M., et al. 2003, XMM-Newton User's Handbook

Ehle, M., Pollock, A. M. T., Talavera, A., et al. 2004, User's Guide to XMM-Newton Science Analysis System

Favata, F., Reale, F., Micela, et al. 2000a, A&A, 353, 987

Favata, F., Micela, G., & Reale, F. 2000b, A&A, 354, 1021

Feldman, U., Seely, J. F., Doschek, G. A., et al. 1995, ApJ, 446, 869

Fuhrmeister, B., Schmitt, J. H. M. M., & Wichmann, R. 2004, A&A, 417, 701

Grevesse, N., & Sauval, A. J. 1998, Space Sci. Rev., 85, 161

Güdel, M., Audard, M., Briggs, K., et al. 2001, A&A, 365, L336

Güdel, M., Audard, M., Kashyap, V. L., et al. 2003, ApJ, 582, 423

Güdel, M., Audard, M., Reale, F., et al. 2004, A&A, 416, 713

Holweger, H. 2001, AIPC, 598, 23

Hudson, H. S. 1991, SoPh, 133, 357

Hünsch, M., Schmitt, J. H. M. M., Sterzik, M. F., et al. 1999, A&AS, 135, 319

Kahn, S. M., Linsky, J. L., Mason, K. O., et al. 1979, ApJ, 234, L111

Kashyap, V. L., Drake, J. J., Güdel, M., & Audard, M. 2002, ApJ, 580, 1118

Katsova, M. M., Livshits, M. A., & Schmitt, J. H. M. M. 2002, ASP Conf. Proc., 177, 515

Kenyon, S. J., & Hartmann, L. 1995, ApJS, 101, 117

Kirsch, M. G. F., Altieri, B., Chen, B., et al. 2004 [arXiv:astro-ph/0407257]

Laming, J. M., Drake, J. J., & Widing, K. G. 1995, ApJ, 443, 416

Maggio, A., Drake, J. J., Kashyap, V., et al. 2004, ApJ, 613, 548

Naftilan, S. A., Sandmann, W. S., & Pettersen, B. R. 1992, PASP, 104, 1045

Ness, J.-U., Schmitt, J. H. M. M., Burwitz, V., et al. 2002, A&A, 394, 911

Ness, J.-U., Güdel, M., Schmitt, J. H. M. M., et al. 2004, A&A, 427, 667

Parker, E. N. 1988, ApJ, 330, 474

Proquet, D., Mewe, R., Dubau, J., et al. 2001, A&A, 376, 1113

Raassen, A. J. J., Mewe, R., Audard, M., & Güdel, M. 2003, A&A, 411, 509

Robrade, J., Ness, J.-U., & Schmitt, J. H. M. M. 2004, A&A, 413, 317

Rosner, R., Tucker, W. H., & Vaiana, G. S. 1978, ApJ, 220, 643

Sanz-Forcada, J., Maggio, A., & Micela, G. 2003, A&A, 408, 1087

Schmitt, J. H. M. M., & Rosso, C. 1988, A&A, 191, 99

Schmitt, J. H. M. M., & Liefke, C. 2004, A&A, 417, 651

Schmitt, J. H. M. M., Fleming, T. A., & Giampapa, M. S. 1995, ApJ, 450, 392

Smith, R. K., Brickhouse, N. S., Liedahl, D. A., & Raymond, J. C. 2001, ASP Conf. Ser., 247, 161

Sciortino, S., Maggio, M., Favata, F., & Orlando, S. 1999, A&A, 342, 502

Stauffer, J. R., & Hartmann, L. W. 1986, ApJS, 61, 531

Vaiana, G. S., Cassinelli, J. P., Fabbiano, R., et al. 1981, ApJ, 244, 163

Zboril, M., Byrne, P. B., & Rolleston, W. R. J. 1998, MNRAS, 299, 753

Zuckerman, B., Song, I., Bessell, M. S., & Webb, R. A., ApJ, 562, L87

Chapter 3

Spatially resolved X-ray emission of EQ Pegasi

J. Robrade, J. - U. Ness and J. H. H. M. Schmitt

Astronomy
&
Astrophysics

Spatially resolved X-ray emission of EQ Pegasi

J. Robrade, J.-U. Ness, and J. H. M. M. Schmitt

Hamburger Sternwarte, Universität Hamburg, Gojenbergsweg 112, 21029 Hamburg, Germany

Abstract. We present an analysis of an XMM-Newton observation of the M dwarf binary EQ Pegasi with a special focus on the spatial structure of the X-ray emission and the analysis of light curves. Making use of data obtained with EPIC (European Photon Imaging Camera) we were for the first time able to spatially resolve the two components in X-rays and to study the light curves of the individual components of the EQ Peg system. During the observation a series of moderate flares was detected, where it was possible to identify the respective flaring component.

Key words. stars: binaries: visual – stars: individual: EQ Peg – stars: flare – X-rays: stars

1. Introduction

X-ray observations with the *Einstein Observatory* and ROSAT have shown the ubiquitous occurrence of coronae around most classes of stars. ROSAT studies of volume-limited complete samples of cool stars in the immediate solar neighborhood have shown coronal formation around late-type cool dwarf stars with outer convection zones to be universal; all stars investigated with sufficient sensitivity were found to be surrounded by X-ray emitting coronae (Schmitt et al. 1995; Schmitt & Liefke 2003). Interestingly, fully convective M dwarfs have also been found to be very active with frequent flares.

EQ Peg is a nearby (6.25 pc) visual binary (period ~180 yr, separation 5.2″) consisting of two M dwarfs of spectral type M3.5 and M4.5. It was first observed photoelectrically to flare by Roques (1954), and Owen et al. (1972) found both components of the system to be flare stars.

EQ Peg has been observed at radio, optical, EUV, and X-ray wavelengths. Observations in the optical focused on the flare nature of EQ Peg and marked emission line variability during photometric quiescence was found (Bopp 1974) as well as frequent optical flares on both components (Rodonò 1978). A VLA map of EQ Peg at 6 cm was presented by Topka & Marsh (1982). They resolved both components and interpreted the radio emission as "quiescent" since they found it unlikely that both components flared at the same time. The radio emission was confined to each component and Topka & Marsh (1982) concluded that radio production mechanisms do not depend on binary interaction (which is plausible due to the separation of ~25 AU).

EQ Peg was observed by all major previous imaging X-ray missions and again found to flare frequently. EQ Peg was observed with the *Einstein Observatory* (Vaiana et al. 1981) and is

contained in the ESS (Einstein Slew Survey) (Elvis et al. 1992). EXOSAT detected an intense long duration flare during a co-ordinated observation with the VLA (Pallavicini et al. 1986); a detailed modelling of these flares and the underlying physical properties is presented by Polotto et al. (1988). EQ Peg was also detected in the ROSAT all-sky survey (Hünsch et al. 1999) and rapid flaring was simultaneously observed at optical and X-ray wavelength with MEKASPEC and ROSAT (Katsova et al. 2002), where the source brightened in X-rays by a factor of ~15. A coordinated VLA, optical, EUVE, and RXTE monitoring of EQ Peg was carried out by Gagné et al. (1998). They found a classic stellar flare with a rapid impulsive phase (radio burst) followed by rapid chromospheric heating and cooling (*U*-band) and more gradual coronal cooling (X-ray and extreme-UV). In addition they found atypical flares with either highly polarized emission with no counterparts at shorter wavelengths or moderately polarized flares that often have shorter-wavelength counterparts.

EQ Peg was also observed with XMM-Newton. In Sect. 2 we describe the observations and the methods used for data analysis. Here we focus on the data from the EPIC instruments in order to obtain spatial and temporal information on the two components of EQ Peg. In Sect. 3 we present the results followed by a summary and discussion in Sect. 4.

2. Observation and data analysis

EQ Peg A/B (*V* = 10.32 mag/12.4 mag) was observed on 2000 July 9 (MJD = 51734) with XMM-Newton. The 15 ksec observation of EQ Peg (see Table 1) provided useful data in all EPIC (European Photon Imaging Camera) detectors. The EPIC instrument consists of three CCD cameras with two different types of CCD design, resp. two MOS (Metal Oxide Semi-conductor CCDs) and one PN (pn CCDs), providing imaging and spectroscopy. The EPIC cameras offer the

Table 1. Observation log of EQ Peg.

Instrument (Mode)	Duration (s)	Obs-time
MOS (FF, thick F.)	14 600	2000-07-09T11:39:13-15:42:32
PN (FF, thick F.)	12 410	2000-07-09T12:20:16-15:47:05

possibility to perform extremely sensitive imaging observations over the telescope's field of view of 30′ and in the energy range from 0.15 to 15 keV with good angular and moderate spectral resolution. A detailed description of the XMM instruments can be found in Ehle et al. (2003). All EPIC instruments (MOS/PN) operated in the full frame mode with the thick filter inserted. Unless otherwise indicated we used for our purposes the full energy bandpass of the EPIC instruments, resp. 0.15 keV to 12.0/15.0 keV.

The data were reduced with the standard XMM-Newton Science Analysis System (SAS) software, version 5.4.1. Light curves and images were produced with standard SAS tools and standard selection criteria were applied for filtering the data. In Fig. 1 we show the image obtained with the MOS1 detector. The image looks elongated and it is reasonable to assume the elongation is due to emission from both components of EQ Peg. The image elongation can be seen clearly in MOS1, but not in MOS2 and PN due to the triangular shape of the point spread function (PSF) for MOS2 and the bigger pixel size in PN.

For a quantitative analysis of the MOS1 image we developed a fitting procedure applicable to the measured event distribution in order to confirm the detection of the two components of EQ Peg and to determine accurate source positions and count rates. For this procedure we optimize a set of parameters describing the modelled event distribution on the sky plane. The modelled event distribution is constructed on the basis of the PSF (Kirsch 2002), which is composed of a King component plus background

$$\text{PSF} = \frac{A}{\left(1 + \left(\frac{r}{r_c}\right)^2\right)^\alpha} + \text{BKG} \qquad (1)$$

with the core radius r_c, the slope α (model parameters), the distance to the peak position r, and the amplitude A (source parameters). The background flux BKG was determined from source free regions in the detector and is kept as a fixed model parameter. We place two such King components near the positions of the two sources and apply an optimization algorithm seeking best-fit values for the amplitudes A_1 and A_2 and the positions $r_1 = (x_1, y_1)$ and $r_2 = (x_2, y_2)$ of each component. We thus determine the model counts in the spatial bin (i, j)

$$\boldsymbol{n}_{i,j} = \frac{A_1}{\left(1 + \left(\frac{r_1 - r_{i,j}}{r_c}\right)^2\right)^\alpha} + \frac{A_2}{\left(1 + \left(\frac{r_2 - r_{i,j}}{r_c}\right)^2\right)^\alpha} + \text{BKG} \qquad (2)$$

and apply Powell's algorithm (Press et al. 1999), a robust multidimensional minimizing routine, in order to minimize the likelihood function

$$\mathcal{L} = -2 \sum_{i,j} \log \left(\boldsymbol{n}_{i,j} * \boldsymbol{c}_{i,j} - \boldsymbol{n}_{i,j}\right) \qquad (3)$$
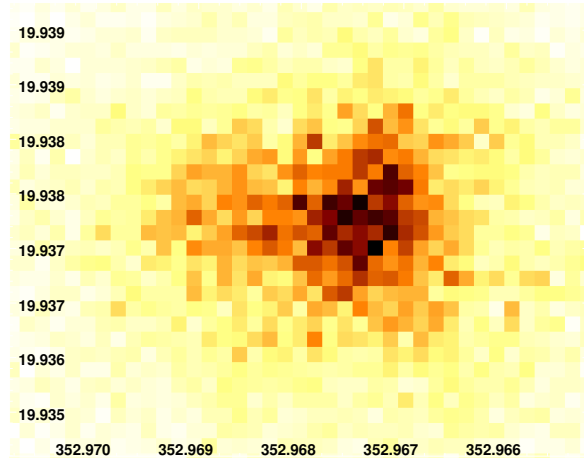
Fig. 1. Image of the EQ Peg system (MOS1) with linear brightness scaling. The image is elongated, suggesting the presence of two components. Analysis shows that the X-ray brighter component is EQ Peg A.

with the measured counts $\boldsymbol{c}_{i,j}$ and model counts $\boldsymbol{n}_{i,j}$. The model counts $\boldsymbol{n}_{i,j}$ are constrained to conserve the total number of counts, i.e., $\sum_{i,j} \boldsymbol{n}_{i,j} = \sum_{i,j} \boldsymbol{c}_{i,j}$.

The mean PSF-parameters (r_c and α) as determined by inflight calibration (Ghizzardi 2001) did not lead to good fit results for our EQ Peg data. It turned out that especially for the value of the core radius (r_c) binning and pile-up effects have to be considered, while the variation of the slope α is only moderate. In order to find a better representation for the shape of the PSF we carried out a parameter study for our data from EQ Peg and for XMM-Newton observations of single point sources, e.g., ϵ Eri with a comparable detector configuration and pile-up level. From this study we found a slope of $\alpha = 1.45$, which agrees with the calibration value, and a value for the core radius of $r_c = 4.45$, i.e., a reduction of ∼20%, to be better suited to model our data.

With the redetermined PSF parameters we modelled the event distribution. In Fig. 2 we show a one-dimensional representation of our fit results for the EQ Peg observation. For this purpose we integrated along the declination axis, which almost matches the main axis of the EQ Peg system and binned the data into a histogram. As can be seen in Fig. 2, the model describes the data very well.

3. Results

3.1. Determination of exact source positions

A first inspection of Fig. 1 suggests the presence of two sources. Since the angular resolution of the MOS1 detector is of the same order as the separation of the two components of EQ Peg (∼5″), it is clear that we are operating at the limit of the spatial resolving power of the MOS1 detector. We applied our PSF algorithm to the EQ Peg dataset to determine precise source positions. We use the MOS1 data from a 50 × 50″ field centered on the position of the EQ Peg system. The calculated
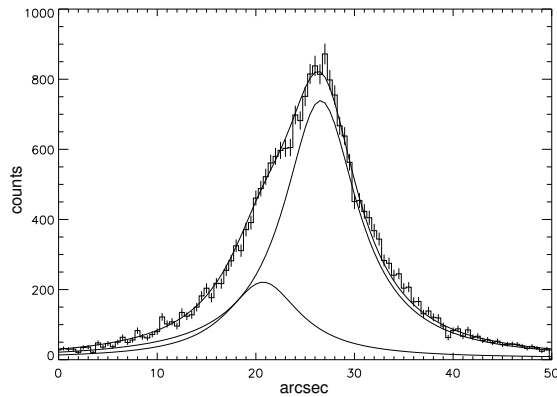
Fig. 2. The event distribution of EQ Peg, fitted with the PSF model. Shown are the individual components as well as the sum of both components compared to the data (histogram).

Table 2. Position fit results (1 σ errors), ref. data from Simbad (FK5/2000).

	EQ Peg A		EQ Peg B	
	Fit	Ref.	Fit	Ref.
RA (23:31:)	52.17 ± 0.01	52.18	52.57 ± 0.02	52.53
	(352.9674°)		(352.9690°)	
Dec (+19:56:)	14.10 ± 0.05	14.10	14.05 ± 0.10	13.90
	(19.9373°)		(19.9372°)	
EQ Peg System	Fit		Ref.	
Separation (″)	6.0 ± 0.3		5.2	
Count ratio A/B	3.4 ± 0.2	4.2 ± 0.3 (quies.)	2.9 ± 0.2 (flare)	

source positions as listed in Table 2 agree well within the errors with the optical positions taken from literature (Perryman et al. 1997). Here proper motion corrections were not applied since they are small because the observation took place in July 2000. We therefore conclude that we indeed identified the two X-ray sources with the optical counterparts.

The algorithm was also used to determine the absolute number of counts per source and the count ratio of the sources. EQ Peg A was on average a factor of ~3.5 brighter than EQ Peg B during the total observation.

3.2. Identification of flare activity

From the image obtained with MOS1 the two components of EQ Peg can be separated. In Fig. 3 we plot the light curves for the EQ Peg system as observed with the different EPIC detectors. Inspection of the total light curves in Fig. 3 shows that the EQ Peg system stayed more or less quiet during the first 8 ksec, afterwards a rise in count rate is detected in all three detectors. We therefore divided the data set into two parts separated at $t = 7.86$ ksec where we consider the first part the quiescent phase and the second part the flaring phase.

In Fig. 4 we display the event distributions of these two subsets; the histograms were created in the same way as in Fig. 2 and are corrected for the different integration times. Here EQ Peg A is the X-ray brighter component on the right, EQ Peg B corresponds to the weaker component on the left
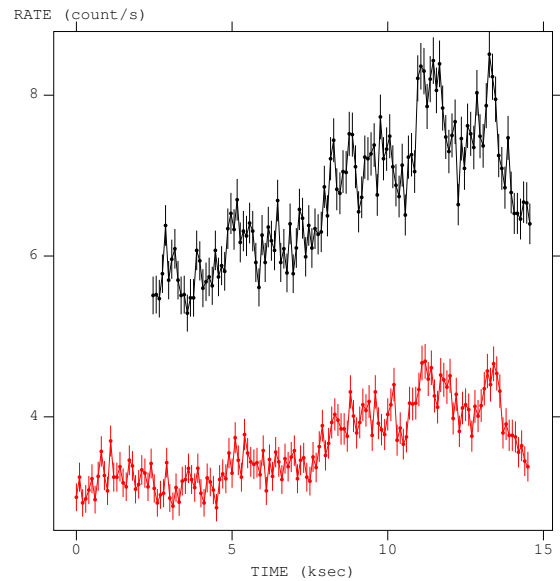
Fig. 3. Light curve of the EQ Peg observation as measured by the PN (black) and MOS1+2 (grey) detectors with 100 s binning.
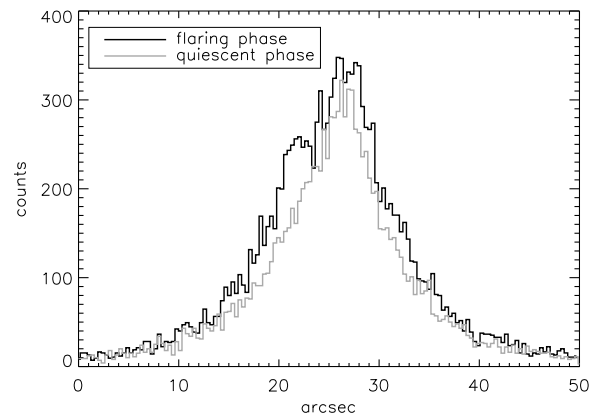
Fig. 4. Comparison of the event distribution during the quiescent and flaring phase.

edge of the event-distribution. In the quiescent phase EQ Peg A dominates the emission and the second component is only marginally visible, while during the flaring phase EQ Peg B brightens up and becomes more clearly visible.

The analysis of the X-ray images as carried out for the total observation (Sect. 3.1) can be repeated for the different phases of activity. Application of our PSF algorithm to the two subsets with variation of only the amplitude parameters returned the count rate of EQ Peg A to be a factor ≳4 higher than for EQ Peg B in the quiescent phase, while in the flaring phase the ratio was ≲3. The results of the fitting procedure for the EQ Peg observation are summarized in Table 2.
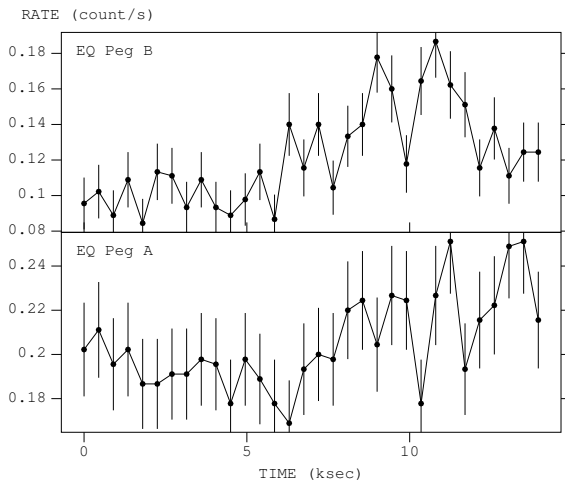
Fig. 5. Light curves of the two components extracted from a circular region around each component.

Fig. 6. Division of the MOS1 light curve into seven time intervals (top) and derived flux ratios (bottom).

Fig. 7. Light curves of EQ Peg B (top) and A (bottom) calculated with the PSF fitting algorithm.

3.3. Reconstruction of individual light curves

Having found that the major flaring activity is due to EQ Peg B, we decided to carry out a systematic light curve analysis of both components of the EQ Peg system. As a first approach we extracted two different light curves from the MOS1 data by placing a circular region with $2.5''$ radius around each component, concentrating on the core of the PSF.

In Fig. 5 we show these light curves binned into 7.5 min bins. Again, EQ Peg B is more variable and its count rate rises by a factor of ~2 at the peak of the flare while EQ Peg A shows only marginal brightening compared to the quiescent emission level. Clearly, the extraction regions used do contain photon contamination from the respective other component due to the wings of the PSF. Nevertheless, the individual light curves also suggest uncorrelated variability between the A and B components. In particular, the flaring at the end of the observations (e.g., $t \gtrsim 11$ ksec) seems to originate from the A component.

For a more detailed quantitative treatment we utilize our PSF algorithm in order to reconstruct the individual light curves. We divide the dataset into seven time intervals covering the various phases of activity as shown in the upper panel of Fig. 6. From our PSF algorithm a count ratio for each time interval can be determined and in the bottom panel of Fig. 6 we show the development of this count ratio. While the main flaring activity is located on EQ Peg B (indicated by the decrease of the A/B count ratio after ~5 ksec) there is also some activity on EQ Peg A especially during the later phase of the observation.

From these ratios we calculated light curves for each individual component, which are shown in Fig. 7. Although the light curves consist of rather large time bins the main features visible in Fig. 5 are also present, i.e., a flare on EQ Peg B around 10 ksec and the flaring activity on EQ Peg A towards the end of the observation. The rise in count rate associated with the flare activity on both components is nearly equally strong,
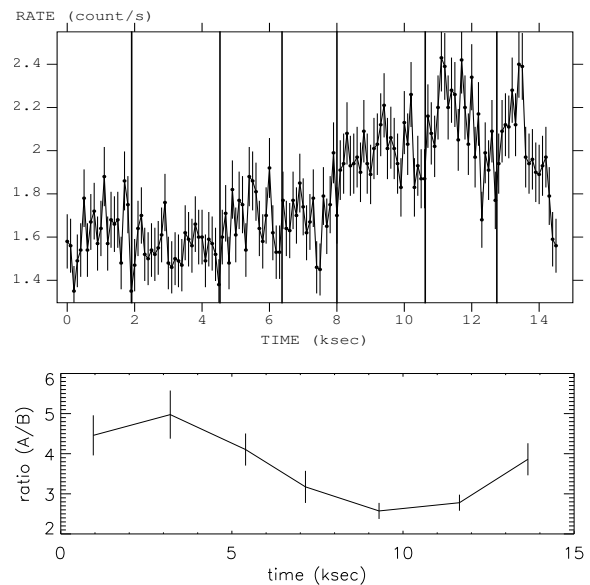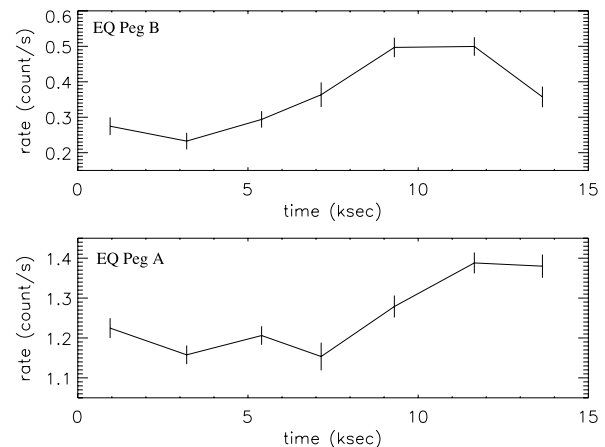
i.e., ~0.2 counts/s, however, the relative change in count rate is much higher on EQ Peg B.

3.4. Development of the spectral hardness

In order to quantify eventual changes in the physical conditions accompanied by rising count rates we calculate a spectral hardness ratio for the sum of both components in two energy bands, resp. 0.2−0.5 keV (soft) and 1.0−10.0 keV (hard). The hardness ratio was calculated from PN data which were cleared for pile-up effects.

In Fig. 8 we show the spectral hardness ratio (hard/soft) for this observation binned every five minutes vs. the measured count rate. The hardness ratio increases during the times where
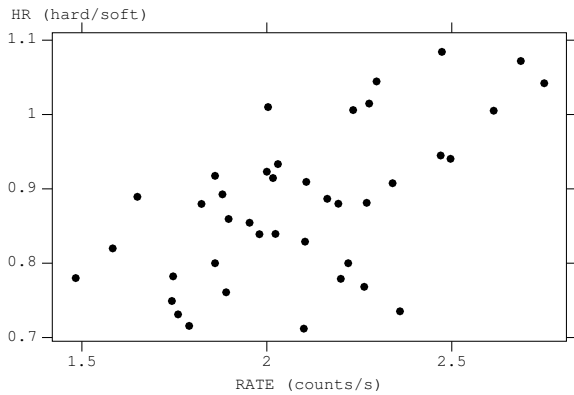
Fig. 8. Hardness ratio ($1-10$ keV/$0.2-0.5$ keV) derived from PN data vs. count rate.

we also observe increases in count rate. We calculated a linear correlation coefficient and found a correlation probability of 99.9%. We therefore interpret the simultaneous increase in count rate and hardness of the emission as flare heating of the coronal plasma. When comparing the calculated average hardness ratios during the time intervals defined in Sect. 3.2 as the quiescent phase and the flaring phase we find an increase in hardness by 12 ± 2% from the quiescent phase into the flaring phase, whereas the increase during individual flares is substantially stronger.

The average X-ray luminosity between 0.2 keV and 10.0 keV was calculated to be 4.2×10^{28} ergs/s from application of spectral models. We compared the X-ray luminosities obtained from a number of different reasonable models and find consistent results. In comparison with previous measurements the energy flux during this observation was $\sim$20% above the flux obtained with ROSAT (Hünsch et al. 1999) and $\sim$50% below the values obtained with *Einstein* (Vaiana et al. 1981) in the respective energy bands.

4. Summary and discussion

Our analysis of EQ Peg is another example of how the high-resolution X-ray telescopes *Chandra* and XMM-Newton allow one to resolve sources down to a unprecedented spatial resolution (for other examples see Stelzer & Burwitz 2003 and Audard et al. 2003).

With the XMM-Newton observation of the EQ Peg system we were able to separate the two components for the first time in X-rays. Using a PSF model fit procedure we can reconstruct the source positions and show that both components are flaring X-ray emitters. On average, we found the A component brighter by a factor $\sim$3.5 for the total observation.

During this observation a series of medium flares was detected. We were able to determine count ratios for EQ Peg A/B

for the different phases of activity. During the early (quiescent) phase of the observation the emission is strongly dominated by EQ Peg A, which is a factor of $\sim$4$-$5 brighter than EQ Peg B. Comparison of the quiescent and active phases made it possible to associate most of the flaring with EQ Peg B, which nearly doubled it's X-ray brightness during the peak of the flare. The count ratio during the peak of the flare on EQ Peg B dropped to $\sim$2.5$-$3. We also found evidence for flaring activity on EQ Peg A towards the end of the observation, consistent with previous findings that both stars exhibit flaring behavior (e.g., Rodonò 1978). In fact, the relative brightening during the flares is much stronger for EQ Peg B, but the absolute increase in flux is comparable for both stars. The energy released by these flares is obviously very similar, although the quiescent emission level is quite different. The flaring X-ray emission of the EQ Peg system shows the typical hardening in the spectral energy distribution as expected for stellar flares.

References

Audard, M., Güdel, M., & Skinner, S. L. 2003, ApJ, 589, 983
Bopp, B. W. 1974, MNRAS, 168, 255
Ehle, M., Breitfellner, M., Gonzales Riestra, M., et al. 2003, XMM-Newton User's Handbook
Elvis, M., Plummer, D., Schachter J., et al. 1992, ApJS, 80, 257
Gagné, M., Valenti, J., Johns-Krull, C., et al. 1998, ASP Conf. Ser., 154, 1484
Ghizzardi, S. 2001, EPIC-MCT-TN-011
Hünsch, M., Schmitt, J. H. M. M., Sterzik, M. F., et al. 1999, A&AS, 135, 319
Katsova, M. M., Livshits, M. A., & Schmitt, J. H. M. M. 2002, ASP Conf. Proc., 177, 515
Kirsch, M., & EPIC Consortium, XMM-SOC-CAL-TN-0018
Owen, F. N., Bopp, B. W., Moffett, T. J., & Lazor, F. J. 1972, ApL, 10, 37
Pallavicini, R., Kundu, M. R., & Jackson, P. D. 1986, Lecture Notes in Physics, 254, 225
Perryman, M. A. C., Lindegren, L., Kovalevsky, J., et al. 1997, A&A, 323, L49
Poletto, G., Pallavicini, R., & Kopp, R. A. 1988, A&A, 201, 93
Press, W. H., Teukolsky, S. A., Vetterling, W. T., et al. 1999, Numerical Recipes in C (Cambridge Univ. Press)
Rodonò, M. 1978, A&A, 66, 175
Roques, P. E. 1954, PASP, 66, 256
Schmitt, J. H. M. M., Fleming, T. A., & Giampapa, M. S. 1995, ApJ, 450, 392
Schmitt, J. H. M. M., & Liefke, C. 2003, A&A, in press
Stelzer, B., & Burwitz, V. 2003, A&A, 402, 719
Topka, K., & Marsh, K. A. 1982, ApJ, 254, 641
Vaiana, G. S., Cassinelli, J. P., Fabbiano, R., et al. 1981, ApJ, 244, 163

Chapter 4

X-rays from accretion shocks in T Tauri stars: The case of BP Tau

J. H. H. M. Schmitt, J. Robrade, J.-U. Ness, F. Favata and B. Stelzer

Astronomy
&
Astrophysics

Letter to the Editor

X-rays from accretion shocks in T Tauri stars: The case of BP Tau

J. H. M. M. Schmitt[1], J. Robrade[1], J.-U. Ness[2], F. Favata[3], and B. Stelzer[4]

[1] Hamburger Sternwarte, Gojenbergsweg 112, 21029 Hamburg, Germany
   e-mail: jschmitt@hs.uni-hamburg.de
[2] University of Oxford, Department of Theoretical Physics, 1 Keble Road, Oxford OX1 3NP, UK
[3] Astrophysics Division, ESA/ESTEC, PO Box 299, 2200 AG, Noordwijk, The Netherlands
[4] Dipartimento di Scienze Fisiche e Astronomiche, Università di Palermo, Piazza del Parlamento 1, 90134 Palermo, Italy

Abstract. We present an XMM-Newton observation of the classical T Tauri star BP Tau. In the XMM-Newton RGS spectrum the O VII triplet is clearly detected with a very weak forbidden line indicating high plasma densities and/or a high UV flux environment. At the same time concurrent UV data point to a small hot spot filling factor suggesting an accretion funnel shock as the site of the X-ray and UV emission. Together with the X-ray data on TW Hya these new observations suggest such funnels to be a general feature in classical T Tauri stars.

Key words. X-rays: stars – stars: individual: BP Tau – stars: pre-main sequence, coronae, activity – accretion

1. Introduction

One of the central results of stellar X-ray astronomy is the discovery that all "cool stars", i.e., stars with outer convective envelopes, are surrounded by hot coronae (Schmitt & Liefke 2004). The usual interpretation of this finding is that the combined action of turbulence in the outer convection zones and the ever-present rotation leads to dynamo action with vigorous production of magnetic fields and ensuing activity. X-ray observations support this interpretation with the "onset of activity", i.e., the rapid increase in X-ray detection rates of main sequence stars at spectral type $\approx$ F0 and the correlation between rotation rate and activity.

Strong X-ray emission is found also from many young stars such as zero age main sequence stars or T Tauri above the main sequence. Both flavors of T Tauri stars, i.e., the weak line T Tauri stars (wTTS) without disks as well as the classical T Tauri stars (cTTS) with disks are X-ray sources (Feigelson & Montmerle 1999). The presence of a disk around cTTS constitutes a fundamental difference compared to a "normal" star without disk, since the energy stored in the disk material can be released through accretion and lead to super-photospheric and/or time variable emissions; in fact, the optical variability observed in (some) cTTS (Gullbring et al. 1996) is commonly interpreted in this fashion. Yet the high-energy activity observed from cTTS and wTTS is usually interpreted as a "scaled-up" version of solar activity. The low-resolution X-ray data available prior to XMM-Newton and *Chandra* made a distinction between the X-ray properties of wTTS and cTTS very difficult; while some differences in emission level and variability properties between wTTS and cTTS were indicated by statistical studies (Stelzer et al. 2000; Stelzer & Neuhäuser 2001;

Flaccomio et al. 2003), a characterization of the physical properties of the X-ray emitting regions was impossible.

This situation has changed with the advent of high-resolution grating spectroscopy with XMM-Newton and *Chandra*. A great surprise was the X-ray spectrum of the cTTS TW Hya (Kastner et al. 2002; Stelzer & Schmitt 2004), which clearly showed low forbidden to intercombination (f/i) line ratios in the O VII and Ne IX triplets, which were interpreted as due to high plasma densities in the X-ray emitting regions. The extensive spectral survey by Ness et al. (2004), who studied high-resolution X-ray spectra of 48 coronal sources, provided no star that would even come close to the low O VII f/i-ratio as observed for TW Hya. Clearly, TW Hya differs in its coronal properties from all other stars, and it is very natural to ascribe this difference to the presence of an accretion disk around TW Hya. Specifically, Kastner et al. (2002) and Stelzer & Schmitt (2004) interpret the X-ray emission as arising from an accretion shock produced by matter falling down onto TW Hya along a magnetic funnel. There is an obvious need to examine further cTTS with high-resolution spectroscopy in order to assess whether TW Hya's X-ray properties are typical for cTTS or not. We therefore obtained a high-resolution X-ray spectrum of the cTTS BP Tau with the Reflection Grating Spectrometer (RGS) onboard XMM-Newton, and the purpose of this letter is to present and discuss the implications of this observation.

2. Observations

2.1. The cTTS BP Tau: Optical and X-ray properties

An extensive overview of the optical properties of BP Tau is given by Gullbring et al. (1996) and Errico et al. (2001).

Its spectral type varies from K5−K7, it rotates fast ($v \sin(i) =$ 15.4 km s^{-1}), but various rotation period measurements varying between 6.1 to 8.3 days have been published. The cTTS nature of BP Tau is clearly demonstrated by the excess continuum (veiling) and Balmer emission (Bertout et al. 1988). There is debate about BP Tau's distance, and Wichmann et al. (1998) argue against BP Tau being an outlier from the Taurus-Auriga cloud as suggested by its HIPPARCOS parallax. From extensive optical monitoring Gullbring et al. (1996) conclude that optical variability is common in BP Tau, but in character very much different from variability encountered in typical flare stars. Most of the observed changes are slow and smooth and are interpreted as the result of inhomogeneous accretion from the disk onto the stellar surface. This view is strongly supported by the circular polarization in the He I λ 5876 emission line measured by Johns-Krull et al. (1999), who deduce a mean longitudinal magnetic field of 2460 ± 120 G in the line forming region and argue that accretion occurs preferentially along large-scale magnetic loops with a small filling factor. X-ray emission from BP Tau at a level of $\approx 10^{30}$ erg/s was first reported by Walter & Kuhi (1981) using the *Einstein Observatory*. In a simultaneous optical and X-ray observations of BP Tau with ROSAT Gullbring et al. (1997) found no evidence for correlated variations between the two bands and thus attributed the X-ray emission to magnetically active regions.

2.2. XMM-Newton X-ray data

BP Tau was observed with XMM-Newton on August 15, 2004 for a duration of 131 ks (Obs-ID 0200370101) with the RGS as prime instrument. The observations were performed in full-frame mode employing the thick filter for both the MOS and the PN cameras of the European Photon Imaging Camera (EPIC). The optical monitor (OM) was operated using the UVW1 filter with a band pass between 2500 Å and 3500 Å and an effective wavelength of 2910 Å according to the XMM-Newton users' handbook (Ehle et al. 2004). All XMM-Newton data was analyzed with SAS version 6.0. Background conditions were very quiet throughout most of the BP Tau observation and only 10 ks of data had to be screened. In Fig. 1 we show the EPIC PN X-ray light curve, the X-ray hardness ratio (lower panel), and the UVW1 light curve (upper panel). An obvious X-ray flare with a spectral hardness increase occurred between $\approx 20-40$ ks into the observations; the X-ray flare may be accompanied by a much longer lasting UV event, but there is no strict correlation between X-ray and UV variability.

In Fig. 2 we show the EPIC PN spectrum of BP Tau (lower curve) in comparison to TW Hya (upper curve; cf. Stelzer & Schmitt 2004). Above ≈ 2.5 keV the two spectra overlap, while at lower energies the flux of TW Hya exceeds that of BP Tau by almost an order of magnitude. Spectral modeling of the EPIC PN spectrum using simple multi-temperature fits requires absorption column densities of $1-2 \times 10^{21}$ cm^{-2} depending on the chosen model and consistent with the relation between N_H and E_{B-V} (Jenkins & Savage 1974); hot temperatures (≈ 2 keV) are required in contrast to TW Hya, whose EPIC spectrum is dominated by cool plasma of ≈ 0.3 keV
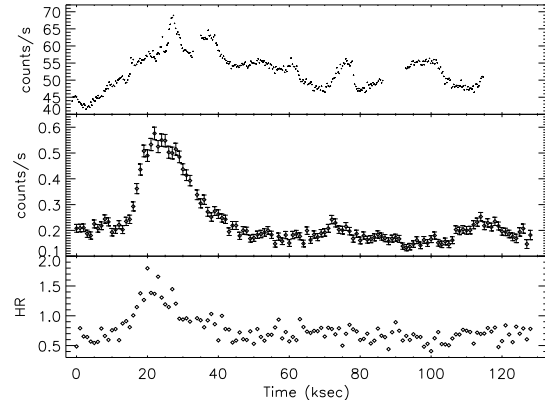
Fig. 1. OM UVW1 light curve (*upper panel*; bin size 300 s), EPIC PN X-ray light curve (*medium panel*), and X-ray hardness ratio defined as ratio between the rates in the bands 0.2−1.0 and 1.0−10.0 keV (*lower panel*; both with bin size 1000 s).
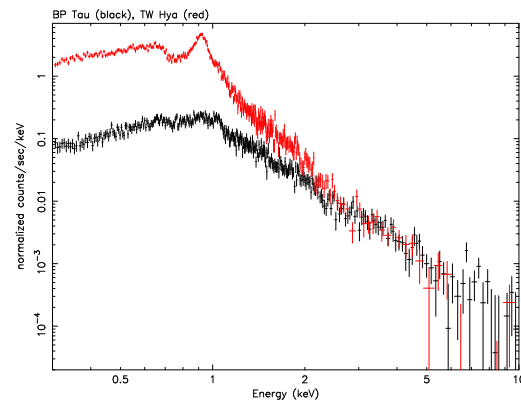
Fig. 2. EPIC PN spectrum of BP Tau (quiescent phase; lower black points) in comparison to the EPIC PN spectrum of TW Hya (upper, red/grey points).

(cf., Stelzer & Schmitt 2004). Thus the EPIC spectra of BP Tau and TW Hya suggest differences between the two stars.

However, BP Tau's instrumental background-subtracted high resolution RGS2 spectrum looks rather similar to that of TW Hya, (cf., Fig. 3); probing the lower-energy plasma it shows mostly oxygen and neon lines with – at best – weak iron lines as well as signs of a continuum. Because of the low signal only a few spectral lines can be reliably detected in our RGS spectra. The clearly detected lines include the O VIII Ly$_\alpha$ line, the O VII triplet, the Ne X Ly$_\alpha$ line, and the Ne IX triplet at 13.5 Å; interestingly, no unambiguous RGS detections of iron lines, in particular at 15.03 Å and 17.07 Å were obtained (cf., Fig. 3 and Table 1), reminiscent of the low amount of iron derived for TW Hya. Also, no lines of nitrogen and carbon could be detected, presumably because of the larger absorption column towards BP Tau. The detected lines together with the derived best fit line counts and their errors are listed in Table 1; all line counts were derived with the CORA program
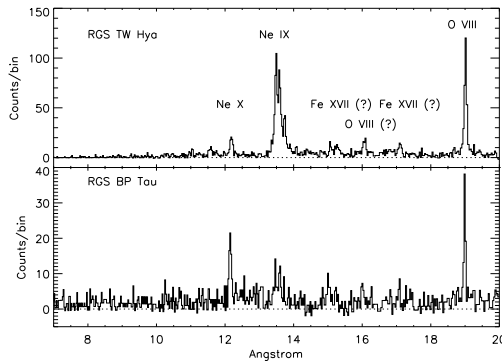
Fig. 3. Comparison of instrumental background subtracted RGS2 spectra of TW Hya and BP Tau with line identifications.

Fig. 4. RGS spectrum BP Tau: O VII triplet region with best fit model.

Table 1. X-ray lines detected in the RGS spectrum of BP Tau, line counts and photon fluxes in units of 10^{-6} ph s^{-1} cm^{-2}.

Line ID	λ (Å)	Counts	Error	Instr.	Flux
Ne X Ly$_\alpha$	12.14	91.5	11.7	RGS2	13.2
Ne IX He r	13.46	37.0	9.9	RGS2	5.2
Ne IX He i	13.56	31.2	9.8	RGS2	4.4
Ne IX He f	13.71	12.5	7.1	RGS2	1.7
O VIII Ly$_\beta$	16.03	25.8	6.4	RGS1	4.1
O VIII Ly$_\beta$	16.00	16.7	6.2	RGS2	2.3
O VIII Ly$_\alpha$	18.97	95.5	11.4	RGS2	14.2
O VII He r	21.6	47.7	8.6	RGS1	8.9
O VII He i	21.8	36.6	7.8	RGS1	7.1
O VII He f	22.1	13.7	5.5	RGS1	2.7
Fe XVII	15.03	<20		RGS1	<2.9

Table 2. Line counts measured in "low state" and in "high state" and extrapolated "high state" counts.

Line	Low state	High state	"Low state"/3.2
Ne X Ly$_\alpha$	48.6 ± 8.7	42.7 ± 8.0	15.2 ± 2.7
O VIII Ly$_\alpha$	59.2 ± 9.1	32.5 ± 6.6	18.5 ± 2.8
O VII He r	34.4 ± 7.3	10.7 ± 4.1	10.8 ± 2.3
O VII He i	24.6 ± 6.3	9.5 ± 4.2	7.7 ± 2.0
O VII He f	5.5 ± 3.8	5.6 ± 3.2	1.7 ± 1.2

(Ness & Wichmann 2002), assuming Lorentzian line shapes. The line fits were carried out in such a way that the wavelength differences between the triplet lines and line widths were held constant; the background was adjusted by eye, different choices of background lead to line flux variations well within the errors; in Fig. 4 we plot the RGS spectrum around the O VII triplet at 22 Å together with our best fit model. From the numbers listed in Table 1 we find an observed f/i-ratio of 0.37 ± 0.16 for O VII and 0.40 ± 0.26 for Ne IX; the latter assumes negligible contamination by iron, which is a severe problem for the interpretation of any Ne IX triplet data (cf., Ness et al. 2003) depending on the strength of the iron lines.

3. Discussion

Stelzer & Schmitt (2004) interpret the XMM-Newton X-ray data on the cTTS TW Hya in terms of an accretion funnel scenario, where the X-ray emission is emitted in a shock ("hot spot") produced by the infall of material along the magnetic field at essentially free-fall velocity onto the stellar surface. Does the same scenario also apply to the cTTS BP Tau and possibly to cTTS as a class?

It is instructive to compare the observed line fluxes from BP Tau with those measured from TW Hya (cf., Table 2

in Stelzer & Schmitt 2004), taking into account the different amounts of interstellar absorption. For ISM columns of 3×10^{20} cm^{-2} and 1×10^{21} cm^{-2} respectively, we compute ISM transmissivities of (0.83, 0.54) at 18.97 Å, (0.77, 0.42) at 21.6 Å, (0.93, 0.78) at 12.14 Å, and (0.91, 0.73) at 13.46 Å for TW Hya and BP Tau respectively. These values lead to ratios between the Ly$_\alpha$ and He-like r flux ratios 1.9 and 2.1 for oxygen and 0.3 and 2.7 for neon respectively. While the ratios for oxygen are about similar, those for neon differ quite significantly, thus the emission measure distribution in BP Tau must also be different. We also note that the Ly$_\alpha$ and He-like r flux ratios observed in BP Tau for oxygen and neon are not consistent with a single temperature.

We next checked to what extent individual RGS-detected lines are influenced by the flare. We defined a "high state" by including all data recorded in the time interval 13.5−43.0 ks (counted from the start of the observations as in Fig. 1) and a "low state" including all the rest and determined line counts as before. We also computed the expected number of "high state" counts extrapolating from the "low state" values and list all results in Table 2. Clearly, within the errors the O VII line counts are unaffected by the flaring emission, and only 15% of the recorded O VIII line counts can be attributed to the flare; for Ne X this contribution rises to 30%. We thus conclude that the observed O VII emissions are not significantly affected by the flare, while O VIII Ly$_\alpha$ is contaminated by <20%.

In addition to the X-ray data concurrent photometric UV data from the XMM-Newton OM are available for BP Tau (cf., Fig. 1). The UV continuum flux of BP Tau is thought to be produced by an accretion hot spot as demonstrated by

Ardila & Basri (2000) and Errico et al. (2001). The same applies of course also to our OM UVW1 photometric data, which would require filling factors of ten or more stellar surfaces if they were to be reconciled with BP Tau's photospheric temperature. We therefore assume in the following that the recorded UVW1 flux is exclusively produced in a hot spot and deredden this UV-flux using $A_V = 0.51$ (Gullbring et al. 1998) and $E_{B-V} = 0.32 \times A_V$. Without any further spectral information we assume an emergent blackbody spectrum with variable temperature T_{em}, convert count rate into specific energy flux (erg/cm^2/s/Å) using the instrumental conversion factor of 4.4×10^{-16} (erg/cm^2/count/Å), and compute the fractional surface area and filling factor required to account for the (dereddened) observed UVW1 flux. Assuming hot spot temperatures between $8000-10\,000$ K (cf., Calvet & Gullbring 1998; Ardila & Basri 2000), we invariably find filling factors between $0.6-4\%$, which are in line with values computed from more sophisticated models including shocks and an irradiated photosphere (Calvet & Gullbring 1998).

Converting the observed oxygen f/i-ratio of 0.37 ± 0.16 to density yields a nominal value of $\log n_e = 11.48$ with a (formal) error range of $(11.3-11.8)$, neglecting radiative deexcitation of the forbidden line level; therefore the derived densities may be regarded as upper limits if the X-ray emitting region is affected by the observed UV radiation. We re-emphasize that both BP Tau and TW Hya have lower f/i-ratios and higher densities than all of the coronal X-ray sources analyzed by Ness et al. (2004). If the O VII f/i-ratio was contaminated by a lower density "coronal component", any accretion-related shock component would require an even smaller f/ir-ratio.

Assuming optically thin emission, the observed energy flux in the O VII and O VIII lines, f_{oxy}, is given by $f_{oxy} = A_{sh} z n_e^2 P_{oxy}/4\pi d^2$, where A_{sh}, z, n_e, P_{oxy} denote shock area, cooling zone thickness, electron density and line cooling function respectively. The post shock plasma cooling time τ is given by $\tau = 3 n_e kT/n_e^2 P_{tot}$, with k, T and P_{tot} denoting Boltzmann's constant, temperature and overall radiative loss function. Postshock velocity V_{post}, z and τ are related through $\tau = z/V_{post}$. Thus we calculate the mass accretion rate $M_{acc} = \frac{4\pi d^2 f_{oxy} m_H \mu P_{tot}}{3kT P_{oxy}}$, with m_H denoting hydrogen mass and μ the mean molecular weight. With the observed values for f_{oxy} we find with $T = 2.5$ MK $M_{acc} \approx 9 \times 10^{-10}$ $M_\odot$/yr, about an order of magnitude smaller than inferred at UV wavelengths; since the observed oxygen fluxes may contain non-accretion related contributions, this value of M_{acc} should be considered as an upper limit. Filling factors of a few percent yield densities consistent with the O VII triplet and a cooling zone thickness of ≈ 100 km. As to the depth of the X-ray emitting region, a model independent absorption estimate using the observed photon flux ratio in the Ly$_\alpha$ and Ly$_\beta$ lines of 3.1 (cf., Table 1) requires with temperature of $\log T = 6.8$ an equivalent absorption column of $\approx 5 \times 10^{21}$ cm^{-2}. Given the large errors on the Ly$_\beta$/Ly$_\alpha$ photon flux ratio and the internal consistency between RGS2 values and optical extinction and the N_H values of $N_H \approx 2 \times 10^{21}$ cm^{-2} derived from the broad band X-ray spectra, we conclude that there is no real evidence for an "additional" absorption of BP Tau's X-ray flux.

4. Conclusions

The XMM-Newton RGS spectrum clearly demonstrates that X-ray emitting O VII layers in the cTTS BP Tau are either at high density and/or immersed in a strong ultraviolet flux. Both possibilities can be well explained by an X-ray emitting accretion shock on BP Tau. This accretion shock can, however, produce only the low-temperature components in the broad band X-ray spectra of BP Tau (and TW Hya); to explain the high temperature component additional processes possibly involving magnetic interactions between the disk and the star or magnetic activity anchored in the photosphere are required. Also, the derived mass accretion rates are smaller than those inferred from optical and UV data, but a detailed modeling in particular taking into account non-equilibrium effects is still lacking. At any rate, the XMM-Newton observations of BP Tau show that TW Hya is not "alone". Accretion shocks at the end of magnetic funnels connecting disk and stellar surface may in fact be a common feature of cTTS stars as a class.

References

Ardila, D. R., & Basri, G. S. 2000, ApJ, 539, 834
Bertout, C., Basri, G. S., & Bouvier, J. 1998, ApJ, 330, 350
Calvet, N., & Gullbring, E. 1998, ApJ, 509, 802
Ehle, M., Breitfellner, M., Gonzales Riestra, M., et al. 2004, XMM-Newton User's Handbook
Errico, L., Lamzin, S. A., & Vittone, A. A. 2001, A&A, 377, 557
Gullbring, E., Barwig, H., Chen, P. S., Gahm, G. F., & Bao, M. X. 1996, A&A, 307, 791
Gullbring, E., Barwig, H., & Schmitt, J. H. M. M. 1997, A&A, 324, 155
Gullbring, E., Hartmann, L., Briceño, C., & Calvet, N. 1998, ApJ, 492, 392
Feigelson, E. D., & Montmerle, T. 1999, ARA&A, 37, 363
Flaccomio, E., Micela, G., & Sciortino, S. 2003, A&A, 402, 277
Jenkins, E. B., & Savage, B. D. 1974, ApJ, 187, 243
Johns-Krull, C. M., Valenti, J. A., Hatzes, A. P., & Kanaan, A. 1999, ApJ, 510, L41
Kastner, J. H., Huenemoerder, D. P., Schulz, N. S., & Canizares, C. R. 2002, ApJ, 567, 434
Ness, J.-U., & Wichmann, R. 2002, AN, 323, 129
Ness, J.-U., Brickhouse, N. S., Drake, J. J., & Huenemoerder, D. P. 2003, ApJ, 598, 1277
Ness, J.-U., Güdel, M., Schmitt, J. H. M. M., et al. 2004, A&A, 427, 667
Schmitt, J. H. M. M., & Liefke, C. 2004, A&A, 417, 651
Stelzer, B., Neuhäuser, R., & Hambaryan, V. 2000, A&A, 356, 949
Stelzer, B., & Neuhäuser, R. 2001, A&A, 377, 538
Stelzer, B., & Schmitt, J. H. M. M. 2004, A&A, 418, 687
Walter, F. M., & Kuhi, L. V. 1981, ApJ, 284, 194
Wichmann, R., Bastian, U., Krautter, J., Jankovics, I., & Rucinski, S. M. 1998, MNRAS, 301, L39

Chapter 5

XMM-Newton X-ray spectroscopy of classical T Tauri stars

J. Robrade and J. H. H. M. Schmitt

XMM-Newton X-ray spectroscopy of classical T Tauri stars

J. Robrade and J.H.M.M. Schmitt

Hamburger Sternwarte, Universität Hamburg, Gojenbergsweg 112, D-21029 Hamburg, Germany

Abstract.
We present results from a comparative study of XMM-Newton observations of four classical T Tauri stars (CTTS), namely BP Tau, CR Cha, SU Aur and TW Hya. In these objects coronal, i.e. magnetic, activity and as recently shown, magnetically funneled accretion are the processes likely to be responsible for the generation of X-ray emission. Variable X-ray emission with luminosities in the order of 10^{30} erg/s is observed for all targets. We investigate light curves as well as medium and high-resolution X-ray spectra to determine the plasma properties of the sample CTTS and to study the origin of their X-ray emission and its variability. The emission measure distributions and observed temperatures differ significantly and the targets are dominated either by plasma at high densities as produced by accretion shocks or by predominantly hotter plasma of coronal origin. Likewise the variability of the X-ray luminosity is found to be generated by both mechanisms. Cool plasma at high densities is found in all stars with detected O VII triplet emission, prevented only for SU Aur due to strong absorption. A general trend is present in the abundance pattern, with neon being at solar value or enhanced while oxygen, iron and most other metals are depleted, pointing to the presence of the inverse FIP effect in active coronae and possibly grain formation in evolved disks. We find that both accretion shocks and coronal activity contribute to the observed X-ray emission of the targets. While coronal activity is the dominant source of X-ray activity in the majority of the CTTS, the fraction for each process differs significantly between the individual objects.

Key words. Stars: activity – Stars: coronae – Stars: late-type – Stars: pre-main sequence – X-rays: stars

1. Introduction

Young, late-type pre main-sequence stars, known as T Tauri stars, are copiously found in or near star forming regions. Historically, they are classified according to their Hα equivalent width as classical T Tauri stars (CTTS) with EW>10Å or otherwise as weak line T Tauri stars (WTTS). The principal physical difference between these two classes is that CTTS are thought to be in an earlier evolutionary stage, i.e. they still possess a disk containing dust and gas and are accreting matter. WTTS are thought to be more evolved, to have mainly lost their disks and are approaching the main-sequence. While CTTS are generally younger with ages of a few up to ~ 10 Myr and the overall fraction of CTTS in a given star-forming region decreases with age, both types of T Tauri stars are commonly found in the same star-forming regions, indicating individual evolutionary time scales. Since the Hα line is often time-variable, a classification solely based on its strength is sometimes misleading and other or additional spectral features have been used to identify and classify CTTS more reliably. The existence of a disk containing a significant amount of matter and ongoing accre-

Send offprint requests to: J. Robrade
Correspondence to: jrobrade@hs.uni-hamburg.de

tion onto the host star impose major differences between the two types of TTS, leading to different spectral properties which can be observed at different wavelengths. The effects of the warm and probably structured disk are for instance reflected in the different infrared designations of CTTS (Class II) and WTTS (Class III) due to their additional near-infrared emission, which is an important indicator for CTTS. Consequently, the different criteria and underlying data used for the identification of CTTS may introduce selection effect in the respective samples.

Both types of T Tauri stars are well known strong and variable X-ray emitters and large numbers of these objects were detected with *Einstein* (Feigelson & DeCampli, 1981; Feigelson & Kriss, 1989) and ROSAT (Feigelson et al., 1993; Neuhäuser et al., 1995). Their X-ray emission and the observed flaring was usually interpreted as a scaled-up version of coronal activity in analogy to cool main-sequence stars. This picture is still valid and the X-ray emission from WTTS is thought to originate from coronal activity. However, T Tauri stars are thought to be at least in their early stages fully convective, therefore the question arises about the underlying processes for the generation of the magnetic field and the influence of accretion on the stellar structure and corona. Further on, the evolutionary stages of young stars and their high energy emission

is of major importance for the process of planetary formation via its effects on chemistry, dust and protoplanets. A comprehensive review of high energy processes and underlying physics in young stellar objects, summarising the results of the era prior to *Chandra* and XMM-Newton, is presented by Feigelson & Montmerle (1999).

The largest sample of pre main-sequence stars are found in the Orion Nebula Cloud. Using *Chandra* ACIS observations, Feigelson et al. (2003) analysed a sample of 500 PMS stars with known basic properties. An even deeper exposure, named the *Chandra* Orion Ultradeep Project (COUP) was presented recently, see e.g. Preibisch et al. (2005), confirming and extending their results. The X-ray luminosity of CTTS in this sample was found to be correlated with bolometric luminosity. No strong correlation between L_X and rotation as observed for main-sequence stars was found, contrary, L_X correlates with L_{bol} and stellar mass, indicating the presence of different, e.g. turbulent, dynamos or of supersaturation effects in solar-type dynamos. The question, whether the presence of an accretion disk influences the stellar X-ray emission is still under debate. While Feigelson et al. (2003) found no intrinsic differences of X-ray activity related to the presence of a circumstellar disk, the results found by Preibisch et al. (2005) indicate that accretion diminishes L_X on average and weaken the L_X/L_{bol} correlation. A similar influence was found by Stelzer & Neuhäuser (2001) in the X-ray properties of young stars in the Taurus-Auriga complex observed with ROSAT PSPC. The COUP sources are rather consistent with the bulk of their X-ray emission being produced in typical coronae. In general, magnetic activity in CTTS may also involve the circumstellar material, e.g. via star-disk interaction, but the topology of their magnetic fields in virtually unknown; Favata et al. (2005) present evidence for magnetic star-disk interaction in the analysis of larger flares on several COUP objects.

Moreover, recent high-resolution spectroscopy of CTTS with *Chandra* and XMM-Newton, indicated accretion shocks at least as an additional mechanism for the generation of X-ray emission in CTTS. In this interpretation X-ray emission is generated by a magnetically funneled accretion stream falling onto small areas of the stellar surface, producing shocked high density plasma (Shu et al., 1994; Calvet & Gullbring, 1998). Since in magnetospheric accretion the matter falls from several stellar radii at nearly free-fall velocity, strong shocks and consequently hot plasma emitting in the X-ray regime are formed. This contribution is expected to be at energies below 0.5 keV and is distinguishable from cool coronal plasma by its density; therefore it can be recognised only through high resolution X-ray spectroscopy. It is thus not contradictory that the COUP sample based on ACIS data with medium resolution spectroscopy and poorer sensitivity at low energies finds accretion to play no significant role.

TW Hya was the first example of a CTTS, where observational evidence for an accretion scenario could be found in X-ray data. Analysis using density sensitive lines of He-like triplets (e.g. O VII, Ne IX) indicated very high densities, exceeding by far the densities previously found in coronal plasma from any other star (Kastner et al., 2002; Stelzer & Schmitt, 2004). These low line ratios were also found in the spectra of BP Tau (Schmitt et al., 2005), again strongly supporting an accretion scenario. However, accretion is only capable to produce plasma with temperatures of a few MK and therefore contributes nearly exclusively to the low energy X-ray emission. The observed flaring and additional hard emission attributed to plasma with temperatures of several tens of MK in BP Tau and other CTTS require the presence of an additional X-ray generating mechanism such as magnetic activity. In this work we use the term 'coronal activity', but more complex phenomena like star-disk interactions cannot be ruled out. While TW Hya like objects where accretion is thought to be the dominant source of the X-ray emission are probably rare, the BP Tau observation revealed that accretion as an additional X-ray generating mechanism may be more common. Another X-ray generating mechanism, shocks in strong Herbig-Haro outflows that may also produce a soft X-ray excess, was proposed for jet-driving CTTS (which resemble Class I protostars) like DG Tau (Güdel et al., 2005). We note that this model cannot explain the soft excess in the case of TW Hya or the other sample CTTS.

We utilise XMM-Newton data from four X-ray bright CTTS to study the origin of their X-ray emission in accretion shocks vs. coronal activity. We specifically use medium and high resolution X-ray spectra and spectrally resolved X-ray light curves to investigate the physical properties of our target stars BP Tau, CR Cha, SU Aur and TW Hya and to check the relevance of these mechanisms for the generation of the X-ray emission and variability in these young stars. This work is the first comparative X-ray study of CTTS using high and medium resolution spectra so far, therefore it is complementary to large sample studies of a specific star forming region such as COUP. Moreover, the data of CR Cha and partly of SU Aur and BP Tau is analyzed and presented here for the first time. Results derived from RGS spectra of BP Tau and the simultaneous obtained UV data were presented in our previous letter (Schmitt et al., 2005), while the data on TW Hya first presented by Stelzer & Schmitt (2004) is re-analysed for purposes of comparison in a manner identical to the analysis of all other sources. The plan of our paper is as follows: In Sect. 2 we describe the individual targets and previous X-ray results, in Sect. 3 the observations and the methods used for data analysis and in Sect. 4 we present and discuss the results subdivided into different physical topics, followed by a summary and our conclusions in Sect. 5.

2. The CTTS sample

BP Tau is a CTTS with spectral type K5–K7 associated with the Taurus-Auriga star forming region at a distance of 140 pc as discussed by Wichmann et al. (1998). Optical and infrared measurements clearly show the typical characteristics of excess emission produced by accre-

tion (Gullbring et al., 1998). BP Tau has a moderate inclination angle of roughly 30° and its disk was found to be quite compact (Muzerolle et al., 2003). X-ray emission from BP Tau with $L_X \sim 10^{30}$ erg/s was already measured with the *Einstein Observatory* (Walter & Kuhi, 1981), the RASS luminosity was determined as 0.7×10^{30} erg/s (Neuhäuser et al., 1995). Gullbring et al. (1997) presented an analysis of simultaneous optical and ROSAT observations of BP Tau. Finding no correlation between optical and X-ray variability they concluded that the optical emission is attributed to accretion while the X-ray emission arises from magnetically active regions. Initial results of our XMM-Newton observation of BP Tau with special focus on the RGS data and density diagnostics with the He-like triplet of O VII were presented in our previous letter (Schmitt et al., 2005), where evidence for high density plasma and/or intense UV radiation is presented, supporting the presence of an accretion funnel in BP Tau and a rough estimate of BP Tau's mass accretion rate as derived from simultaneous UV measurements was given.

CR Cha with spectral type K2 is located in the Chamaeleon I cloud, a star forming region at a distance of 140–150 pc with a measured RASS luminosity of 1.5×10^{30} erg/s (Feigelson et al., 1993). It was classified as CTTS via Hα, see e.g. Reipurth et al. (1996), and according to Meeus et al. (2003) it is dominated by small amorphous silicates, indicating large amounts of unprocessed dust. The archival XMM-Newton data of CR Cha is analysed and presented here for the first time.

SU Aur is classified as G2 subgiant and also a member of the Taurus-Auriga star forming region, therefore we adopt a distance of 140 pc. For this very luminous and variable object also a wider range of values of its optical properties is given in literature, see e.g. DeWarf et al. (2003). It was sometimes classified as WTTS, but a clear IR-excess confirms its status as a CTTS, viewed nearly edge on, with a rather high accretion luminosity (Muzerolle et al., 2003), thus causing the strongest absorption signatures in our sample. SU Aur is one of the brightest known CTTS, its strong X-ray emission was already detected with the *Einstein Observatory* (Feigelson & DeCampli, 1981) with an X-ray luminosity of 3.0×10^{30} erg/s. A similar value (3.7×10^{30} erg/s) was derived from RASS data by Neuhäuser et al. (1995), making it the brightest target in our sample, especially when considering the unabsorbed X-ray luminosity. Some results of the XMM-Newton observation are presented in an analysis of star forming regions by Pallavicini et al. (2004), who showed that SU Aur is both extremely hot and variable.

TW Hya is classified as a K7–K8 star and is the nearest object in our sample. At a distance of only 56 pc it is located in the TW Hydra association, a nearby young but diffuse stellar associations, see e.g. Zuckerman et al. (2001). TW Hya is viewed nearly pole on and due to its proximity and lack of obscuring clouds it can well studied at all wavelengths. With an estimated age of nearly

10 Myr it is also one of the oldest known stars, still accreting matter. Kastner et al. (1999) analysed ASCA and ROSAT data of TW Hya and found that a model with plasma temperatures of ~ 1.7 and ~ 9.7 MK and an X-ray luminosity of $\sim 2 \times 10^{30}$ erg/s describes both observations well. TW Hya was also observed with the *Chandra* HETGS detector (Kastner et al., 2002), providing high resolution spectra, which were modelled with an iron depleted and neon enhanced plasma and a emission measure distribution showing a sharp peak around 3 MK. The analysis of density sensitive lines indicated plasma at high densities (log n_e=13) and the inferred plasma properties were found to be consistent with the X-ray emission to be generated by funneled mass accretion from the circumstellar disk. Several moderate 'flares' were detected on TW Hya during the ASCA and *Chandra* observation; however, the untypical shape of the flare light curve and the seemingly constant spectral properties led Kastner et al. (2002) to conclude that most or all of the X-ray emission of TW Hya originates from accretion. Results of the XMM-Newton observation of TW Hya obtained with a somewhat different analysis were presented by Stelzer & Schmitt (2004), who found that the XMM-Newton data can be well explained by X-ray emission from a metal depleted accretion shock with an X-ray luminosity of $\sim 1.5 \times 10^{30}$ erg/s, consistent with the *Chandra* results. Different conclusions were derived at on the interdependent properties mass accretion rate and surface area of the shock region, which is assumed to fill either below one percent or up to a few percent of the stellar surface. Here the TW Hya data is independently re-analysed to ensure consistency and allow a comparison of our results.

Table 1. Basic properties for our sample CTTS. Spectral types taken from Simbad database, distances adopted from Wichmann et al. (1998), ages from Gullbring et al. (1998): BP Tau, Natta et al. (2000): CR Cha, DeWarf et al. (2003): SU Aur, Makarov & Fabricius (2001): TW Hya, L_x are ROSAT values (< 2.4 keV).

Target	Spec.T.	Dist.(pc)	Age (yr)	$L_x(10^{30}\,erg\,s^{-1})$
BP Tau	K5V	140	6×10^5	0.7
CR Cha	K2	145	1×10^6	1.5
SU Aur	G2III	140	4×10^6	3.7
TW Hya	K8V	56	8×10^6	2.0

3. Observation and data analysis

All sample CTTS were observed with XMM-Newton using somewhat different detector setups with exposure times in the range of $30 - 130$ ks. Data were taken with all X-ray detectors, which were operated simultaneously onboard XMM-Newton, respectively the EPIC (European Photon Imaging Camera), consisting of the MOS and PN detectors and the RGS (Reflection Grating Spectrometer). Note that for SU Aur no PN data is available and different filters were used, the thick filter for the BP Tau and SU Aur

and the medium filter for the CR Cha and TW Hya observations. Further on, the signal to noise ratio differs for the various targets and instruments. For CR Cha only a fraction of the original data from the additionally split observation could be used for analysis because of very high background contamination; the RGS data from two exposures was merged with the tool 'rgscombine' provided with SAS 6.5, but the RGS spectrum of CR Cha is still underexposed. The EPIC data is quality is sufficient for all targets. In addition, strong absorption affects the data quality especially at lower energies. The details of our observations and used data are described in Table 2, a detailed description of the XMM-Newton instruments can be found in Ehle et al. (2003).

Table 2. Observation log of our sample CTTS, duration of prime instrument/RGS(filtered).

Target	Obs.Mode	Obs. Time	Dur. (ks)
BP Tau	FF/thick	2004-08-15T06:14–16T18:51	132/124
CR Cha	FF,LW/med.	2001-02-24T05:04–15:49	39/72
SU Aur	FF/thick	2001-09-21T01:27–22T14:18	130/126
TW Hya	FF/med.	2001-07-09T05:51–14:01	30/28

Data analysis was performed with the XMM-Newton Science Analysis System (SAS) software, version 6.0. Images, light curves and spectra were produced with standard SAS tools and standard selection criteria were applied for filtering the data, see Loiseau et al. (2004). X-ray spectral analysis was carried out with XSPEC V11.3 (Arnaud, 1996), while for line fitting purposes we used the CORA program (Ness & Wichmann, 2002), assuming Lorentzian line shapes. Individual line fits are used to investigate the density sensitive forbidden and intercombination lines of He-like triplets. Line counts are derived keeping the line spacing fixed within a triplet and using an overall line width for all lines. Spectral analysis of EPIC data is performed in the energy band between $0.3 - 10.0$ keV, while the RGS first order spectra in the full energy range, i.e. $0.35 - 2.5$ keV ($5 - 35$ Å), are used whenever data quality permits. While the RGS obviously has the highest spectral resolution, the EPIC detectors are more sensitive and are able to measure higher energy X-rays; the MOS detectors provide a slightly better spectral and spatial resolution, the PN detector is more sensitive. We emphasize that the data were analysed simultaneously but not co-added, thus providing sufficient signal for all observations and ensuring a consistent analysis for all targets. All periods affected by proton flares were removed from spectral analysis and for TW Hya the PN data was cleaned for some moderate pile-up. The background was taken from source free regions on the detectors.

For the analysis of the X-ray spectra we use multi-temperature models with variable but tied abundances, i.e. the abundance pattern was assumed to be the same in all temperature components. Such models assume the emission spectrum of a collisionally-ionized optically-thin gas as calculated with the APEC code, see e.g. Smith et al.

(2001). Since the RGS is not very sensitive above 2.0 keV, we use EPIC data to determine the properties of plasma with temperatures above 20 MK. In order to account for calibration uncertainties of the different detectors, see e.g. Kirsch et al. (2004), the normalization between instruments was taken as a free parameter for each type of instrument, i.e. for MOS, PN, RGS. Our fit procedure is based on χ^2 minimization, therefore spectra are always rebinned to satisfy the statistical demand of a minimum value of 15 counts per spectral bin. All errors are statistical errors given by their 90% confidence range and were calculated separately for abundances and temperatures by allowing variations of normalizations and respective model parameters. Note that additional uncertainties arise from uncertainties in the atomic data and instrumental calibration which are not explicitly accounted for.

The applied models use three temperature components, models with additional temperature components were checked, but did not improve the fit results significantly. Since the APEC models do not account for high density plasma, resolved density sensitive lines are excluded from the global fits for TW Hya. Abundances are calculated relative to solar photospheric values as given by Anders & Grevesse (1989). For iron and oxygen we use the updated values of Grevesse & Sauval (1998). Application of the new but controversial solar abundances published by Asplund (2005) would further increase the neon abundance in our sample stars compared to other metals, but not change our conclusions significantly. We note that relative results between the CTTS are not affected by the underlying solar abundance pattern. For elements with overall low abundances and no significant features in the X-ray spectra, i.e. Al, Ca, Ni, the abundances were tied to the iron abundance. When data quality permits, we determine the abundances of individual elements, global abundances are used if no features are present in the spectra. This is for instance the case for targets with strong absorption, where e.g. the stronger carbon lines at the low energy end of the detectors are completely absorbed. We simultaneously modelled the temperatures and emission measures (EM=$\int n_e n_H dV$) of the components and checked the derived results for consistency. X-ray luminosities were then calculated from the resulting best fit models.

Absorption in the circumstellar environment and possibly also in the interstellar medium is significant for CTTS and is applied in our modelling. Since absorption is supposed to be slightly variable and, in addition, optical and IR measurements often give a wider range of values, it is kept as a free parameter in our analysis. In general, the derived fit results are quite stable, but note that some of the fit parameters are mutually dependent, thus affecting especially absolute values. Interdependence mainly affects the low energy region of the spectra, where the strength of absorption, the emission measure and abundances of elements with emission lines in the respective temperature range strongly depend on each other. While some effects can be prevented by the methods described above, models with different absolute values of the mentioned parameters

but only marginal differences in its statistical quality may be fitted to the data, however ratios and relative changes of these properties are again very robust.

4. Results

4.1. X-ray light curves

To study time variability and its origin we first investigated the X-ray light curves of our sample CTTS. In Fig.1 we show background subtracted light curves with a temporal binning of 1000 s, extracted from a 50″ radius circular region around each source and cleaned for obvious data dropouts.

A flare with a rise in count rate of factor $2.5 - 3$ occurred during the BP Tau observation and a smaller flare (factor ~ 1.5) during the CR Cha observation. In the SU Aur data several flares were detected, the largest one showing an increase in X-ray brightness by a factor of 3. TW Hya does not exhibit a flare during the XMM-Newton observation, any variability remains in the range of only 10%. However, light curve variations with factors around two are also known for TW Hya (Kastner et al., 1999, 2002), who noted three 'flares' during 140 ks (ASCA, 94 ks + Chandra, 48 ks) observation time but no spectral changes were detected during the periods of increased X-ray brightness. The average time scale for flares on CTTS appears to be around one moderate flare (factor $\gtrsim 2$) occurring daily on our sample CTTS. In addition to obvious flare events, variability is present also on smaller time scales and lower amplitude variations throughout the observations.

4.1.1. X-ray hardness

The light curves in connection with spectral hardness can be used to identify the origin of the variability. While in typical stellar coronal flares the emission measure of predominantly hot plasma and hence the hardness of the spectra is increased, in a pure accretion spectrum no spectral changes should accompany the brightening, since the plasma temperature only depends on the infall velocity and not the accretion rate. If, in addition, a coronal contribution with a temperature higher than that produced by accretion is present, a slight spectral softening should be observed. We calculate a hardness ratio for each light curve time bin and in Fig. 2 we show the hardness ratio vs. count rate for our sample CTTS. The hardness ratio is here defined as HR=H-S/H+S with the soft band covering the energy range $0.2 - 1.0$ keV and the hard band $1.0 - 10.0$ keV. Errors are small compared to the observed shifts in hardness ratio. A clear correlation of X-ray brightness with spectral hardness is present for BP Tau, CR Cha and SU Aur, a behaviour typical of stellar flares, suggesting a coronal origin of the variability. No strong correlation is found for variations on TW Hya, which are, however, quite small. An anti-correlation appears to be present for the larger variations, as expected for brightness changes
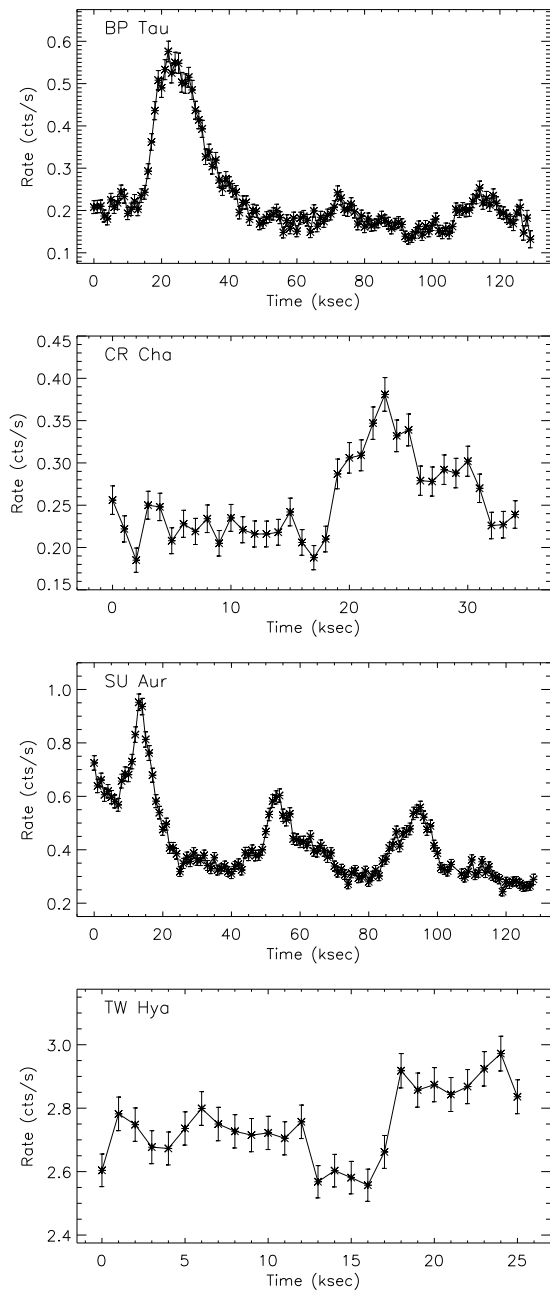
Fig. 1. Light curves and corresponding hardness ratio of the sample CTTS, PN (SU Aur – MOS) data with 1 ksec binning.

due to an increase in accretion rate. This is reflected in the slope of the linear regression curves. It is positive for BP Tau, CR Cha and SU Aur, but slightly negative for TW Hya.

To quantify the spectral changes that the CTTS are undergoing during phases of increasing emission in more
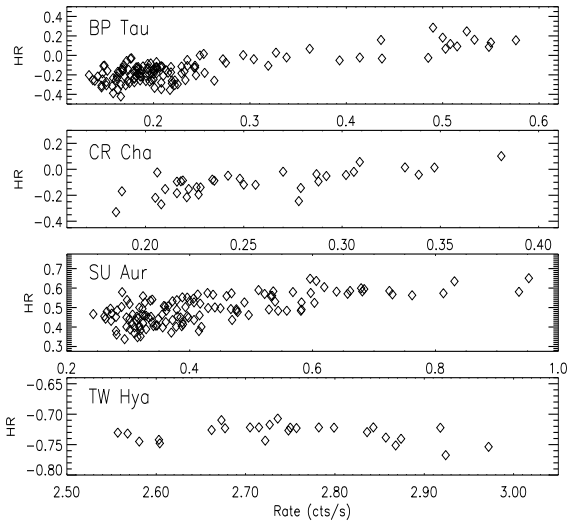
Fig. 2. Hardness ratio vs. count rate of the sample CTTS, PN (SU Aur – MOS) data with 1 ksec binning.

detail, we use their light curves to define 'high' states for BP Tau (15–37 ks), CR Cha (18.5–31.5 ks), SU Aur (0–24, 47–69, 83–101 ks) and TW Hya (> 19 ks), while the remaining time intervals are considered as quasi-quiescence. An individual spectral analysis of both states of activity is presented in Sect. 4.2.3.

4.2. Spectral analysis

The spectral analysis and its results are presented as follows. First we use the medium resolution EPIC spectra in combination with the high resolution RGS data to obtain general spectral properties like temperatures, emission measures and elemental abundances of the X-ray emitting plasma and constrain the strength of absorption present for our targets. From the RGS spectra we investigate the resolved He-like triplet of O VII to determine the densities of the emitting plasma and/or strength of the surrounding UV field. Subsequently we investigate spectral changes between the low and the high state of our sample CTTS.

4.2.1. The global spectra

The spectra of all our sample CTTS as observed with MOS1 are shown in Fig. 3, which demonstrates major differences between individual stars. While the spectra of BP Tau and CR Cha are comparable, the spectrum of SU Aur indicates the presence of large amounts of extremely hot plasma noticeable, e.g. in the very strong Fe XXV line complex at 6.7 keV. On the other hand, the X-ray spectrum of TW Hya is much softer, suggesting a more dominant accretion component. The observed spectra are also subject to absorption, affecting primarily the energy range below 1.0 keV. In these spectra the low energy slope

mainly reflects the strength of the absorption, while the high energy slope traces temperature and amount of hot coronal and flaring plasma. Inspection of the two slopes indicates that the absorption is weakest for TW Hya, moderate for BP Tau and strongest for CR Cha and SU Aur, while the coronal component is strongest and hottest for SU Aur, followed by BP Tau and CR Cha and much weaker and cooler for TW Hya.
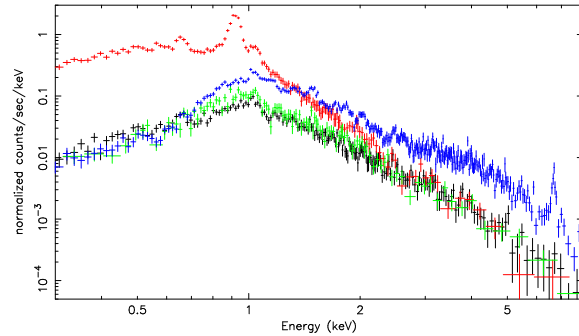
Fig. 3. Spectra of our sample CTTS for the total observation as observed with the MOS1 detector: BP Tau (black), CR Cha (green), SU Aur (blue) and TW Hya (red); bottom to top of the 1.0 keV peak. *Colour figure in electronic version.*

To quantify the physical properties of the X-ray emitting plasma we fitted the spectra of the different instruments with multi-temperature spectral models as described in Sect. 3. The results of the fitting procedure are presented in Table 3. Note again the interdependence of several fitting parameter, especially absorption, cool emission measure and corresponding abundances. However, general trends on abundances and their ratios as well as the overall shape of the emission measure distribution and their changes, which indicate the production mechanism of the X-rays, are very stable.

While spectral modelling must consider absorption, the physically most interesting quantity is the emitted, i.e. dereddened, X-ray luminosity of our targets, which is calculated in the 0.2–10. keV band using MOS data (see 3). We find that despite their very different spectral properties, all targets have an X-ray luminosity of the same order of magnitude. The hottest and most massive star SU Aur is also X-ray brightest target, followed by CR Cha, BP Tau and TW Hya with comparable X-ray luminosities. CTTS as a class are known strong X-ray emitter, but our sample stars are about a magnitude brighter than the X-ray luminosity of an average CTTS, as determined from RASS data with a mean $\log L_X$ of 29.1 (Chamaeleon) and 29.4 (Taurus) in Neuhäuser et al. (1995), Feigelson et al. (1993); this is of course no surprise since these CTTS were selected for grating observations.

Neglecting interstellar contribution, the strength of absorption depends on the amount of circumstellar material in the disk and the inclination angle of the target. The results of our spectral modelling confirm that

Table 3. Spectral results, units are N_H in $10^{21} \mathrm{cm}^{-2}$, kT in keV EM in $10^{52} \mathrm{cm}^{-3}$ and L_X in $10^{30} \mathrm{erg\,s}^{-1}$.

Par.	BP Tau	CR Cha	SU Aur	TW Hya
N_H	$1.5^{+0.1}_{-0.1}$	$2.7^{+0.4}_{-0.3}$	$3.1^{+0.1}_{-0.1}$	$0.35^{+0.04}_{-0.05}$
Fe	$0.28^{+0.04}_{-0.04}$	$0.45^{+0.08}_{-0.07}$	$0.79^{+0.05}_{-0.05}$	$0.26^{+0.02}_{-0.02}$
Si	$0.14^{+0.08}_{-0.08}$	$0.23^{+0.10}_{-0.09}$	$0.60^{+0.08}_{-0.08}$	$0.13^{+0.05}_{-0.06}$
O	$0.62^{+0.08}_{-0.06}$	$0.53^{+0.18}_{-0.14}$	$0.39^{+0.12}_{-0.11}$	$0.23^{+0.02}_{-0.02}$
Ne	$1.47^{+0.16}_{-0.14}$	$1.02^{+0.19}_{-0.17}$	$1.04^{+0.15}_{-0.14}$	$1.81^{+0.05}_{-0.05}$
kT1	$0.20^{+0.01}_{-0.01}$	$0.17^{+0.03}_{-0.03}$	$0.68^{+0.03}_{-0.02}$	$0.25^{+0.01}_{-0.01}$
kT2	$0.63^{+0.03}_{-0.03}$	$0.66^{+0.01}_{-0.02}$	$1.61^{+0.07}_{-0.10}$	$0.69^{+0.06}_{-0.02}$
kT3	$2.17^{+0.09}_{-0.09}$	$1.92^{+0.06}_{-0.10}$	$4.82^{+1.02}_{-0.84}$	$1.34^{+0.03}_{-0.05}$
EM1	$3.48^{+0.89}_{-0.69}$	$4.96^{+4.05}_{-2.49}$	$11.66^{+0.87}_{-0.86}$	$19.16^{+0.74}_{-0.82}$
EM2	$5.28^{+0.64}_{-0.56}$	$10.67^{+1.60}_{-1.53}$	$25.27^{+2.87}_{-3.96}$	$1.23^{+0.54}_{-0.84}$
EM3	$10.30^{+0.43}_{-0.29}$	$9.27^{+0.73}_{-0.54}$	$15.79^{+4.02}_{-2.59}$	$3.12^{+0.52}_{-0.51}$
χ^2(d.o.f.)	0.97 (1281)	1.20 (700)	1.20 (1027)	1.57 (878)
L_X obs.	1.3	1.4	4.5	1.5
L_X emit.	2.3	3.1	8.1	2.0

absorption is lowest for TW Hya. Our value for the interstellar column density N_H is slightly higher than the one used by Stelzer & Schmitt (2004), who fixed N_H at $2 \times 10^{20}\, cm^{-2}$. No values are given for the *Chandra* data in Kastner et al. (2002), but the authors refer to previous work (Kastner et al., 1999) where values determined from ROSAT PSPC ($0.5 \times 10^{21}\, cm^{-2}$) and higher ones from ASCA SIS ($2.9 \times 10^{21}\, cm^{-2}$) with a consequently larger emission measure. These differences were attributed to temporal changes in the circumstellar environment, but the poorer spectral resolution and sensitivity of the used instruments, the strong interdependence between N_H and EM, that is also present in models from the individual instruments operated simultaneously onboard XMM-Newton, suggests that limited spectral resolution of the instruments combined with uncertainties in the code used for modelling the spectra is a possible explanation for those discrepancies. Recently Herczeg et al. (2004) analysed the Ly α profile of TW Hya as measured by HST/STIS and put a stringent upper limit on the hydrogen column density with $N_H \leq 5 \times 10^{19}\, cm^{-2}$. We therefore adopted this value and additionally fitted the spectra with the reduced absorption value, which results in a comparable model, but with accordingly lower emission measure at cool temperatures.

We find intermediate values of the interstellar column density N_H for BP Tau, which are in good agreement with optical measurements using the standard conversion between N_H and A_v viz. $N_H = 2 \times 10^{21} A_v\, cm^{-2}$; values taken from literature are in the range $1.0 - 2.0 \times 10^{21}\, cm^{-2}$ (Gullbring et al., 1998; Hartigan et al., 1995). Even stronger absorption is found for CR Cha, also in good agreement with optical measurements, with a literature value of $2.7 \times 10^{21}\, cm^{-2}$ (Gauvin & Strom, 1992). The strongest absorption is found for SU Aur, here the large inclination angle results in a strong and probably also variable absorption. Optical and NIR measurements give a range of values ranging from no absorption up to $3 \times 10^{21}\, cm^{-2}$ (DeWarf et al., 2003). While commonly a lower N_H value is adopted, our result is comparable with

the larger values and a much weaker absorption significantly worsens the quality of the fit.

The emission measure distributions (EMD) of our sample CTTS differ significantly among the sample stars. The hottest EMD is clearly present in SU Aur, with significant amounts of plasma at temperatures around 50 MK detected. Due to the very strong absorption no definite conclusions about a possibly existing cool temperature part of the EMD can be drawn. Since SU Aur is of average age in our sample and the major difference to the other stars is its spectral type, an explanation for its outstanding properties might be a dependence of the evolutionary time scale on spectral type, i.e stellar mass. The EMDs of BP Tau and CR Cha are similar, with the temperatures of BP Tau being slightly higher and a larger fraction of plasma residing in the hottest component; plasma at temperatures around $20 - 25$ MK must be present in those stars. The picture is very different for TW Hya, where the cool component with temperatures around 3 MK clearly dominates the EMD. Plasma at medium temperatures with 5-10 MK appears to be nearly absent, while in the hot component plasma temperatures around 15 MK are reached; however, this component is cooler and significantly weaker than in the other objects. We emphasise that this finding is independent of the used value of N_H.

As far as abundances are concerned, one property is common to all CTTS analysed: Most abundances are subsolar, sometimes at considerable level, while neon is commonly found at solar abundance or even significantly enhanced. The noble gas neon is more abundant compared to iron, oxygen and silicon for all targets, and in the most extreme case TW Hya these ratios are of the order of 10 (see Table. 3). Iron and silicon are less abundant than oxygen in BP Tau and CR Cha, while all three elements are strongly depleted in TW Hya. The very active star SU Aur appears to be an exception, with only oxygen apparently being more strongly depleted, but here very strong absorption affects the results based on cool lines. These metal anomalies were interpreted for TW Hya by Stelzer & Schmitt (2004) through a depletion of grain forming element in the accreted material, consistent with the low observed IR excess and also plausible when considering the age of TW Hya. Drake et al. (2005) argue, that for TW Hya coagulation of grains into larger bodies finally withdraws these elements from the accretion process, while for the younger BP Tau dust and grains at corotation radius ($R_{co} = (\frac{GM}{\omega^2})^{1/3}$) will sublimate and rereleased into the accretion process. The coagulation of significant amounts of material into centimeter sized particles in the disk around TW Hya is supported by the radiospectrum at centimeter wavelength as observed with the VLA (Wilner et al., 2005).

However, stars without accretion but with an active corona also show a distinct abundance pattern, commonly known as IFIP effect, i.e. an enhancement of elements with a high first ionisation potential. While iron and silicon are low FIP elements, oxygen is an intermediate and neon a high FIP element. The IFIP-effect is observed for

BP Tau and CR Cha, thus pointing towards the typical abundance pattern for coronal plasma. Moreover, Argiroffi et al. (2005) analyse the spectra of TWA5, a young multiple system dominated by a M dwarf and also located in the TW Hya association. These object is classified as CTTS (via Hα), but is probably a WTTS since there is no evidence for a disk in the IR, but it also shows a high neon to iron ratio similar to TW Hya with spectral properties very much reminiscent of active stars. While environmental conditions may be invoked to explain the abundance anomalies, Robrade & Schmitt (2005) showed that a high neon to iron ratio is common for active M dwarfs, with most extreme ratios found in very young and therefore more active stars. We further point out that our CTTS belong to different star formation regions and their X-ray emission is predominantly generated by different processes, yet no significant difference in the abundance pattern was found. Therefore it appears reasonable to attribute the observed abundance anomalies in the sample CTTS to a combined action of metal depletion of the accreted matter via grain forming and the coronal IFIP effect. Grain forming is only important for the accretion plasma of older and more evolved objects, while the IFIP effect is present in plasma generated in active coronae.

4.2.2. The O VIII and O VII lines

We used the CORA line fitting program to determine the strengths of the resonance, intercombination and forbidden lines in the He-like triplet of O VII (21.6, 21.8, 22.1 Å) and the Ly α line of O VIII at 18.97 Å as measured with RGS1. The spectra of the sample CTTS covering this wavelength-region are shown in Fig. 4, the measured line counts of the O VII triplet and the derived densities are given in Table 4. We used the relation $f/i = \frac{R_0}{1 + \phi/\phi_c + ne/N_c}$ with f and i being the line intensities in the forbidden and intercombination line, R_0 the low density limit of the line ratio with a adopted value of 3.95, N_c the critical density and ϕ/ϕ_c the radiation term, which is neglected in our calculations. Values used in the calculations were taken from (Pradhan & Shull, 1981); we caution that the presence of strong radiation fields would lead us to overestimate plasma densities. The O VII triplet traces the cool plasma around 2 MK, is essentially free of stronger blends and therefore well suited to investigate possible accretion scenarios, while O VIII traces slightly hotter plasma around $3-5$ MK.

The analysis of the oxygen triplet of BP Tau and its implications are presented by Schmitt et al. (2005), results obtained for TW Hya are presented in Stelzer & Schmitt (2004). Our analysis here is - technically – slightly different, but we arrive at the same results as found by Stelzer & Schmitt (2004). The data of CR Cha, which unfortunately has only moderate S/N ratio and larger absorption, is analysed here for the first time. The O VIII line is here clearly detected, the same applies to the O VII triplet, which, however, looks quite peculiar. Resonance
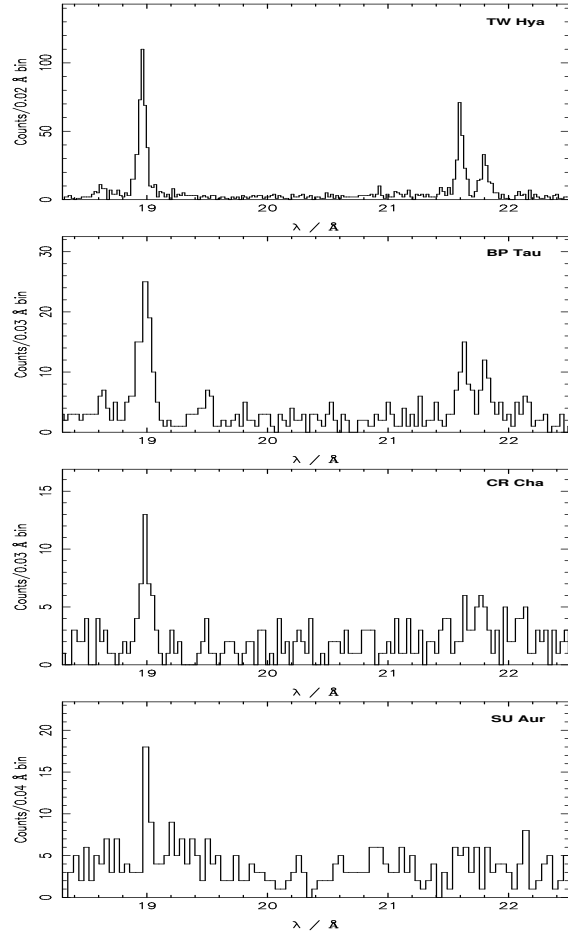
Fig. 4. Spectra of the sample CTTS covering the O VIII line and the O VII triplet as measured with the RGS1 detector. Absorption increases from the top to bottom.

and forbidden lines have about the same strength, and the intercombination line is actually the strongest line in the triplet. Because of the poor SNR the errors in the line count measurements are quite substantial; also the g-ratio (f+i)/r is found to be 2.9 ± 2.2, but is because of its large error actually consistent with unity as theoretically expected. The observed f/i ratio is well below unity despite its considerable measurement error, as observed for TW Hya and BP Tau.

In SU Aur the O VII triplet is absent, ruling out any quantitative analysis. We attribute the absence of O VII to the strong (circumstellar) absorption and the presence of extremely hot plasma, which increases the continuum emission at these wavelengths. Some weak emission may actually be present at the position of the oxygen triplet, but neither the intercombination nor forbidden line are clearly detected. The O VIII Lyα line is however clearly present and attenuation increases only by a factor of roughly two between the two wavelengths. A strong

O VII triplet should therefore be detected in the spectra, even with SU Aur's strong absorption. This indicates, that large amounts of cool plasma do not exist on SU Aur.

Table 4. Measured RGS1 line counts of the O VIII and O VII-triplet (r,i,f) lines and calculated densities, taking into account the effective areas at the respective wavelengths.

Par.	BP Tau	CR Cha	SU Aur	TW Hya
O VIII	94.5±11.4	36.6±7.1	33.1±7.5	453.0±23.8
O VII r	44.9±8.4	7.5±4.9	-	234.9±17.3
O VII i	34.5±7.6	13.5±5.6	-	113.5±12.9
O VII f	11.6±5.3	8.7±4.8	-	6.1±5.1
f/i (obs.)	0.34±0.17	0.64±0.44	-	0.054±0.045
$n_e (10^{11} cm^{-3})$	$3.2^{+3.5}_{-1.2}$	$1.6^{+4.2}_{-0.8}$	-	$21.1^{+107}_{-9.7}$

Comparing the ratio of O VIII to the O VII line counts, we find the largest (observed) ratio for TW Hya. However, absorption attenuates the O VII lines more strongly than the O VIII line and using our determined values for N_H, in the unabsorbed ratio the inverse trend is observed. While typical active coronae, as well as all other sample CTTS, show a rise of the EMD in this temperature regime, we find that in the accretion dominated spectrum of TW Hya the bulk of plasma has temperatures around $2.5-3$ MK, consistent with the results of the global fitting.

Investigating the O VII triplets of our sample CTTS, we find that derived densities differ from those of cool main sequence stars. While typical coronal plasma is compatible with and for very active stars no more than an order of magnitude above the low density limit, i.e f/i $\sim$ 2–4 and $\log n_e \sim$ 9–10 (Ness et al., 2002), all CTTS with detected oxygen triplets deviate strongly from the low density limit. BP Tau and CR Cha show a density about two orders of magnitude lower, for TW Hya it is even three orders of magnitude lower, suggesting extremely high densities for the cool plasma of the CTTS. Alternatively, strong UV radiation fields would explain the measured line ratios, but these fields cannot be produced by the stellar photospheres of the underlying cool stars, therefore the radiation fields would have to be attributed to an additional hotter component, i.e. an accretion shock.

Thus the derived densities may be considered as an upper limit, but we point out that even in the case of UV radiation contributing to the low f/i-ratio accretion must occur, since also a strong UV radiation points to the presence of an accretion-induced shocks. Furthermore, the coronal plasma is likely to additionally contribute to the flux in the O VII-triplet. It was shown in Schmitt et al. (2005) that the f/i-ratio for BP Tau is even lower, when only the quasi-quiescent state is considered in the analysis. This is plausible, because the f/i-ratio from the coronal contribution is expected to be near the low density limit and therefore the densities in the accretion spot are under-estimated in this calculation and also appear as an lower limit. Since the size of the accretion spots or filling factors as well as the amount of coronal plasma contributing at low temperatures are not known precisely, we just note that there are two competing effects on the derived den-

sities present, but they are not calling the accretion scenario in question. While the poor data quality for CR Cha prevents a more detailed discussion as for BP Tau, the derived f/i-ratio is also significantly lower than for coronal sources and the derived plasma density is in the same order of magnitude as it is for BP Tau. The derived results for CR Cha fit into the picture and support the accretion scenario for CTTS as a class. Therefore we conclude that the cool plasma of TW Hya is strongly dominated by accretion, while in the cases of BP Tau and CR Cha and possibly also of SU Aur accretion is present, but with additional cool coronal plasma. However, the emission measure of this component is hard to constrain given the SNR of our data. These findings agree well with the conclusions drawn in the previous section.

4.2.3. Spectral changes

To investigate the spectral changes between the phases of different X-ray brightness, we use the more sensitive EPIC data, separated in low and high states as defined in Sect 4.1 and utilise the previously derived best fit models. A comparison of the PN spectra of BP Tau and TW Hya during high and low state is shown in Fig. 5, where the high state represents the strong flare on BP Tau (factor 2.4) and the period of slightly enhanced emission of TW Hya (factor 1.1). The differences between the spectra of the high and low state are nearly reverse for the two CTTS. While for BP Tau the spectrum hardens and the most significant changes are seen at higher energies, pointing to a coronal origin of the changes, the TW Hya spectra are identical at higher energies and only at lower energies the emission is enhanced, pointing to a higher accretion rate. The changes are more pronounced for BP Tau due to the much higher increase in X-ray brightness.

Table 5. EMD of our sample CTTS in low (left) and high (right) state as derived from PN data (MOS for SU Aur), N_H in 10^{21}cm^{-2}, kT in keV and EM in 10^{52}cm^{-3}.

Par.	BP Tau		CR Cha	
N_H	1.5		2.6	
kT1	$0.18^{+0.02}_{-0.02}$		$0.19^{+0.06}_{-0.04}$	
kT2	$0.50^{+0.07}_{-0.05}$	$0.67^{+0.07}_{-0.07}$	$0.65^{+0.03}_{-0.03}$	
kT3	$2.12^{+0.15}_{-0.14}$	$2.71^{+0.26}_{-0.14}$	$1.71^{+0.20}_{-0.19}$	$1.99^{+0.23}_{-0.14}$
EM1	$4.5^{+0.5}_{-0.5}$	$2.9^{+1.0}_{-1.0}$	$4.5^{+1.5}_{-1.2}$	$6.3^{+2.9}_{-2.3}$
EM2	$5.9^{+0.4}_{-0.5}$	$9.8^{+0.9}_{-1.2}$	$10.8^{+1.5}_{-1.7}$	$11.7^{+1.4}_{-1.9}$
EM3	$6.8^{+0.5}_{-0.4}$	$23.9^{+1.4}_{-1.7}$	$7.7^{+0.9}_{-0.9}$	$13.3^{+1.3}_{-1.4}$
χ^2(dof)	0.89 (778)		1.12 (414)	
Par.	SU Aur		TW Hya	
N_H	3.1		0.35	
kT1	$0.69^{+0.03}_{-0.02}$		$0.24^{+0.01}_{-0.01}$	
kT2	$1.62^{+0.09}_{-0.07}$		$0.60^{+0.09}_{-0.06}$	
kT3	$5.08^{+1.27}_{-0.81}$		$1.37^{+0.11}_{-0.05}$	
EM1	$10.8^{+1.0}_{-0.5}$	$11.9^{+1.1}_{-0.3}$	$21.5^{+0.4}_{-0.6}$	$24.5^{+0.4}_{-0.8}$
EM2	$21.2^{+1.8}_{-2.1}$	$29.9^{+4.1}_{-4.3}$	$2.3^{+0.5}_{-0.4}$	$3.2^{+1.1}_{-0.3}$
EM3	$6.9^{+1.9}_{-1.9}$	$22.7^{+4.4}_{-4.3}$	$2.8^{+0.3}_{-0.6}$	$2.3^{+0.5}_{-0.8}$
χ^2(dof)	1.10 (929)		1.27 (496)	
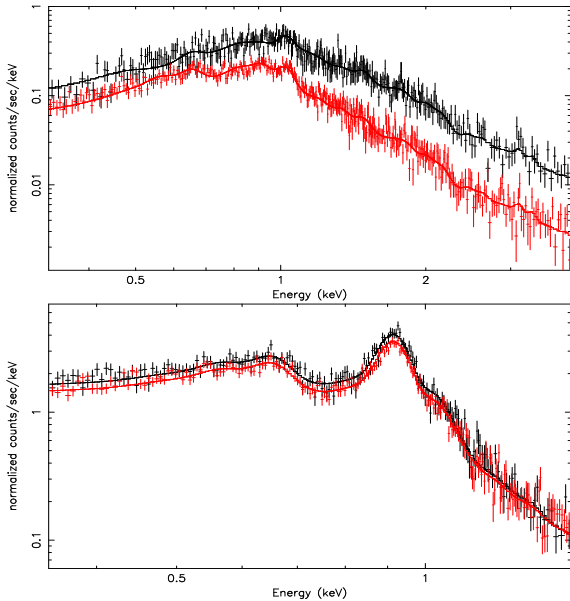
Fig. 5. Spectra of BP Tau (top) and TW Hya (bottom) during high (black) and low (red) state with model fits.

No significant changes in the elemental abundances were detected between high and low state, therefore we fixed strength of absorption and abundances at those values that were derived for the total observation and remodelled the EMD for the selected time intervals. If we find – using temperature as a free parameter for each state – no significant difference in the temperature components, it is tied for both sets of data.

The results of the individual modelling of the low and high states for our sample CTTS are summarised in Table 5. Very different effects on the derived temperature structures are found and also the largest increase in emission measure is found in different temperature components for our CTTS. The rise in temperature and the presence of a larger amount of additional hot plasma with temperatures around 30 MK during the high state reflects the coronal origin of the increased X-ray brightness for BP Tau. Flaring affects also the emission measure at moderate temperatures as represented by the increased emission measure and a shift to higher temperatures, which are in the range of $6-8$ MK. A more moderate increase of temperatures and additional plasma at moderate temperatures but again predominantly in the hot component is found for CR Cha. This also points to a coronal origin of the increased brightness and is consistent with the observed more moderate flare. Also for SU Aur coronal activity is the explanation for the increased X-ray brightness, with large amounts of additional hot plasma at temperatures of $20-50$ MK. The flare plasma is extremely hot, but since large amounts of extremely hot plasma are already present during quasi-quiescence, no significant increase in temperature accompanies the brightening. The coolest detected

component of SU Aur, which already has temperatures around 8 MK, is again not strongly affected by the flaring. In contrast, none of these signatures are connected with the flux increase for TW Hya. No differences in the temperature structure were found and the additional plasma is found mainly in the coolest temperature component, supporting the scenario of increased accretion. With $2.5-3$ MK this component is much cooler than typical flare plasma temperatures, but fits to the temperatures as expected for plasma generated in an accretion spot.

5. Summary and Conclusions

We have presented the first comparative study using high and medium resolution X-ray spectra of classical T Tauri stars observed with the new generation X-ray telescopes so far. The results derived from these data are complementary to the ones obtained from the large sample of COUP sources, since high-resolution spectroscopy and low-energy sensitivity additionally permits the investigation of the cool plasma components.

Using the XMM-Newton observations of BP Tau, CR Cha, SU Aur and TW Hya we determined X-ray properties of accreting young pre-main sequence stars. Two different mechanisms are likely to contribute to the production of X-ray emission in those objects, first coronal, i.e. magnetic activity, and second, magnetically funneled accretion. We investigate variability, global spectra and density sensitive lines to check for the presence and relative contribution of these two mechanisms for the individual objects. For this purpose we utilize the emission measure distribution and its changes, specific abundance pattern and density diagnostics. Interpreting very high densities as indicator for accretion shocks and a high temperature component as indicator for coronal activity, we derive the following conclusions, which are likewise supported by the analysis of abundance analysis and spectral variability. In all targets where the O VII-triplet is observable density analysis leads to higher densities than observed in any pure coronal source. Additionally, a high temperature component is present in all targets. We therefore argue that both X-ray generating processes are present in our sample CTTS, but at very different levels and importance in individual objects.

The X-ray emission of BP Tau is overall dominated by coronal activity and a stronger flare of again probably coronal origin is observed. Even in quasi-quiescent phases the emission measure distribution is dominated by medium and hot temperature plasma whereof significant amounts are present at temperatures around 20 MK. However, the analysis of density sensitive lines confirms that accretion is also present and actually dominates the cool plasma with temperatures of a few MK. CR Cha is similar to BP Tau but more strongly absorbed and the coronal plasma temperatures are slightly lower. It also appears to be dominated by the coronal contribution, likewise there is evidence for high density plasma at cool temperatures. SU Aur is the by far brightest and with tem-

peratures of at least up to 50 MK hottest X-ray source in our sample. A powerful and active corona is the essential contributor to its X-ray spectrum and frequent flaring is observed. Unfortunately the very strong absorption prevents definite conclusions about the cooler plasma component. TW Hya is the other hand strongly dominated by accretion, but an additional coronal component is clearly detected. It is the prototype and still the outstanding and only example of an accretion dominated star. Most of its plasma is at cool temperatures typical for accretion spots and it exhibits by far the lowest O VII f/i ratio. Also the highest neon to oxygen ratio, which may be interpreted via depletion of grain forming element, is found for TW Hya. This is plausible since TW Hya is the oldest and most evolved object in our sample. In the other sample CTTS neon is also enhanced, but the abundance pattern is more reminiscent of the inverse FIP effect found in active stars.

Considering the global picture of stellar evolution towards the main sequence, we find that magnetic processes play a major role in high energy phenomena in all our sample CTTS. While the specific stellar evolution and its timescale might depend on e.g. spectral type, the generation of X-rays via accretion and coronal activity is apparently a common feature of CTTS in general.

References

Anders E., Grevesse N. 1989, Geo- et Cosmochimica Acta, 53, 197

Argiroffi, C., Maggio, A., Peres, G. et al. 2005, A&A, 439, 1149

Arnaud, K.A. 1996, ASP Conf. Series, 101, 17

Asplund, M. 2005, ASP Conf. Series, 336, 25

Calvet, N., Gullbring, E. 1998, ApJ, 509, 802

DeWarf, L.E., Sepinsky, J.F., Guinan, E.F., et al. 2003, ApJ, 590, 357

Drake, J.J., Testa, P., Hartmann, L. 2005, ApJ, 627, L149

Ehle, M., Breitfellner, M., Gonzales Riestra, M., et al. 2003, XMM-Newton User's Handbook

Favata, F., Flaccomio, E., Reale, F., et al. 2005, ApJS, 160, 469

Feigelson, E.D., DeCampli, W.M. 1981, ApJ, 243, L89

Feigelson, E.D., Kriss, G.A. 1989, ApJ, 338, 262

Feigelson, E.D., Casanova, S., Montmerle, T., Guibert, J. 1993, ApJ, 416, 623

Feigelson, E.D., Montmerle, T. 1999, Ann. Rev. A&A, 37, 363

Feigelson, E.D., Gaffney, J.A., Garmire, G. et al. 2003, ApJ, 584, 911

Grevesse, N., Sauval, A.J. 1998, Space Sci. Rev., 85, 161

Gauvin, L.S. and Strom, K.M. 1992, ApJ, 385, 217

Güedel, M., Skinner, S.L., Briggs, K.R., et al. 2005, ApJ 626, L53

Gullbring, E., Barwig, H., Schmitt, J.H.M.M. 1997, A&A, 324, 155

Gullbring, E., Hartmann, L., Briceno, C., Calvet, N. 1998, ApJ, 492, 323

Hartigan, P., Edwards, S., Ghandour, L. 1995, ApJ, 452, 736

Herczeg, G.J., Wood, B.E., Linsky, J.L., et al. 2004, ApJ, 607, 369

Kastner, J.H., Huenemoerder, D.P., Schulz, N.S., et al. 1999, ApJ, 525, 837

Kastner, J.H., Huenemoerder, D.P., Schulz, N.S., et al. 2002, ApJ, 567, 434

Kirsch, M.G.F., Altieri, B., Chen, B., et al. 2004, astro-ph/0407257

Loiseau, N. (edt.), Ehle, M., Pollock, A.M.T., et al. 2004, User's Guide to XMM-Newton Science Analysis System Issue 3.1

Makarov, V.V., Fabricius, C. 2001, A&A, 368, 866

Meeus, G., Sterzik, M., Bouwman, J., Natta, A. 2003, A&A, 409, L25

Muzerolle, J., Calvet, N., Hartmann, L, D'Alessio, P. 2003, ApJ, 597, L149

Natta, A., Meyer, M.R., Beckwith, S.V.W. 2000, ApJ, 534, 838

Ness, J.-U., Schmitt, J.H.M.M., Burwitz, V., et al. 2002, A&A, 394, 911

Ness, J.-U., Wichmann, R. 2002, AN, 323, 129

Neuhäuser, R., Sterzik, M.F., Schmitt, J.H.M.M. et al. 1995, A&A, 297, 391

Pallavicini, R., Franciosini, E., Randich, S. 2004, MSAI, 75, 434

Pradhan, A.K., Shull, J.M. 1981, ApJ, 249, 821

Preibisch, T., Kim, Y.-C., Favata, F., et al. 2005, ApJS, 160, 401

Reipurth, B., Pedrosa, A., Lago, M.T.V.T. 1996, A&AS, 120, 229

Robrade, J., Schmitt, J.H.M.M. 2005, A&A, 435, 1073

Schmitt, J.H.M.M., Robrade, J., Ness, J.-U., et al. 2005, A&A, 432, L35

Shu, F., Najita, J., Ostriker, E., et al. 1994, ApJ, 429, 781

Smith, R.K., Brickhouse, N.S., Liedahl, D.A., Raymond, J.C. 2001, ASP Conf. Series, 247, 161

Stelzer, B., Neuhäuser, R. 2001, A&A, 377, 538

Stelzer, B., Schmitt, J.H.M.M. 2004, A&A, 418, 687

Walter, F.M., Kuhi, L.V. 1981, ApJ, 250, 254

Wichmann, R., Bastian, U., Krautter, J., et al. 1998, MNRAS, 301, L39

Wilner, D.J., Alessio, P.D., Calvet, N., et al. 2005, ApJ, 626, L109

Zuckerman, B., Webb, R.A., Schwartz, M., Becklin, E.E. 2001, ApJ, 549, L233

Chapter 6

Detection of X-ray emission from β Pictoris with XMM-Newton: a cool corona, a boundary layer or what?

M. Hempel, J. Robrade, J. - U. Ness, J. H. M. M. Schmitt

Astronomy
&
Astrophysics

Detection of X-ray emission from β Pictoris with XMM-Newton: a cool corona, a boundary layer or what?

M. Hempel[1,2], J. Robrade[2], J.-U. Ness[2,3], and J. H. M. M. Schmitt[2]

[1] AIU Jena, Schillergäßchen 2-3, 07745 Jena, Germany
   e-mail: marc@astro.uni-jena.de
[2] Hamburger Sternwarte, Gojenbergsweg 112, 21029 Hamburg, Germany
[3] Department of Physics, Rudolf Peierls Centre for Theoretical Physics, University of Oxford, 1 Keble Road,
   Oxford OX1 3NP, UK

Abstract. β Pictoris (HR 2020) is the most prominent prototype of stars with circumstellar disks and has generated particular interest in the framework of young planetary systems. Given its spectral type A5, stellar activity is not expected. Nevertheless, resonance lines of C III and O VI typical for a chromosphere and transition region have been unambiguously detected with FUSE. We present results from an XMM-Newton observation of β Pic and find evidence for X-ray emission. In particular, we detected an emission of O VII at 21.6 Å with the MOS detectors. These findings present a challenge for the development of both stellar activity and disk models. We discuss and investigate various models to explain the observed emission including the presence of a cool corona and a boundary layer.

Key words. stars: activity – stars: circumstellar matter – stars: individual: HR 2020 – ultraviolet: stars – X-rays: stars

1. Introduction

The A5 star β Pictoris (HR 2020) is well-known for its circumstellar (CS) debris disk (Smith & Terrile 1984) seen nearly edge-on. Spectroscopic observations exhibit conspicuous and highly variable narrow absorption lines interpreted as *falling evaporating bodies* (FEB, Ferlet et al. 1987): kilometre-sized cometary-like objects on star-grazing orbits pass near β Pic and evaporate gas leading to imprints up to $v_{\rm K} \approx 400\,{\rm km\,s^{-1}}$ in the photospheric spectrum. Among other stars like Vega and α PsA, CS disks have generated particular interest in the framework of young planetary systems. Although numerous stars possessing CS material have been found so far, β Pic is the most prominent prototype of stars with a CS disk and thus β Pic presents a challenge for the development of theoretical disk models (see e.g. Kamp et al. 2003). In this context it is necessary to determine the temperature structure of disks in order to obtain chemical compositions and disk masses. Since the chemistry in CS disks is driven by the stellar radiation field, such models require a realistic stellar flux as input. Upper atmospheric layers like chromospheres will have a pronounced effect on disks since the chromospheric UV photons lead to warmer disks due to an increase in the heating rate. The same applies to the presence of a X-ray radiation field from a possible stellar corona. Depending on the spectral type of the host star it is thus necessary to account for the chromospheric UV and coronal X-ray flux. For the case of HR 4796A/B, consisting

of an A0V-type star and a M dwarf companion, this has been carried out by Chen & Kamp (2004) in their study of the CS environment of this source. Similar to β Pic, HR 4796A harbours CS material which has been successfully imaged (Schneider et al. 1999). From the companion's ROSAT X-ray flux of $F_{\rm X} \lesssim 2 \times 10^{-4}$ erg/cm^2/s at the position of HR 4796, Chen & Kamp (2004) estimated that X-ray heating due to the M dwarf is insignificant for the case of HR 4796A/B.

In general, A-type stars are not considered to be chromospheric and coronal stars. Radiation hydrodynamic model calculations show that they do not possess significant outer convection zones (Freytag et al. 1996) and therefore one does not expect chromospheric and coronal X-ray emission from these stars. Yet, small turbulent velocities are present in A-type stars. Holweger et al. (1997) determined the microturbulence of β Pic to be $\xi_{\rm t} = 4 \pm 0.3\,{\rm km\,s^{-1}}$, a value slightly higher than what is generally expected for A stars.

In order to study the possible occurrence of chromospheres and transition regions in A-type stars Simon et al. (2002) have carried out FUSE observations in the C III at 977/1175 Å and O VI at 1032/1037 Å lines for a sample of seven stars in the temperature range between $T_{\rm eff} \sim 7800$ K and 8600 K. They find an abrupt drop of the chromospheric emission in a very narrow temperature range of just ± 50 K, centered around $T_{\rm eff} \approx 8250$ K. In the sample of stars analyzed by Simon et al. (2002) the A4 V star τ^3 Eri is the hottest ($T_{\rm eff} = 8210$ K)

Table 1. Observation log of β Pic.

Instrument	Filter	Mode	Duration (s)	Observation time	Good times (ks)
MOS1	Thick	Full Frame	73 668	2004-01-04 18:52:18–2004-01-05 15:20:06	72
MOS2	Thick	Full Frame	73 677	2004-01-04 18:52:13–2004-01-05 15:20:10	72
PN	Medium	Full Frame	72 036	2004-01-04 19:14:34–2004-01-05 15:15:10	55
RGS1		Spectroscopy	73 912	2004-01-04 18:51:30–2004-01-05 15:23:22	–
RGS2		Spectroscopy	73 913	2004-01-04 18:51:35–2004-01-05 15:23:28	–

main-sequence star known to date to show evidence of hot material in a chromosphere and transition region. However, X-ray emission from τ^3 Eri has so far not been detected; it shows up neither as a source in the ROSAT all-sky survey nor was it detected in *Einstein Observatory* pointed observations (cf., Schmitt et al. 1990). Interestingly, the effective temperature of τ^3 Eri is similar to that of β Pic (T_{eff} = 8200 K, Holweger et al. 1997). The steep decline of the boundary line for convection as found by Simon et al. (2002) is consistent with recent stellar structure models (Christensen-Dalsgaard 2000; Kupka & Montgomery 2002).

The expected absence of X-ray emission from A-type stars is verified from ROSAT all-sky survey observations, which show a much lower detection rate for A-type stars as compared to F- or G-type stars (cf., Schmitt & Liefke 2004). In the X-ray picture, the "earliest" late-type star showing magnetic activity as evidenced through X-ray emission is the nearby, single A7V star Altair with $L_{\text{X}} = 6.4 \times 10^{27}$ erg/s (Hünsch et al. 1998).

Nevertheless some A-type stars do show significant X-ray emission (Hünsch et al. 1999). These X-ray detections are usually ascribed to unidentified late-type companions, although it is difficult to rule out an intrinsic X-ray flux of the A-type stars. Support for this scenario has been derived by Schmitt & Kürster (1993), who observed the eclipsing binary system α CrB with ROSAT, an eclipsing binary system consisting of an A0 V and a G5 V star. The X-ray light curve of the system shows a total X-ray eclipse during secondary optical minimum, with the G star behind the A star. The totality of the eclipse demonstrates that – as "expected" – the A-type component in α CrB is X-ray dark and that the X-ray flux arises essentially exclusively from the late-type companion. Furthermore, Chung et al. (2004) detected Doppler shifts in the eclipsing binary Algol, consisting of a B8 V primary and a K2 IV secondary, ascribed to the orbital motion of the K2 star Algol B. Their *Chandra* HETGS observations thus demonstrate that the X-ray emission of Algol is dominated by the K2 secondary while the early-type primary component is X-ray faint and most likely X-ray dark.

In the case of β Pic no convincing evidence of X-ray emission or any other signature of magnetic activity from the star itself has been found so far. However, a study based on FUSE spectra by Deleuil et al. (2001) led to the surprising result that β Pic may actually show signatures of stellar activity. The FUSE observations obtained by Deleuil et al. (2001) show pronounced emission lines of C III at 977.020/1175.711 Å and of O VI at 1031.926/1037.617 Å, respectively. Such highly ionized species are a typical signature of the presence of a chromosphere-transition region complex, which consequently

led Bouret et al. (2002) to the development of a magnetic activity scenario for β Pic on the basis of their FUSE spectra.

Starting from the FUSE detection of O VI emission lines from β Pic, it is natural to also expect emission lines from O VII, which can be conveniently diagnosed with XMM-Newton. We therefore carried out a deep X-ray observation with XMM-Newton in order to determine the X-ray emission level from β Pic especially in this line and the purpose of this paper is the presentation of this observation and a discussion of our results.

2. Observations, data analysis and results

On 2004 January 4 we observed β Pic for 73.6 ks with XMM-Newton; details of the observation are given in Table 1.

Data were collected with all X-ray detectors onboard XMM-Newton, the EPIC (European Photon Imaging Camera) and RGS (Reflection Grating Spectrometer) detectors. A detailed description of the XMM-Newton instruments can be found in Ehle et al. (2003). The XMM-Newton data reduction was carried out using the standard XMM-Newton Science Analysis System (SAS) routines, version 5.4.1 and standard selection criteria were applied for filtering the data. The EPIC detectors were operated with two different filters, the PN camera with the medium filter, the two MOS cameras with the thick filter. The PN observation is more strongly affected by proton contamination, which results in a total good time of 55 ks for the PN camera while the MOS observations provide a good time of 72 ks each. Analysis of EPIC data was performed in the energy range 0.2–12.0 keV for the MOS and 0.2–15.0 keV for the PN detector. In the RGS no useful signal could be detected from β Pic, therefore we restricted our analysis to the EPIC data.

2.1. XMM-Newton EPIC PN results

In the EPIC PN image a source can be clearly identified at the precise position of β Pic; extracting the photons with their individually measured energies we constructed an X-ray spectrum as plotted in Fig. 1. 216 source photons were extracted from a circular region with a 20″ radius around the nominal position of β Pic. For the spectrum, 723 background photons were extracted from a four times larger background region on the same CCD. The EPIC PN spectrum clearly shows the typical spectral shape of optical contamination of the CCD chips (see, e.g., Ness et al. 2004), and therefore no claim of a X-ray detection can be made on the basis of the EPIC PN observation alone.
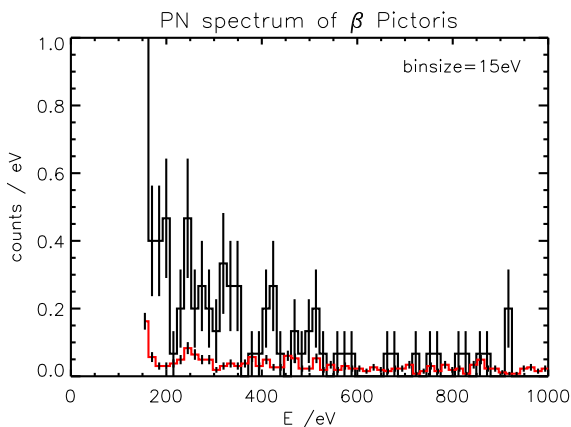
Fig. 1. The PN spectrum of β Pic applying a binsize of 15 eV (black, upper curve) and the background level (red/grey, lower curve). Note the significant difference of both histograms in the range between 200 eV and 500 eV.

2.2. XMM-Newton EPIC MOS results

Due to the fact that, on the one hand, the FUV observations of β Pic with FUSE (Deleuil et al. 2001) clearly detected OVI emission, but on the other hand, the EPIC PN data show no clear X-ray signal, we specifically searched for emission from OVII in the EPIC MOS data. Hot plasma in the temperature range $5.6 < \log T$ [K] < 6.1 produces strong OVII emission lines in the He-like triplet at wavelengths of 21.6 Å, 21.8 Å and 22.1 Å, respectively, corresponding to energies of 574 eV, 569 eV, and 561 eV with very little continuum emission. Since the individual triplet lines cannot be resolved in the EPIC MOS detectors with their medium spectral resolution, we searched for photons from this triplet in a narrow energy band centered around 565 eV $\pm$ 100 eV, *selected a priori* to contain basically all triplet photons. A circular source extraction region with a 20″ radius around the nominal position of β Pic was chosen. In order to determine a reliable background value we extracted photons from various source free regions on the central CCD of the MOS detectors; the total area chosen for background determination is 111 times larger than the source region. The same exercise was also carried out for other energy bands below and above the energy interval centered on the OVII triplet energies in order to search for possible additional source signals and to check our background estimation procedures. The results of these extraction procedures are summarized in Table 2, where we list for a total of 6 energy bands (the band 0.465–0.665 keV is centered on the OVII triplet) the extracted source cell counts for MOS1, MOS2 and their sum, the (scaled) extracted background values and their sum, the ratio between source cell and background counts, and the Poisson probabilities for obtaining the extracted source counts (or higher), assuming only a Poisson signal from the expected background, again for MOS1 and MOS2 separately and their combined probability.

Inspection of Table 2 shows that in five of the six considered energy bands the ratio between source and background counts is very close to unity and that the probabilities of obtaining the observed number of counts are always 0.1 or higher.

However, in the a priori chosen energy band 0.465–0.665 keV an excess is observed both for MOS1 (7 counts observed, 2.5 expected) and MOS2 (10 counts observed, 3.6 expected) and of course for both detectors combined (17 counts observed, 6.1 expected). While the probabilities for obtaining the individual MOS1 and MOS2 counts by chance are already low (0.014 and 0.004, respectively), the combined probability for the assumption of observing background fluctuations both in MOS1 and MOS2, is only 5.7×10^{-5}. This small number combined with the fact that in the other energy bands no significant detections are obtained makes us confident that our background estimates are reliable and that the observed excess in the 0.465–0.665 keV band is real (with a formal statistical confidence of 0.999943) despite the low overall number of recorded counts.

Interpreting the observed 10.9 excess photons as a true source signal, we can convert this number into an energy flux. With an effective area in the considered energy band (465–665 eV) of 86 cm^2 for each of the two detectors, an encircled energy fraction of ~75% for the used source cell regions and the CCD live time of 72 ks, we can calculate the recorded energy flux in the OVII-triplet. While other X-ray lines (e.g. H-like NVII at 500 eV) and continuum emission may contribute to the observed flux, OVII is clearly the major contributor in this energy band, unless extremely unusual abundance patterns are assumed. In this fashion we arrive at an observed energy flux of 6.0×10^{-16} erg/cm^2/s in the OVII triplet; if one were to choose not to interpret these counts as a true source signal or to assume other relevant contributors in this energy band, this number would have to be treated as an upper limit.

2.3. ROSAT HRI results

After carrying out the XMM-Newton observation we analyzed an (apparently) unpublished ROSAT HRI observation of β Pic obtained in February 1996 (ROR number WG202151). Like the EPIC PN image, the ROSAT HRI image shows a clear source at the position of β Pic. Again the source is seen mainly in the lower pulse height channels suggesting a UV origin of the observed signal. Restricting the analysis to HRI pulse height channels 2–8, we find a count rate of 1.41×10^{-3} cts/s. Using a U band magnitude of 4.13 and the ROSAT HRI UV contamination calibration curve derived by Berghöfer et al. (1999) we calculate an expected contaminating ROSAT HRI flux of 4.3×10^{-4} cts/s, which lies considerably below the actually observed value. However, it is obviously quite courageous to interpret the formal excess as a true X-ray signal since the calibration curve by Berghöfer et al. (1999) has been derived from a rather small number of stars.

3. Discussion

3.1. Internal consistency of X-ray results

Accepting the MOS data as a X-ray detection, we derive an observed X-ray count rate of 1.5×10^{-4} cts/s for β Pic. This is clearly inconsistent with the excess with respect to the expected flux from UV contamination as formally derived from the ROSAT HRI data; we therefore conclude that all of the

Table 2. The photons of β Pic. The *a priori* chosen energy band between 0.465 keV and 0.665 keV is centered on the OVII triplet at 21.6 Å/21.8 Å/22.1 Å. Note the significantly different ratio between source and background counts as well as the conspicuously lower probabilities for the assumption of observing background fluctuations in this energy band.

Energy (keV)	Source region			Scaled background			SRC/BG	Probability		
	MOS1	MOS2	Σ	MOS1	MOS2	Σ	Ratio	PPM1	PPM2	PPM1/2
0.2–0.465	4	7	11	3.9	7.0	10.9	1.0	0.55	0.55	0.30
0.465–0.665	7	10	17	2.5	3.6	6.1	2.8	0.014	0.004	5.7×10^{-5}
0.665–1.0	6	2	8	3.5	3.7	7.2	1.1	0.14	0.88	0.13
1.0–2.0	19	11	30	14.3	15.2	29.5	1.0	0.13	0.89	0.12
2.0–5.0	15	9	24	11.9	11.4	23.3	1.0	0.22	0.80	0.18
5.0–12.0	13	16	29	19.1	18.3	37.4	0.8	0.94	0.74	0.69

Table 3. Comparison of O VI and OVII fluxes. The last column contains the X-ray fluxes calculated by Hünsch et al. (1998) (besides AB Dor). All data are given in 10^{-14} erg/cm^2/s. See Sect. 3.2 for details.

Star	HD	Sp.-Type	O VI (1032 Å)	O VII (r+i+f)			f_{x14}
				LETG	MEG	RGS1	
Procyon	61421	F5 IV-V	223 ± 49^a	66 ± 7	–	–	1293.9
α Cen A	128620	G2 V	95.4 ± 9.5^a	21 ± 5	–	–	990.0^c
α Cen B	128621	K1 V	61.6 ± 11.5^a	25 ± 6	–	84 ± 29	990.0^c
AB Dor	36705	K1 III p	44.9 ± 4.5^a	–	32 ± 13	49 ± 7	5100^d
ϵ Eri	22049	K2 V	43.3 ± 4.3^a	71 ± 8	–	64 ± 16	1687.0
AU Mic	197481	M0 V	20.9 ± 2.4^a	–	32 ± 13	67 ± 8	–
Altair	187642	A7 V	82.1 ± 8.2^a	–	–	–	201.3
β Pic	39060	A5 V	5.5^b	–	–	< 0.3	–

[a] Redfield et al. (2002), [b] Deleuil et al. (2001), [c] combined flux of α Cen A and α Cen B,
[d] derived using 7 cts/s (Kürster et al. 1997).

ROSAT HRI data are due to UV contamination from β Pic's photosphere. On the other hand, performing the same procedure for the EPIC PN camera as carried out and described in Sect. 2.2 for the MOS data, we find in the energy band 0.465–0.665 keV a total of 25 source counts where 12 background counts are expected. Considering the different characteristics of the instrument and shorter effective exposure time one expects approximately 16 source counts in the PN detector. The net number of 13 source counts is thus consistent with the total number of counts detected in the two MOS cameras. We note that optical/UV contamination dominates at low energies, and our measurements above 0.665 keV are fully compatible with being background. If one therefore attributes the detected EPIC PN counts below 0.465 keV to optical/UV contamination and the recorded ROSAT HRI counts to UV contamination, all the obtained X-ray measurements are internally consistent.

3.2. Comparison to other cool stars

It is instructive to compare the obtained FUV and X-ray data to those of other cool stars. In Table 3, we list FUSE measurements of the OVI line at 1031.926 Å together with various measurements of the OVII triplet obtained with *Chandra* and XMM-Newton as well as broad band measurements obtained with the ROSAT PSPC. The OVI data are taken from Redfield et al. (2002) and Deleuil et al. (2001). The OVII fluxes were measured by us using CORA (Ness & Wichmann 2002);

for details see Ness et al. (2004). The RGS data are included for completeness only. Since we did not detect a useful RGS signal for β Pic due to the small number of photons, this value has to be considered as an upper limit. The ROSAT measurements are from the compilation by Hünsch et al. (1998); the AB Dor PSPC flux is based on 7 cts/s (Kürster et al. 1997), converted to fluxes using the HEASARC tool PIMMS (0.1–2 keV). We perform this comparison for the inactive stars Procyon, α Cen A and B and the "early" late-type star Altair, as well as the active stars ϵ Eri, AB Dor, and AU Mic. Note that for Altair no high resolution spectroscopic X-ray measurements are available. From Table 3 it is clear that for all stars (possibly except Altair) the OVI and OVII flux is of the same order of magnitude, in contrast to β Pic. This suggests a fundamental difference between the stars with outer convection zones and β Pic.

3.3. A cool corona?

If we attribute the OVI line detection obtained with FUSE and the OVII X-ray detection obtained with XMM-Newton to a stationary corona, we can obtain a temperature and emission measure estimate for such a structure. Using the CHIANTI code (Dere et al. 1997) to compute the flux ratios between the overall OVII triplet (i.e., the sum of resonance, intercombination and forbidden lines) and the OVI doublet (i.e., the sum of the 1032 Å and 1037 Å lines) as a function of temperature, we can compare the measurements for various stars (cf. Table 3) with
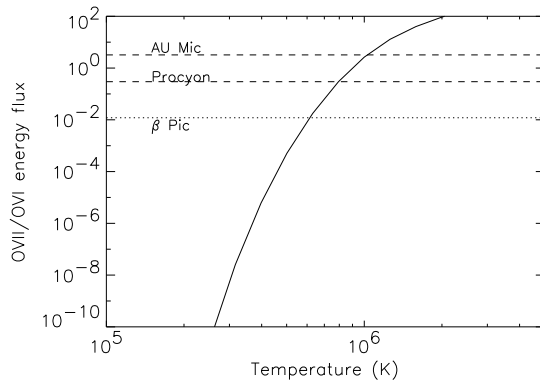
Fig. 2. Flux ratio of the O VII triplet vs. O VI doublet. See Table 3 for the corresponding O VII and O VI fluxes. For β Pic, we used the O VII flux of 6.0×10^{-16} erg/cm^2/s derived in Sect. 2.2.

Fig. 3. Comparison of spectra from β Pic (blue/grey) and Altair (black) obtained from the FUSE archive. The profiles show the C III 977 Å resonance line. Note that despite the significantly lower rotational velocity ($v \sin i_{\beta\,\mathrm{Pic}} = 132$ km s^{-1}, $v \sin i_{\mathrm{Altair}} = 208$ km s^{-1}) the profile of β Pic is at least as broad as Altair's.

Fig. 4. O VI at 1032 Å shows that the profile obtained for β Pic is broader than the one of Altair. As for C III at 977 Å we consider this as an effect from the infalling material.

theoretical expectations in Fig. 2. As is obvious from Fig. 2, the thus derived temperature of $\approx 600\,000$ K is far lower than that of any comparison star. Accepting for the moment this value, we require volume emission measures of $\approx 10^{52}$ cm^{-3} to account for both the FUSE O VI and XMM-Newton O VII measurements. Naturally, these emission measure values depend very sensitively on the adopted temperatures, and choosing higher temperatures leads to significantly lower emission measures. Based on the X-ray detection of Altair (Golub et al. 1983; Schmitt et al. 1985; Freire Ferrero et al. 1995), and regarding the similarity between β Pic and Altair, Bouret et al. (2002) suspected that a warm corona such as that of Altair (Freire Ferrero et al. 1995) can be expected for β Pic as well.

3.4. Comparison of FUSE line profiles

In order to address the issue of whether there is a connection between the FUV and X-ray emissions obtained for the A5V star β Pic and the A7 V star Altair (HR 7557), we retrieved the archival FUSE data analysed by Deleuil et al. (2001) and compared them with spectra of the same lines from Altair[1].

Figures 3 and 4 show the overlaid emission line profiles of C III at 977.020 Å and O VI at 1031.926 Å for both β Pic and Altair, respectively. As can be seen from Figs. 3 and 4, the emission lines from β Pic are clearly broader than those of Altair. This is remarkable since the significantly different projected rotational velocities of both stars would suggest exactly the opposite: while β Pic rotates with $v \sin i_{\beta\,\mathrm{Pic}} = 132$ km s^{-1} (Holweger et al. 1999), Altair apparently rotates much faster with $v \sin i_{\mathrm{Altair}} = 208$ km s^{-1} (Holweger et al. 1999). Therefore one would expect the profiles of Altair to be far broader than those of β Pic. Figures 3 and 4 show the contrary. This strongly suggests that for β Pic an additional line broadening mechanism must exist which exceeds the rotational line broadening and is not present in the otherwise similar star Altair. We note in this context that "suprarotational" line broadening is often encountered in studies of emission lines originating from chromospheres and/or transition regions. For example,

---
[1] Dataset IDs Q1190103000 (β Pic) and P1180701000 (Altair).

Ayres et al. (1997) measured such broadening in their study of moderate-mass giant stars, which, however, are slow rotators compared to the A-stars considered in this paper; their Fig. 9 shows the dependence of the nonthermal broadening on $v \sin i$ for four stars, suggesting a correlation between excess broadening and stellar rotation, and the authors then attribute this broadening to a thick transition zone extending to $h \sim R_\star$. As far as main-sequence stars of earlier spectral type are concerned, Simon & Landsman (1997), using HST GHRS data, and Simon et al. (2002), using FUSE data, describe the emission line profiles of C III $\lambda 977$, O VI $\lambda 1032$, and Si III $\lambda 1206$ from τ^3 Eri, α Cep, and Altair as significantly broader than what one would expect from the $v \sin i$ values, without, however, giving a quantitative analysis. In their FUSE study of β Pic, Bouret et al. (2002) suggest that the suprarotational broadening can be explained in terms of an extended coronal magnetosphere which traps and heats the gas in the co-rotating lobes. If the chromospheric and transition region line broadening in τ^3 Eri is indeed comparable to that observed in Altair as suggested by Simon & Landsman (1997), τ^3 Eri with $v \sin i = 120$ km s^{-1} would in fact be quite similar to β Pic.

While no disk is known around τ^3 Eri, both Ohanesyan (1997) and Song et al. (2001) argue for the presence of a disk around τ^3 Eri, suggesting τ^3 Eri to be "Vega-like" based on IRAS excesses at at 12 μm and 25 μm (rather than at 60 μm).

3.5. A boundary layer?

Are there other origins for the additional line broadening mechanism required to explain the OVI line profile observed in β Pic? Let us recall that material from its circumstellar debris disk is falling onto β Pic with a more or less constant rate. Narrow circumstellar absorption components in the core of the Ca II K line are a well-studied phenomenon: the star shows a seemingly stable central absorption and a *variable* component which may vanish at times. The variability in the core of the Ca II K line on short timescales is attributed to the above mentioned *falling evaporating bodies* (FEB's, Ferlet 1987, see Sect. 1). Petterson & Tobin (1999) carried out a long-term study on the spectral variability of β Pic in Ca II H and K between 1994 and 1996 and inferred event rates of 400 per year for high velocity features (HVF's), while low velocity features are seemingly more stable and may even persist for several nights. In our study of high-resolution spectra ($R \approx 217\,000$) we have detected nightly variations in the Ca II K line of β Pic (Hempel & Schmitt 2003). Brandeker et al. (2004) analyzed the spatial structure of the β Pic gas disk in a distance range from the star from 13 AU out to 323 AU and found 88 spatially resolved emission lines in their UVES spectra. From the velocity shift of the NE and SW side observed in the Na D$_2$ emission they deduced a Keplerian rotation of the outer disk. It is thus clear that the disk around β Pic contains not only debris and dust, but also gas.

Let us therefore hypothesize that β Pic is still an accretion disk now, which it must have been in the very early days of β Pic's existence. Of course, radiation pressure acts – as always – against accretion, however, according to Lagrange et al. (1998, Table 4), the radiation pressure would only prevent some ions, but not the bulk of the material from accretion; also, the source of viscosity, which would be required for angular momentum transport, remains unclear.

Let us first consider the accretion rate necessary to account for the observed high-temperature plasma. Modelling the emitting gas as an isothermal, optically thin gas cloud of temperature T, the FUSE and XMM-Newton observations determine the volume emission measure $VEM = n_e^2 \times V$. The emitting volume V is assumed to have a height h much smaller than the stellar radius R, so that $V = 4\pi R^2 hf$, where f is the unknown filling factor of the accreting material. The hot gas is assumed to predominantly cool through radiation, and the radiative cooling time scale τ_{rad} is given by $\tau_{rad} = \frac{3kT}{2n_e P(T)}$, where $P(T)$ denotes the radiative cooling function of the plasma as a whole. As the gas cools, it is accreted and settles onto the star. Assuming explicitly that radiative cooling is the dominant energy loss mechanism, the radial accretion velocity v_{rad} is given by $v_{rad} = \frac{h}{\tau_{rad}}$. The overall mass accretion rate then becomes $\dot{M}_{acc} = 4\pi R^2 f \rho v_{rad}$, where ρ denotes the density of the X-ray emitting layers. Since $\rho = \mu m_H n_e$, we finally obtain
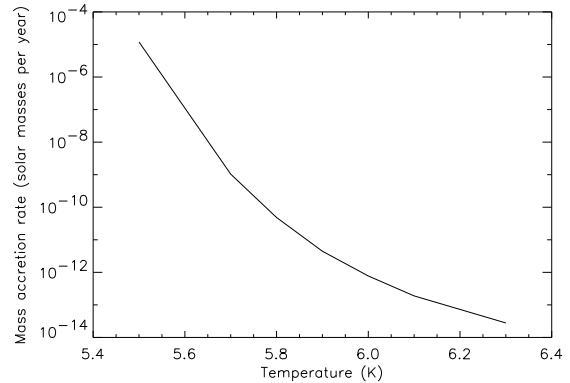
Fig. 5. Mass accretion rates vs. temperature. See Sect. 3.5 for details.

$\dot{M}_{acc} = \frac{8\pi f R^2 \mu m_H n_e h n_e P(T)}{3kT} = \frac{2VEM\mu m_H P(T)}{3kT}$, i.e., an expression that depends only on measured or (more or less) known quantities. Unfortunately, the emission measure VEM, derived from the UV and X-ray data, depends very sensitively on the adopted temperature, and also, the plasma cooling function $P(T)$ depends on temperature and on the elemental abundances in the hypothesized accretion stream. In particular the latter may be far from the cosmic abundance and in fact only oxygen is observed. With the above formulae and the observed VEM we can compute $\dot{M}_{acc}$ as a function of temperature (see Fig. 5) assuming cosmic abundances (Holweger 2001), an ideal gas, and a plasma cooling function $P(T)$ as computed with the CHIANTI package (Dere et al. 1997). Since temperatures between $5.8 < \log T < 6.0$ are the most likely ones, we conclude that accretion rates between 10^{-10}–10^{-12} $M_\odot$ yr^{-1} would be required to explain the observed emissions via a boundary layer. Assuming reasonable values for β Pic's mass, radius, and luminosity, $M = 1.75\,M_\odot$, $R = 1.53\,R_\odot$, $\log(L/L_\odot) = 0.95$ (Di Folco et al. 2004), the resulting accretion luminosities $L_{acc} = \frac{G\dot{M}_{acc}M}{R}$ would then be in the range of 10^{31}–10^{29} erg/s, i.e., only a fraction of 10^{-3}–10^{-5} of β Pic's luminosity and therefore very difficult to detect. Holweger et al. (1997) have performed a detailed abundance analysis of β Pic and found it to be consistent with solar abundance; this result would exclude mass accretion rates $>10^{-13}$ $M_\odot$ yr^{-1} consisting of material with depleted elemental abundances, while material with solar-like abundances could be accreted at much higher rates. King & Patten (1992) analyzed accretion scenarios in β Pic in the context of the λ Boo phenomenon and estimated $1.5 \times 10^{-19} \leq \dot{M}_{FEB} \leq 2 \times 10^{-14}$ $M_\odot$ yr^{-1} for the accretion due to FEBs and $7.5 \times 10^{-19} \leq \dot{M}_{CS} \leq 6 \times 10^{-10}$ $M_\odot$ yr^{-1} for an accretion of CS material onto β Pic. Unaffected by the fact that a metal-deficiency of β Pic could not be established in an abundance analysis (Holweger et al. 1997, see also Gerbaldi et al. 1993) and thus the λ Boo nature of β Pic could not be confirmed, the estimated accretion rate is consistent with our values and we therefore conclude that at present there are no strong arguments against an accretion onto β Pic with mass accretion rates in the range 10^{-10}–10^{-12} $M_\odot$ yr^{-1}.

How is the accretion disk material actually accreted onto the star? This may occur by free fall from some inner truncation

radius of the disk resulting in velocities of up to $400\,\mathrm{km\,s^{-1}}$, which are in fact obtained and observed for FEBs. However, line broadening of $400\,\mathrm{km\,s^{-1}}$ is certainly larger than what is required to explain the broadening observed in the FUSE spectra. Alternatively, we may assume a Keplerian disk reaching down almost to the stellar surface and releasing its energy in a narrow boundary layer. Assuming reasonable values for β Pic's mass and radius, $M = 1.75\,M_\odot$ and $R = 1.53\,R_\odot$ (Di Folco et al. 2004), we calculate a Keplerian velocity of $v_{\mathrm{K}} \approx 470\,\mathrm{km\,s^{-1}}$ directly at its surface. On the other hand, since the inclination angle is very close to $90°$, we expect an equatorial rotation velocity $v_{\mathrm{eq}} \approx 132\,\mathrm{km\,s^{-1}}$ (Holweger et al. 1999). The kinetic energy contained in this velocity difference $\Delta V = v_{\mathrm{K}} - v_{\mathrm{eq}} \approx 340\,\mathrm{km\,s^{-1}}$ is available for dissipation and the value of ΔV should be a strict upper limit for the additionally occurring line broadening.

The kinetic energy of the incoming material is dissipated in a thin turbulent boundary layer. Applying the turbulent Crocco-Busemann relations (White 1991) we find the following relation between boundary layer temperature T and velocity u:

$$T = T_{\mathrm{photo}} + \left(T_{\mathrm{acc}} + \frac{\Delta V^2}{2c_{\mathrm{p}}}\right)\frac{u}{\Delta V} - \frac{u^2}{2c_{\mathrm{p}}};\qquad(1)$$

here T_{photo} and T_{acc} denote the temperatures of the photosphere and accretion disk respectively, ΔV the velocity difference between surface and Keplerian velocity and c_{p} the specific heat. In Fig. 6 we plot the temperature vs. velocity for accreting material onto β Pic in a boundary layer. It can be seen that a maximum of about $T_{\mathrm{max}} \approx 3.5 \times 10^5\,\mathrm{K}$ is reached for material accreting with $v \approx 170\,\mathrm{km\,s^{-1}}$. A temperature of about $350\,000\,\mathrm{K}$, in turn, corresponds to the line formation temperature of the observed emissions of CIII and O VI. At face value this is a factor of two lower, but considering the simplicity of the model the hypothesis of accretion of circumstellar material in a boundary layer is at least in principle capable of explaining the presence of CIII and O VI and the weakness of O VII *without the ad hoc assumption of a chromosphere*. For a more sophisticated model, detailed hydrodynamical calculations would be needed. Note that this scenario is also applicable to explain the additional broadening mechanism of the observed CIII and O VI emissions.

3.6. Implications for disk models

We compared β Pic's broadened highly ionized resonance lines of C III and O VI analyzed by Deleuil et al. (2001) to the same lines of Altair. Our results show that the emission from the CIII and OVI lines are significantly broadened compared to the otherwise similar star Altair. Furthermore, we found X-ray emission from β Pic in the OVII triplet at $21.6\,\mathrm{\AA}$. We have shown that our findings are consistent with the existence of either a cool corona or with the accretion of circumstellar material in a boundary layer without the ad hoc assumption of a chromosphere. These results present a challenge for the development of stellar/coronal models but one further point compared to, e.g. the active A7 V star Altair, is important especially for the case of β Pic: the star harbours a well-known circumstellar debris disk with a diameter of approximately 1000 AU. Thus β Pic
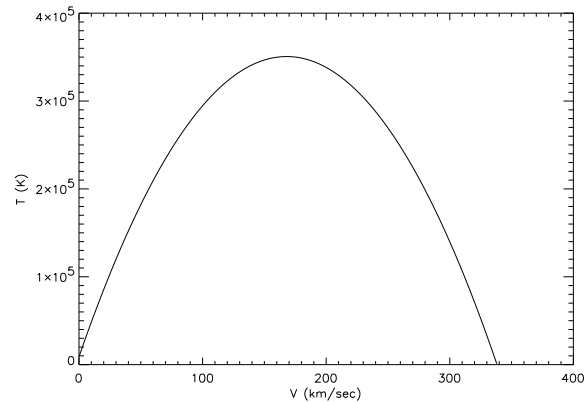
Fig. 6. Temperature of accreted material in a boundary layer according to the turbulent Crocco-Busemann relations (White 1991); see Sect. 3.5 and Eq. (1) for details. For infalling material with $v \approx 170\,\mathrm{km\,s^{-1}}$ we find a temperature of about $350\,000\,\mathrm{K}$ which is sufficient for the formation of CIII and OVI.

serves as a prototype: one important result of the IRAS and ISO missions is the detection of many IR-excess stars with CS disks and rings of gas and dust. One vital question still under debate is how to determine the masses of these disks. CS disk masses are an important ingredient in assessing the formation process of planets – either via core-accretion or gravitational instabilities. Therefore it is mandatory to develop models to describe the chemical structure of CS disks. So far, such models have often neglected the existence of chromospheres – even in the case of late-type stars. Nevertheless, it is known that the stellar radiation field drives the chemistry in CS disks and that the solar ultraviolet ionizing flux weakens with time. Thus the influence of the stellar UV field on CS disks is expected to be greater for younger stars. One attempt to include the chromosphere of late-type stars has been made by Kamp & Sammar (2004), who studied the influence of the chromosphere of a G5 star on the chemistry in the late phases of disk evolution. Their calculations show that in the inner disk ($\lesssim 400\,\mathrm{AU}$) the chromospheric UV emission is the driving mechanism in chemistry and that differences in the H and CO abundances by more than a factor of 10 occur if one neglects the presence of a chromosphere. Given the fact that highly ionized species were detected in the FUSE spectra of β Pic, these processes may also have a pronounced effect on its disk chemistry. Since the calculations by Kamp & Sammar (2004) were carried out for a G star, it would be desirable to extend the disk models to A-type stars. The model by Kamp & Sammar (2004) does not consider an X-ray flux. Although the nature of the detected X-ray emission from β Pic is not fully clear yet it is most likely that the X-ray flux will not be of major importance for the disk chemistry of β Pic. Alexander et al. (2004) studied the effects of X-ray ionization and heating on the stucture of CS disks around low-mass stars. Using parameters of typical T Tauri stars, they find that photo-evaporation does not play a significant role in the evolution of CS disks. Given the fact that the X-ray flux from β Pic is very low, we expect that this is also valid for β Pic.

4. Conclusions

We have detected X-ray emission of the A5 V star β Pic in a 73 ks observation with XMM-Newton. Despite the low number of photons, a thorough statistical analysis makes us confident that the observed excess in the OVII triplet is actually real with a flux level of 6.0×10^{-16} erg/cm^2/s. We discuss the detected X-ray emission in view of (i) the existence of a cool corona and (ii) accretion of circumstellar material in a boundary layer.

The main results of this work can be summarized as follows:

(1) β Pic shows weak emission in the OVII triplet at 21.6 Å. We derive an energy flux of 6.0×10^{-16} erg/cm^2/s in the OVII triplet. To our knowledge this is the first detection of X-rays from β Pic.

(2) The OVII detection is consistent with a cool corona with $T \approx 600\,000$ K.

(3) β Pic exhibits highly ionized species typical of a transition region (Deleuil et al. 2001). The emission from the CIII and OVI lines are significantly broadened compared to the otherwise similar star Altair.

(4) Material is accreted on β Pic with (as measured for FEBs) velocities up to $400\,\mathrm{km\,s^{-1}}$. This might account for the additional broadening of the CIII and OVI emission lines.

(5) Accretion in a boundary layer appears to be capable of explaining the observed UV lines of CIII and OVI and the weakness of O VII.

References

Alexander, R. D., Clarke, C. J., & Pringle, J. E. 2004, MNRAS, 354, 71

Ayres, T. R., Simon, T., Stern, R. A., et al. 1998, ApJ, 496, 428

Berghöfer, T. W., Schmitt, J. H. M. M., & Hünsch, M. 1999, A&A, 342, L17

Brandeker, A., Liseau, R., Olofsson, G., & Fridlund, M. 2004, A&A, 413, 681

Bouret, J.-C., Deleuil, M., Lanz, T., et al. 2002, A&A, 390, 1049

Chen, C. H., & Kamp, I. 2004, ApJ, 602, 985

Christensen-Dalsgaard, J. 2000, ed. M. Breger, & M. Montgomery, San Francisco, ASP Conf. Ser., 210, 187

Chung, S.M., Drake, J. J., Kashyap, V. L., et al. 2004, ApJ, 606, 1184

Deleuil, M., Bouret, J.-C., Lecavelier des Etangs, A., et al. 2001, ApJ, 557, L67

Dere, K. P., Landi, E., Mason, H. E., et al. 1997, A&AS, 125, 149

Di Folco, E., Thévenin, F., Kervella, P., et al. 2004, A&A, 426, 601

Ehle, M., Breitfellner, M., Gonzales Riestra, M., et al. 2003, XMM-Newton User's Handbook

Ferlet, R., Vidal-Madjar, A., & Hobbs, L. M. 1987, A&A, 185, 267

Freire Ferrero, R., Gouttebroze, P., Catalano, S., et al. 1995, ApJ, 439, 1011

Freytag, B., Ludwig, H. G., & Steffen, M. 1996, A&A, 313, 497

Gerbaldi, M., Zorec, J., Castelli, F., & Faraggiana, R. 1993, ASP Conf., 44, 413

Golub, L., Harnden, F. R., Jr., Maxson, C. W., et al. 1983, ApJ, 271, 264

Holweger, H. 2001, in Solar and Galactic Composition, A Joint SOHO/ACE Workshop, ed. R. F. Wimmer-Schweingruber, AIP Conf. Proc., 598, 23

Holweger, H., Hempel, M., van Thiel, T., & Kaufer, A. 1997, A&A, 320, L49

Holweger, H., Hempel, M., & Kamp, I. 1999, A&A, 350, 603

Hempel, M., & Schmitt, J. H. M. M. 2003, A&A, 408, 971

Hünsch, M., Schmitt, J. H. M. M., Voges, W. 1998, A&AS, 132, 155

Hünsch, M., Schmitt, J. H. M. M., Sterzik, M. F., & Voges, W. 1999, A&AS, 135, 319

Kamp, I., van Zadelhoff, G.-J., van Dishoeck, E. F., & Stark, R. 2003, A&A, 397, 1129

Kamp, I., & Sammar, F. 2004, A&A, 427, 561

King, J. R., & Patten, B. M. 1992, MNRAS, 256, 571

Kürster, M., Schmitt, J. H. M. M., Cutispoto, G., & Dennerl, K. 1997, A&A, 320, 831

Kupka, F., & Montgomery, M. H. 2002, MNRAS, 330, L6

Lagrange, A.-M., Beust, H., Mouillet, D., et al. 1998, A&A, 330, 1091

Ness, J.-U., & Wichmann, R. 2002, AN, 323, 129

Ness, J.-U., Güdel, M., Schmitt, J. H. M. M., et al. 2004, A&A, 427, 667

Ness, J.-U., Schmitt, J. H. M. M., & Robrade, J. 2004, A&A, 414, L49

Ohanesyan, J. B. 1997, Astrophysics, 40, 237

Petterson, O. K. L., & Tobin, W. 1999, MNRAS, 304, 733

Redfield, S., Linsky, J. L., Ake, T. B., et al. 2002, ApJ, 581, 626

Schmitt, J. H. M. M., Golub, L., Harnden, F. R., et al. 1985, ApJ, 290, 307

Schmitt, J. H. M. M., Micela, G., Sciortino, S., et al. 1990, ApJ, 351, 492

Schmitt, J. H. M. M., & Kürster, M. 1993, Science, 262, 215

Schmitt, J. H. M. M., & Liefke, C. 2004, A&A, 417, 651

Schneider, G., Smith, B. A., Becklin, E. E., et al. 1999, ApJ, 513, L127

Simon, T., Ayres, T. R., Redfield, S., & Linsky, J. L. 2002, ApJ, 579, 800

Simon, T., & Landsman, W. B. 1997, ApJ, 483, 435

Smith, B. A., & Terrile, R. J. 1984, Science, 226, 1421

Song, I., Caillault, J.-P., Barrado y Navascués, D., & Stauffer, J. R. 2001, ApJ, 546, 352

White, F. M. 1991, Viscous Fluid Flow (McGraw-Hill International Editions)

Chapter 7

X-rays from α Centauri – The darkening of the solar twin

J. Robrade, J. H. M. M. Schmitt and F. Favata
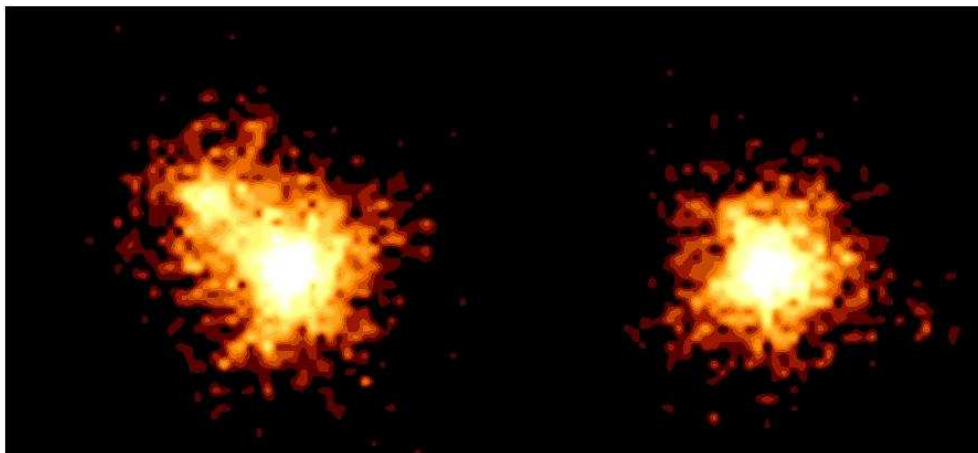
X-rays from Alpha Centauri - The darkening of the solar twin

Image courtesy of Robrade, Jan

European Space Agency

Figure 7.1: Accompanying image of the Alpha Centauri system obtained in March 2003 and Febuary 2005 with MOS1 and released in the XMM-Newton image gallery.

**Astronomy
&
Astrophysics**

X-rays from α Centauri – The darkening of the solar twin

J. Robrade[1], J. H. M. M. Schmitt[1], and F. Favata[2]

[1] Hamburger Sternwarte, Universität Hamburg, Gojenbergsweg 112, 21029 Hamburg, Germany
    e-mail: jrobrade@hs.uni-hamburg.de
[2] Astrophysics Division – Research and Science Support Department of ESA, ESTEC, Postbus 299, 2200 AG, Noordwijk, The Netherlands

ABSTRACT

We present first results from five XMM-Newton observations of the binary system α Centauri, which has been observed in snapshot like exposures of roughly two hours each during the last two years. In all our observations the X-ray emission of the system is dominated by α Cen B, a K1 star. The derived light curves of the individual components reveal variability on short timescales and a flare was discovered on α Cen B during one observation. A PSF fitting algorithm is applied to the event distribution to determine the brightness of each component during the observations. We perform a spectral analysis with multi-temperature models to calculate the X-ray luminosities. We investigate long term variability and possible activity cycles of both stars and find the optically brighter component α Cen A, a G2 star very similar to our Sun, to have fainted in X-rays by at least an order of magnitude during the observation program, a behaviour never observed before on α Cen A, but rather similar to the X-ray behaviour observed with XMM-Newton on HD 81809. We also compare our data with earlier spatially resolved observations performed over the last 25 years.

Key words. stars: activity – stars: coronae – stars: flare – stars: late-type – X-rays: stars

1. Introduction

The visual binary system α Centauri AB (HD 128620/1) is the nearest stellar system consisting of a G2V (A) and a K1V (B) star at a distance of 1.3 pc; in addition, the M dwarf Proxima Centauri is in common proper motion with the α Cen A/B system. The two components α Cen A and B are separated by roughly 25 AU, with an orbital period of 80 years. The age of the system is thought to be slightly larger than that of the Sun, correspondingly both stars are also slow rotators (periods are 29 (A) and 42 (B) days) with a rather inactive corona. References and further literature can be found in Raassen et al. (2003), who analyzed *Chandra* LETGS data from α Cen and in Pagano et al. (2004), who analysed UV data using HST/STIS. The latter authors determined an emission measure distribution of α Cen A from UV to X-rays measurements and found it to be comparable to the quiet Sun, making the slightly more massive star α Cen A a nearly perfect solar twin. This finding immediately raises the question, whether an activity cycle as observed on the Sun, is also present on α Cen. While long-term measurements of chromospheric activity have been performed for several decades (Baliunas et al. 1995), clear indications for X-ray, i.e. coronal, activity cycles on other stars than the Sun were only recently found on a few objects.

Hempelmann et al. (2003) analysed a time series of 4.5 years of ROSAT HRI data, taken at intervals of typically 6 months, on the stars 61 Cyg A and B with well determined chromospheric cycles of 7 and 12 years respectively, and find

that coronal cycles are the dominant source of long-term X-ray variability for both stars. 61 Cyg was monitored also with XMM-Newton over the last years and results of these observations will be presented in a forthcoming paper. Similarly, Favata et al. (2004) obtained a time series of 2.5 years of XMM-Newton data, again obtained at 6 month intervals, of the G star HD 81809, which has a pronounced cycle of 8.2 years, and find clear evidence for large amplitude X-ray variability in phase with the known (chromospheric) activity cycle.

The α Cen system has been studied before in X-rays with several missions, e.g. *Einstein*, ROSAT, ASCA and recently *Chandra*. The two components were already spatially separated with *Einstein* (Golub et al. 1982). The K star was found to dominate the X-ray emission and is usually a factor 2–3 brighter than the G star at typical energies above 0.2 keV in previous observations. In two ROSAT HRI monitoring campaigns, performed in 1996 with nearly daily measurement for a month each, light curves for the individual components were obtained and indications for flaring and a decrease in X-ray brightness of 30% over 20 days, which could be due to rotational modulation, were found on α Cen B (Schmitt & Liefke 2004). Separate high resolution spectra were first obtained with the *Chandra* LETGS (Raassen et al. 2003), which revealed solar like properties for both stars, e.g. the FIP effect and an emission measure distribution dominated by cool plasma with temperatures of 1–3 MK. The K star was found to be slightly hotter and dominates the emission measure above 1.5 MK, while at lower temperatures the G star is the stronger component.

In order to study possible coronal activity cycles of solar-like stars we initiated a long-term monitoring program of a small number of objects and first results on HD 81809 were presented by Favata et al. (2004). Within the context of this ongoing monitoring program the α Cen system was repeatedly observed with XMM-Newton, and here we report first results on the α Cen system. In Sect. 2 we describe the observations and the methods used for data analysis. In Sect. 3 we present the results subdivided into different physical topics, in Sect. 4 we discuss the findings in comparison with previous observations followed by our conclusions in Sect. 5.

2. Observations and data analysis

The target α Cen was repeatedly observed with XMM-Newton using almost identical detector setups and with exposure times in the range of 5–9 ks. We present data from five observations separated by roughly half a year each, which allows us to study short time behaviour during individual exposures as well as long term variations on timescales of several month up to years. Useful data were collected in all X-ray detectors, which were operated simultaneously onboard XMM-Newton, respectively the EPIC (European Photon Imaging Camera), consisting of the MOS and PN detectors and the RGS (Reflection Grating Spectrometer). The MOS and PN observations were performed in the small and large window mode with the thick filter. The OM (Optical Monitor) was blocked due to the brightness of the target.

A description of the observations is provided in Table 1 and a detailed description of the XMM-Newton instruments can be found in Ehle et al. (2003).

The data were reduced with the standard XMM-Newton Science Analysis System (SAS) software, version 6.0. Images, light curves and spectra were produced with standard SAS tools and standard selection criteria were applied for filtering the data, see Ehle et al. (2004). Spectral analysis was carried out with XSPEC V11.3 (Arnaud 1996).

For imaging we use data taken with the MOS1 detector, which has a more spherical symmetric PSF shape compared to MOS2 and a better spatial resolution than the PN detector. Spectral analysis of EPIC data is performed in the energy band between 0.2–5.0 keV, but sufficient signal is mostly present only up to ~2 keV. For the RGS first order spectra in the full energy range, i.e. 0.35–2.5 keV (5–35 Å), are used. While the RGS has the highest spectral resolution, the EPIC detectors are able to measure higher energy X-rays with higher sensitivity, with the MOS detectors providing a slightly better spectral resolution and the PN detector providing greater sensitivity. Data of the same detector type, i.e. RGS1 and RGS2 and MOS1 and

MOS2, were analyzed simultaneously but not co-added. Data quality is generally good, only the MOS2 data of the July 04 observation are corrupted and had to be discarded from further analysis. The background was taken from source free regions on the detectors. Our fit procedure is based on χ^2 minimization, therefore spectra are rebinned to satisfy the statistical demand of a minimum value of 15 counts per spectral bin.

For the analysis of the X-ray spectra we use multi-temperature models with variable but tied abundances, i.e. the same abundance pattern in all temperature components. Such models assume the emission spectrum of a collisionally-ionized optically-thin gas as calculated with the APEC code, see e.g. Smith et al. (2001). Abundances are calculated relative to solar photospheric values as given by Anders & Grevesse (1989). For iron and oxygen we use the values of Grevesse & Sauval (1998). The applied model uses two temperature components, models with additional temperature components were checked, but did not improve the fit results significantly. Due to the lower spectral resolution of the EPIC detectors, for those elements where features are most prominent only in the RGS, the RGS values were taken, for elements without clearly recognizable lines, e.g. Al, Ca, Ni, solar values were used. X-ray luminosities were then calculated from the resulting best fit models. Due to the proximity of the stars absorption in the interstellar medium is negligible at the wavelengths of interest and was not applied in our modelling.

3. Results

3.1. Investigation of images and light curves

In Fig. 1 we show two images of the system taken with the MOS1 detector during the first (March 03) and last (Feb. 05) exposure of our data sample. Significant changes in the luminosity of the components are obvious, especially the strong dimming of α Cen A. To investigate these changes we use individual light curves and a PSF fitting algorithm, which is applied to the event distribution in the sky plane.

The MOS1 light curves of α Cen A and α Cen B for the five observations, separated roughly half a year each, are shown in Fig. 2. The light curves were extracted from a circle with 5″ radius around the respective position of the sources, the temporal binning is 600/180 s for the A/B component. For α Cen A the measured count rate in a region mirrored at the position of α Cen B is subtracted to account for contamination through the much brighter B component; further background contributions are negligible. It is obvious that α Cen B is always the brighter X-ray source, but the count ratio A/B differs significantly. Looking at the individual light curves, α Cen A is mainly constant, only in March 03 a steady decline is visible throughout the observation. α Cen B exhibits short time variability in all observations and a small flare occurred during the Jan. 04 exposure. The mean count rate of α Cen B is comparable during the first three observations, roughly 50% lower in the fourth one and has nearly recovered in the Feb. 05 exposure, while α Cen A has declined by more than an order of magnitude over the two years.

To quantify the individual count rates more precisely, we fitted two instrumental PSFs to the event distribution in the

Table 1. Observation log of α Cen, MOS1

Obs. ID	Obs. Mode	Obs. Time	Dur. (s)
0045340901	SW/thick	2003-03-04T13:50-15:47	6850
0045341001	SW/thick	2003-09-15T14:55-17:04	7560
0045341101	SW/thick	2004-01-29T14:16-15:45	5160
0045340401	SW/thick	2004-07-29T03:48-05:59	7660
0143630501	LW/thick	2005-02-02T14:47-17:13	8770
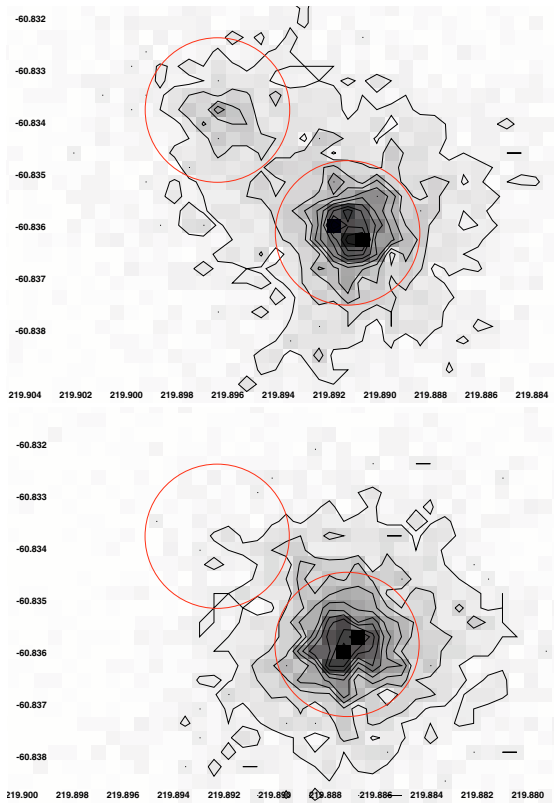
Fig. 1. Image of the system obtained with MOS1 during the March 03 (*top*) and February 05 (*bottom*) exposure with contours and used extraction regions (red) for the two components overlayed. Image creation is identical and the counts per image are very similar, the darkening of the α Cen A component at the upper left is striking.

Table 2. PSF fit results. Poissonian errors are calculated for the derived ratio.

Obs.	Mar. 03	Sept. 03	Jan. 04	July 04	Feb. 05
Live-time(s)	6646	7315	4952	7423	8661
Cts (total)	6152	5775	4690	3477	5759
Cts (αCenB)	4806	5392	4161	3272	5694
Cts (αCenA)	1346	383	529	205	76
Ratio B/A	3.6 ± 0.1	14.1 ± 0.8	7.9 ± 0.4	16.0 ± 1.2	75.0 ± 10.0

sky-plane taken from a 50×50″ box around the position of α Cen following the procedure described by Robrade et al. (2004). After adjusting the PSF shape we kept these fixed, fitted the position of the sources and derived the counts for each of the two components. Small variations of the position were allowed to account for the small proper motion and the two components are detected in all observations very close to their calculated positions, only for the February 05 observation the position of the α Cen A had to be fixed because of the weakness of the source at that time. For this most critical observation we derive values for the count ratio B/A in the range 65–85, depending on the exact position of the sources. This error is of the same magnitude as if assuming Poissonian errors for the derived counts of each source.
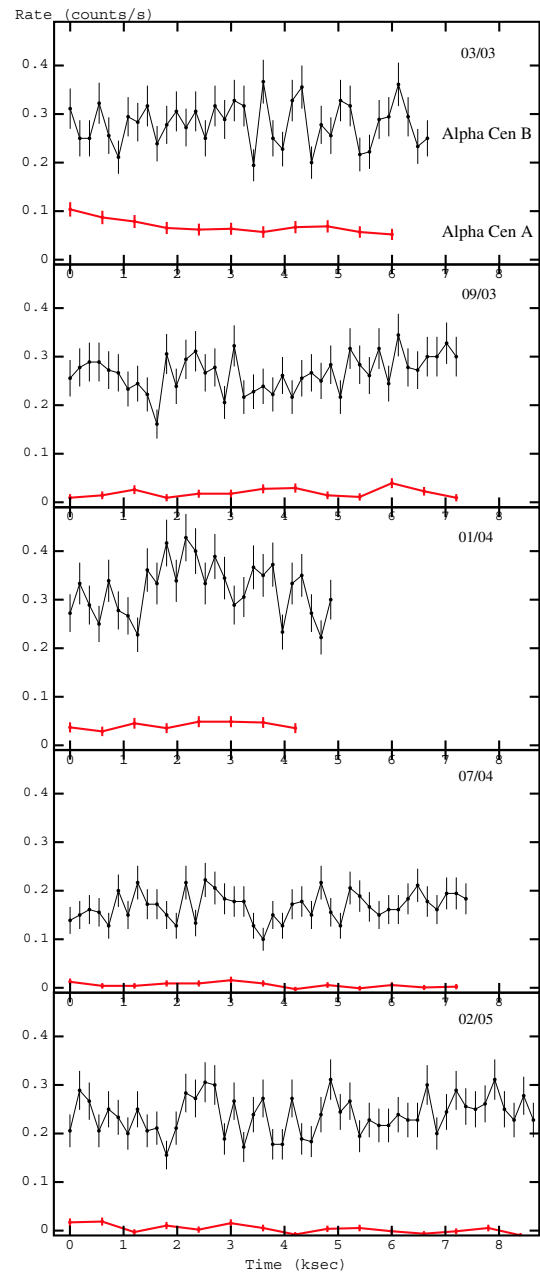
Fig. 2. Light curves of α Cen A/B (red/black) in chronological order as extracted from MOS1 data with 10/3 min binning. The plot sizes are identical for all observations to allow better comparison.

Results of the PSF fitting procedure are presented in Table 2 and are also in good agreement with estimates made from the individual light curves derived above. While α Cen B exhibits a slowly varying brightness, only in July 04 it was significantly darker compared to the other observations, α Cen A is mainly fading away throughout the campaign.

3.2. Spectral analysis

Due to the low signal to noise of the data from the individual observations we modelled the data from the five observations simultaneously, i.e. we neglect possible changes in the elemental abundances, while keeping only the temperatures and emission measures as free parameters to account for the different flux levels and possible coronal heating due to flaring. Because of overlapping PSFs for the individual components, the spectral analysis is performed on the α Cen system as a whole. However, individual fits of spectra taken from small extraction regions around the respective component lead to comparable results for both components. In this work the spectral models are primarily used to determine the X-ray flux for the individual sources. We find that the derived fluxes and therefore luminosities vary only moderately within the different applied models, introducing only a small effect compared to differences arising from calibration uncertainties of the different detectors and errors on the derived count rates.

The RGS spectrum shown in Fig. 3 is dominated by emission lines with no strong continuum visible. The most prominent features are labeled. These lines are formed at relatively cool temperatures, plasma with temperatures in the range of 1–4 MK provides here the dominant contributions to line formation.

The PN spectra of two selected observations are shown in Fig. 4. At energies above 1.0 keV the here non-resolved He-like triplets of magnesium (at 1.35 keV) and silicon (at 1.85 keV) are visible, representing the "hottest" features in the spectra of these stars. The Mg XI and Si XIII lines form at temperatures of 6–10 MK and are more prominent during the brighter exposures or during flaring. Overall spectral changes are also a little more pronounced at higher energies. However, the general spectral shape is very similar for the exposures despite the different flux levels and the different contributions of α Cen A to the flux of the system.

To determine the spectral properties and to calculate the X-ray luminosities of the components, we fitted the spectra of different instruments with multi-temperature spectral models as described in Sect. 2. We find a two temperature fit to be sufficient, only during the flare-observation the model improves with a third hotter (8–10 MK) component, which contributes around 1–2 % to the emission measure of the α Cen system. Since we are not able to clearly separate the spectra of the

Fig. 4. Spectra of the α Cen system obtained with the PN detector: 03/03 (black/top), 07/04 (red/bottom). Despite the different contributions from each component and absolute luminosities, both spectra are very similar and soften only slightly with decreasing flux.

Table 3. X-ray luminosity in 10^{27} erg/s of the α Centauri system in the 0.2–2.0 keV band as derived with the different detectors, for the MOS also separated into three energy bands (low: 0.2–0.5, medium: 0.5–0.75, high: 0.75–2.0 keV).

Obs.date	L_X – MOS – (low/med./high)	RGS	PN
Mar. 03	2.47 – (1.42/0.64/0.42)	2.30	2.86
Sept. 03	2.17 – (1.27/0.55/0.35)	2.02	2.60
Jan. 04	2.52 – (1.41/0.64/0.47)	2.37	2.86
July 04	1.31 – (0.79/0.32/0.19)	1.19	1.79
Feb. 05	1.86 – (1.11/0.47/0.28)	1.62	2.25

individual components and α Cen B is the far brighter X-ray source, we consider all spectral results presented here strongly dominated by α Cen B, especially for the later observations where α Cen A has darkened. A spatially resolved spectral analysis of the two components using data of the *Chandra* LETGS (Raassen et al. 2003), where the sources are clearly separated due to the better spatial resolution, revealed solar like properties for both stars with a slightly hotter corona to be present in α Cen B. Although a detailed spectral analysis is beyond the scope of this work, we would like to point out that consistent results were obtained within our modelling. All X-ray luminosities are given in the 0.2–2.0 keV band unless otherwise indicated.

In Table 3 we show the derived X-ray luminosities of the α Centauri system. The derived fluxes for the individual instruments onboard of XMM-Newton differ slightly, with the MOS results taking an intermediate place between RGS and PN. The PN models predict higher fluxes, especially at lower energies. The subdivision of the MOS results into three energy band exhibits that flux changes are strongest above 0.75 keV and they become more pronounced at even higher energies; but since there is actually not much emission at these energies, the decline in X-ray brightness has to be attributed mainly to a decrease of the emission measure instead of a cooling. This is also reflected by the average coronal temperatures, which are around 2.8 MK and differ only by 0.1 MK between the different exposures.

Fig. 3. The RGS spectrum of the Feb. 05 exposure, an almost pure spectrum of α Cen B.

3.3. A flare on the K star

The individual MOS1 light curves shown in Fig. 2 clearly identify α Cen B as the flaring star in the January 2004 observation, which confirms the nature of the K star as a flare star, as already suggested by Schmitt & Liefke (2004). Due to the greater sensitivity we use the PN data of the total system to investigate details of the flare. The luminosity of α Cen A is much lower than that of α Cen B and is nearly constant over the whole exposure; it therefore induces only an offset on the light curves.

The PN light curves from this observation of the system in two energy bands (medium: 0.5–0.75 keV, hard: 0.75–5.0 keV) are shown in Fig. 5. In the soft band, i.e. below 0.5 keV, the flare is hardly visible. Overlayed on the hard band is a simple exponential flare model of the form $c(t) = C_0 + A \exp^{(-t/\tau)}, t > 0$ with an exponential decay time of $\tau = 900$ s. The flare is much more pronounced in the hard band, a typical behaviour of stellar flares. Using the average energy per photon as derived from the spectral models in Sect. 3.2 we calculate the energy released by this flare event and we derive a total flare energy release of $\sim 5 \times 10^{29}$ erg above 0.5 keV with 60% percent measured in the hard and 40% percent in the medium band. Therefore this flare is comparable to a typical solar flare, where the energy release is in the order of 10^{29} erg while the largest solar flares release up to 10^{32} erg.
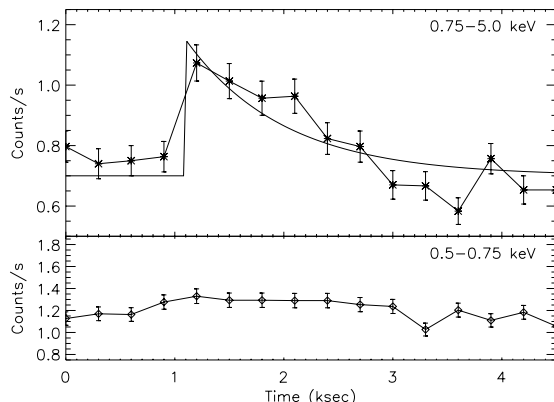
Fig. 5. Light curve of the system in two energy bands with the flare on α Cen B that occurred on January, 29, 2004, PN data with 300 s binning. Overlayed on the hard band is a flare model assuming an exponential decay.

3.4. Long term behaviour

In Fig. 6 we show the calculated 0.2–2.0 keV X-ray luminosities of α Cen A and B as derived from spectral models applied to MOS1 data combined with the results from the PSF fitting procedure; the numerical values are given in Table 4. In this context it is important to note that individual fluxes are calculated from the measured counts of the individual components with a model derived for the sum of both components. In the considered energy band the average energy per photon is slightly lower for the G star, so especially in case of
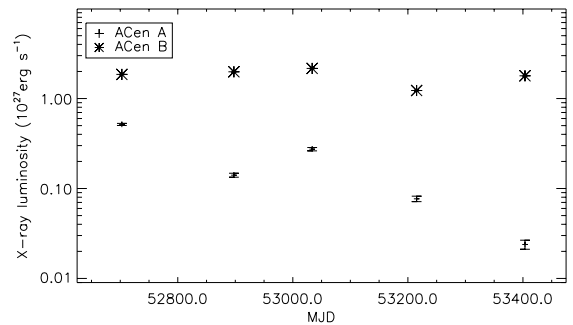
Fig. 6. Long term light curve of α Cen A and B for the five XMM-Newton observations. Errors are Poissonian errors on the derived counts only.

Table 4. Derived X-ray luminosity in 10^{27} erg/s for the two components α Cen A and B from MOS1 data.

Obs.	Mar. 03	Sep. 03	Jan. 04	July 04	Feb. 05
L_X (A)	0.52	0.14	0.27	0.08	0.02
L_X (B)	1.86	1.98	2.16	1.22	1.79

activity on α Cen B the flux of α Cen A may actually be somewhat overestimated.

The X-ray emission of α Cen B is variable within a factor of two also in the absence of stronger flares. However, there is no strong trend visible over the whole observation campaign, only the July 04 observation stands out, exhibiting the lowest X-ray luminosity for α Cen B. The most remarkable result is that α Cen A, a nearly solar twin, is found to be strongly variable by a factor of 10–20. Such a behaviour has to our knowledge never been observed before on this star.

4. Discussion

Although X-ray luminosities are subject to the usual calibration uncertainties of different instruments and although flux ratios do depend on the selected energy range, we are able to compare our measurements with X-ray data taken over the last 25 years. Since the X-ray spectra of both components decline very steeply towards higher energies, there is very little flux above 2.0 keV, and thus only the lower energy threshold matters for a calculation of a broad band X-ray luminosity. To give an example, in our model we find that the derived energy flux increases by $\sim 25\%$ if measured above 0.15 keV instead of 0.2 keV.

In 1979 a *Einstein* HRI (0.15–3.0 keV) observation (Golub et al. 1982) yielded X-ray luminosities of $1.2/2.8 \times 10^{27}$ erg s^{-1} for α Cen A/B, resulting in a B/A ratio of 2.3. A large number of individually short ROSAT HRI observations (~ 40) taken in 1996 indicated a B/A ratio varying between 2.0–3.5, excluding a probable flare event observed on α Cen B; X-ray luminosities (0.2–2.0 keV) were about 1.0–1.3/2.6–3.6 $\times 10^{27}$ erg s^{-1} for α Cen A/B (Schmitt & Liefke 2004). The more recent *Chandra* LETGS exposure (Raassen et al. 2003) taken in 1999 yielded luminosities for α Cen A/B of $0.9/1.6 \times 10^{27}$ erg s^{-1} in the energy range 0.15–4.0 keV with a B/A ratio of 1.9.

No variability of α Cen was reported for an *Einstein* IPC (4.5 h) and the *Chandra* (22.5 h) observation.

Only the March 2003 exposure of our XMM-Newton campaign has exhibited a comparable B/A ratio; in this observation we derive X-ray luminosities of $0.5/1.9 \times 10^{27}$ erg s^{-1} for α Cen A/B in the 0.2–2.0 keV band. The X-ray luminosity of α Cen B is thus comparable with previous measurements and no variations larger than a factor of two, which are already present within the different exposures of the XMM-Newton campaign, are found over a time interval of roughly 25 years. These findings support the scenario of a stable corona, where variations of the emission can be explained by a long-term activity cycle as indicated by emission line variability in IUE data (Ayres et al. 1995) covering roughly 10 years and short term activity in small surface areas that are additionally subject to rotational modulation. The period of this cycle, however, has to be long, probably ten or more years, while the relative modulation of the overall X-ray luminosity has to be much smaller than on the Sun to be consistent with the X-ray data.

But what about α Cen A? Although moderate short term variability also seems to be present, no indications were found for a long-term activity cycle so far. Comparing the derived X-ray luminosities, the values from the 1979–1999 observations differ by no more than 50% with the lowest value measured in 1999. With the March 03 exposure being already another 40% below the 1999 value, the X-ray output drops by more than a magnitude within two years. In the February 05 exposure (cf., Fig. 1) we can hardly recognise an X-ray binary at all, and the derived flux for α Cen A has declined to 2.5×10^{25} erg s^{-1}. We do point out that the decline in X-ray luminosity observed with XMM-Newton cannot be explained by a pure temperature effect. The assumption, that all of the X-ray emitting plasma has a temperature of only 1 MK with constant emission measure, results in a decrease of X-ray luminosity by a factor of two and is thus not sufficient to explain our XMM-Newton observations. Rather, a strong decrease of the total emission measure is necessary to explain our findings. While smaller differences in the long term evolution of X-ray luminosity may be explained by the use of the various instruments, the decline seen over the XMM-Newton campaign can only be explained by a X-ray activity cycle or an irregular event. While no definite statement can be made about an irregular event, the scenario of an activity cycle would require, that all previous X-ray measurements were made when α Cen A was near the "high state" of its cycle. Putting all the observation dates together, this would require a cycle with a duration of ~3.4 years from maximum to maximum. While chromospheric activity cycles on late-type stars were frequently found in Ca II H and K emission lines (Mt. Wilson S index) and periods of a few years are not uncommon (Baliunas et al. 1995), the α Centauri system was not observed in these programs due to its location in the southern sky. Further, the long term variability studies of IUE-UV lines mentioned above found no evidence for an activity cycle on α Cen A although some scatter in the data is present.

In the X-ray regime indications for coronal activity cycles were found in three other stars. Hempelmann et al. (2003) found evidence for coronal activity cycles in in both components of the K dwarf binary 61 Cygni; using ROSAT HRI data they determined X-ray luminosities for 61 Cygni A ($L_X = 1$–3×10^{27} erg s^{-1}) and 61 Cygni B ($L_X = 0.4$–1×10^{27} erg s^{-1}) that correlate well with the chromospheric activity as measured in the Ca II H+K, and recently, Favata et al. (2004) presented an analysis of the XMM-Newton data of the somewhat more active G2 star HD 81809 ($L_X = 2$–18×10^{28} erg s^{-1}), which also shows a drop in X-ray flux by more than an order of magnitude correlated with the Ca S index. On α Cen A long term X-ray variability is definitely present at a significant level, however the absence of comparative chromospheric activity data does not allow a correlation analysis and therefore only future observations will allow to check if an activity cycle is present on α Cen A, which would then be the first X-ray activity cycle on a true solar analog.

5. Conclusions

We have analysed five XMM-Newton observations of the α Centauri system regularly performed over two years and determined light curves and fluxes for the α Cen A (G2V) and B (K1V) components, which enables us to study short term behaviour as well as long term variability of the stellar activity of this system. The X-ray properties of both stars are characterized by a rather cool and inactive corona, but the system is found to be strongly dominated by the K star, α Cen B. The X-ray luminosity of α Cen B appears be variable within a factor of two and we are able to confirm its nature as a flare star. The observed flare on α Cen B is probably one of the weakest stellar flare events, where typical flare signatures like a well defined decay time were actually detected. A long term X-ray activity cycle on α Cen B, if present at all, has to be characterized by a long period and/or a small modulation.

For α Cen A we find a strong decline in X-ray luminosity by no less than an order of magnitude over the time span of our observations of two years, a behaviour that was never observed before on this star during observations performed over the last 25 years. This might then indicate a coronal activity cycle with all other observations having occurred – by chance – near the "high state" or – alternatively – an irregular event. The absence of long term chromospheric activity data for these stars make a definite statement on this point impossible. The observed trend of α Cen's X-ray luminosity is actually comparable to solar activity parameters as observed with the Yohkoh SXT in the 0.3–3.0 keV band. Acton (1996) studied changes of the solar X-ray emission from 1991 (near solar maximum) to 1995 (near solar minimum) and found that the average coronal temperature changed only by a factor of 1.5, i.e. from 3.3 MK to 1.9 MK, while emission measure declined by a factor larger than ten. A similar scenario would clearly explain the observed decline of α Cen A's X-ray brightness. The program is ongoing and future observations are scheduled to enlightened the nature of the coronal variability of our Sun's neighbouring twin.

References

Acton, L. W. 1996, ASP Conf. Ser., 109, 45

Anders, E., & Grevesse N. 1989, Geochim. Cosmochim. Acta, 53, 197

Arnaud, K. A. 1996, ASP Conf. Ser., 101, 17

Ayres, T. R., Fleming, T. A., Simon, T., et al. 1995, ApJS, 96, 223

Baliunas, S. L., Donahue, R. A., Soon, W. H., et al. 1995, ApJ, 438, 269

Ehle, M., Breitfellner, M., Gonzales Riestra, M., et al. 2003, XMM-Newton User's Handbook

Ehle, M., Pollock, A. M. T., Talavera, A., et al. 2004, User's Guide to XMM-Newton Science Analysis System

Favata, F., Micela, G., Baliunas, S. L., et al. 2004, A&A, 418, L13

Golub, L., Harnden, F. R., Jr., Pallacicini, R., et al. 1982, ApJ 253, 242

Grevesse, N., & Sauval, A. J. 1998, Space Sci. Rev., 85, 161

Hempelmann, A., Schmitt, J. H. M. M., Baliunas, S. L., Donahue, R. A. 2003, A&A, 406, L39

Pagano, I., Linsky, J. L., Valenti, J., & Duncan, D. K. 2004, A&A, 415, 331

Robrade, J., Ness, J.-U., & Schmitt, J. H. M. M. 2004, A&A, 413, 317

Raassen, A. J. J., Ness, J.-U., Mewe, R., et al. 2003, A&A, 400, 671

Schmitt, J. H. M. M., & Liefke, C. 2004, A&A, 417, 651

Smith, R. K., Brickhouse, N. S., Liedahl, D. A., & Raymond, J. C. 2001, ASP Conf. Ser., 247, 161

Chapter 8

X-ray activity cycles in stellar coronae

J. Robrade, J. H. M. M. Schmitt, A. Hempelmann and F. Favata
to appear in Proc. of The X-ray Universe 2005

1

X-RAY ACTIVITY CYCLES IN STELLAR CORONAE

J. Robrade[1]**, J.H.M.M. Schmitt**[1]**, A. Hempelmann**[1]**, and F. Favata**[2]

[1]Hamburger Sternwarte, Universität Hamburg, Gojenbergsweg 112, D-21029 Hamburg, Germany
[2]Astrophysics Division, ESA / ESTEC, Postbus 299, NL-2200 AG Noordwijk, The Netherlands

ABSTRACT

We present first results from the XMM-Newton monitoring program of solar-like stars; here we report on the binary systems α Cen A/B and 61 Cyg A/B. During the last years both targets were observed in snapshot like exposures separated roughly by half a year each. We are able to resolve both stellar systems and to determine the X-ray luminosities and respective emission measure distributions of the individual components. We also investigate physical changes in the coronae during variability and activity cycles. An X-ray darkening of α Cen A is observed during this program for the first time, probably indicating a coronal cycle. 61 Cyg A exhibits a continuation of its cyclic activity as discovered with ROSAT in the 1990s, making it the first persistent coronal activity cycle observed on a star other than the Sun.

Key words: X-rays, stars, coronae, activity.

1.   MONITORING THE TARGETS

α Cen is the nearest stellar system at a distance of 1.3 pc and we present six XMM-Newton observations of roughly two hours each, taken between 2003 – 2005. In all our observations the X-ray emission of the system is dominated by α Cen B, a K1V star. We investigate long-term variability and possible activity cycles of both stars and find the optically brighter component α Cen A, a G2V star very similar to our Sun, to have fainted in X-rays by at least an order of magnitude during the observation program. This behaviour was never observed before on α Cen A, but is rather similar to the X-ray behaviour observed with XMM-Newton on HD 81809 (Favata et al., 2004). Earlier spatially resolved observations of α Cen performed with *Einstein*, ROSAT and *Chandra* over the last 25 years always revealed a situation comparable to the beginning of our campaign in March 2003. We find that a coronal activity cycle with a duration of ~ 3.4 years matches all observations, but an irregular event cannot be ruled out due to the absence of long-term chromospheric activity data.

61 Cyg, a K5V (A) and a K7V (B) star at a distance of 3.5 pc, was observed with XMM-Newton during the years 2002 – 2005 and we obtained seven exposures with durations about two to four hours. We find a continuation of the coronal activity cycle on 61 Cyg A, which was discovered with ROSAT in the 1990s and found to be tightly correlated with the chromospheric activity as measured in CaII H+K (Hempelmann et al., 2003). 61 Cyg A is the first example of a persistent coronal cycle observed on a star other than the Sun. The component 61 Cyg B exhibits a more chaotic behaviour and a cycle can be identified only as long-term trend. Results derived from the ROSAT monitoring are included to extend the time-base of the X-ray measurements.

2.   DATA ANALYSIS

The data were reduced with the standard XMM-Newton Science Analysis System (SAS) software, version 6.0. Images, light curves and spectra were produced with standard SAS tools and standard selection criteria were applied for filtering the data. Spectral analysis was carried out with XSPEC V11.3.

The derived light curves of the program stars show variability on short timescales; flaring was observed on α Cen B, 61 Cyg A and strongest on 61 Cyg B. To investigate possible coronal activity cycles, only data from quasi-quiescent phases are considered, i.e., time periods free of strong activity or flares. To determine the X-ray brightness of our program stars, we use for α Cen a PSF (Point Spread Function) fitting algorithm which is applied to the event distribution in the sky-plane, while 61 Cyg is well resolved in the EPIC images which allows us to use individual extraction regions. X-ray luminosities are determined from spectral analysis, which uses multi-temperature APEC models and is performed in the energy range 0.2–5.0 keV, however, sufficient signal in quasi-quiescence is mostly present only up to 2.0 keV. Spectral analysis is performed for the α Cen system as a whole, but individual fits of spectra taken from small extraction regions around the respective component lead to comparable results for both components. Moreover, the determined X-ray luminosities L_X are nearly independent of the modelling details.

2
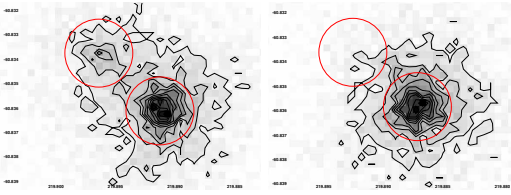
Figure 1. The α Cen system during March 2003 (left) and February 2005 (right); contours and 5″regions for the two components overlayed. Image creation is identical and the counts per image are comparable. The darkening of α Cen A at the upper left is striking and observed with XMM-Newton for the first time.
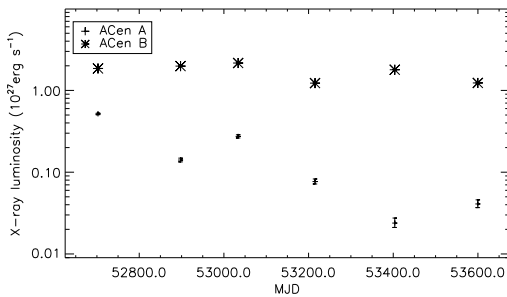
Figure 2. X-ray luminosity in the 0.2 – 2.0 keV band for α Cen A and B as determined from MOS1 data using PSF fitting algorithm and spectral modelling. Plotted errors are Poissonian derived from the PSF fitting.

3. ALPHA CENTAURI – THE DARKENING OF THE SOLAR TWIN

In Fig.1 we show two images of the system taken with the MOS1 detector during the March 2003 and the Feb. 2005 exposure. While the X-ray luminosity α Cen B is constant within a factor of two, a significant change, i.e. a strong dimming, is observed for α Cen A. To quantify these changes we determine the brightness of each component with a PSF fitting algorithm and subsequently its X-ray luminosity via spectral modelling.

In Fig. 2 we show the long-term light curve of α Cen A and B. The derived X-ray luminosities L_X (in 10^{27} erg/s) are given in Table 1 for the individual exposures. Spectral analysis shows both stars to have a rather cool (1.5 – 3 MK) and inactive corona with α Cen B being slightly hotter. The observed darkening of α Cen A is mainly due to a strong decrease in emission measure, comparable to the behaviour of the Sun as observed with Yohkoh (Acton, 1996). Comprehensive results including the data up to Feb. 2005 are published by Robrade et al. (2005).

Table 1. Derived X-ray luminosity for α Cen A/B.

Obs.	Mar. 03	Sept. 03	Jan. 04	July 04	Feb. 05	Aug. 05
L_X (A)	0.52	0.14	0.27	0.08	0.02	0.04
L_X (B)	1.86	1.98	2.16	1.22	1.79	1.23
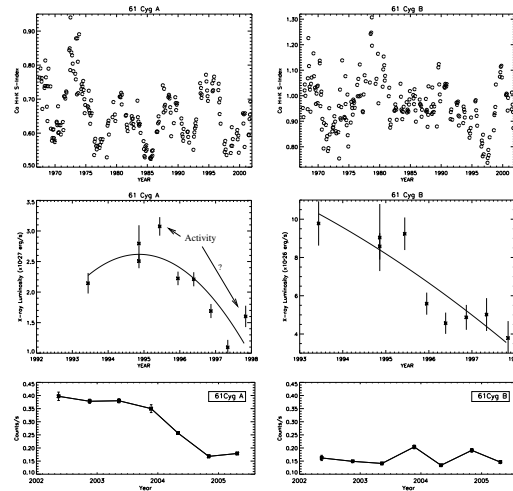
Figure 3. Long-term chromospheric activity up to 2001 (top) and ROSAT measurements (middle, from Hempelmann et al. (2003)) as well as preliminary results from the XMM-Newton program (bottom), here PN measurements (Robrade et al., in preparation) for 61 Cyg A (left column) and 61 Cyg B (right).

4. 61 CYGNI – THE PERSISTENT CORONAL CYCLE

In Fig. 3 we show that 61 Cyg A exhibits a very regular chromospheric activity cycle with a period of 7.3 years and a nearly symmetric rise and decay phase. Our X-ray measurements are well correlated and in phase with the previously observed cyclic activity as well as the ROSAT observations in the 1990s. In contrast, the chromospheric cycle of 61 Cyg B (11.7 yr) is more irregular, not symmetric and its activity index has a higher mean value. This is also reflected in its coronal behaviour. Although darker in X-rays, the corona is more active in the sense that flaring occurs more often and with larger amplitudes than on 61 Cyg A. Our X-ray light curve is rather constant and correlated variations are not detected over the three years. However, also in the ROSAT light curve as well as in chromospheric data, phases of rather constant activity are observed.

REFERENCES

Acton, L.W. 1996, ASP Conf. Series, 109, 45

Favata, F., Micela, G., Baliunas, S.L. et al. 2004, A&A, 418, L13

Hempelmann, A., Schmitt, J.H.M.M., Baliunas, S.L., Donahue, R.A., A&A, 406, L39

Robrade, J., Schmitt, J.H.M.M., Favata, F., 2005, A&A, in press

Chapter 9

Summary and outlook

9.1 Summary

In this thesis the X-ray properties of different types of cool stars have been investigated. Using data taken with instruments onboard XMM-Newton various aspects of stellar activity and mechanisms for X-ray generation were studied in several classes of the stellar population. The main aspects are (I) X-ray properties of active M dwarfs, (II) X-rays from classical T Tauri stars, (III) X-ray emission from Beta Pictoris and (IIII) Coronal activity cycles in solar-like stars.

I. X-ray properties of active M dwarfs

The X-ray properties of a sample of active M dwarfs with spectral type M3.5–M4.5 have been investigated in different states of activity. Light curves and spectra were analysed and a systematic study of its coronal properties with the different instruments onboard XMM-Newton was performed. Flare related changes of their coronal properties have been investigated and a comparison with other measurements was performed to check for long-term variations of their activity level. The results can be summarised as follows:

1. The X-ray properties of the investigated M dwarfs are quite similar, despite their different activity level. Concerning X-ray brightness and activity level, AD Leo, EQ Peg and EV Lac were found to be comparably active, while the probably younger object AT Mic was found to be X-ray brighter. All targets show frequent flaring and additional light curve variability on short timescales. Moderate flaring with brightness variations of factors 2–3 appear regularly on timescales of a few hours

while short-term behaviour is characterised by permanent flickering. A real quiescent phase was not observed during these observations.

2. The emission measure distribution covers a broad range of temperatures with a dominant cool component and a second hot component or tail. The cool component peaks around 7–8 MK, in the Sun these temperatures are observed only in flaring structures. A hotter component with temperatures of 25–30 MK is also present in quasi-quiescent phases. The derived coronal structures are compact, i.e. much smaller than a stellar radius. During flares the prominence of the hotter plasma components and temperatures, which exceed 50 MK, increase dramatically, in contrast the cool component is only marginally affected.

3. Coronal abundances of all investigated active M dwarfs show the inverse FIP-effect and its strength is correlated with activity. The overall metallicities are quite low compared to solar values, but appear to be consistent with measured stellar photospheric ones.

4. Long-term variations deduced from observations performed over decades with various missions are comparable to the variations already observed within our observations. This indicates a stable corona over theses timescales and the absence of strong cyclic behaviour for active M dwarfs.

5. The two components of binary system EQ Peg were separated for the first time in X-rays. It is shown that both components are flaring X-ray emitter with EQ Peg A being the X-ray

brighter star.

II. X-rays from classical T Tauri stars

The X-ray generating mechanisms in these objects are at least in detail still controversial. While coronal, i.e. magnetic, activity is clearly present in these stars, its underlying dynamo processes are only poorly understood. Recently accretion shocks were found to be an additional X-ray generating mechanism in CTTS. Several objects and their X-ray properties were studied with high and medium resolution spectroscopy. Especially the possibility of interpreting their X-ray properties as a superposition of coronal activity and magnetically funneled accretion and the relevance of these mechanisms in the individual objects is investigated. The derived results are:

1. Investigation of density sensitive lines in the spectra of BP Tau indicated that accretion shocks contribute to the X-ray emission of the cool plasma component. After TW Hya it is the second source, where observational evidence for the presence of magnetically funneled accretion in CTTS was found.

2. The derived plasma density in BP Tau is found to be even higher, when only quiescent phases are considered. This finding supports the accretion scenario but also indicates the presence of additional cool coronal plasma. The spectral hardening observed during the flare and the presence of a hot plasma component requires additional X-ray generating processes, i.e. the presence of magnetic activity.

3. Investigation of a sample of X-ray bright CTTS, i.e. BP Tau, CR Cha, SU Aur and TW Hya indicated the generation of X-rays via accretion shocks and coronal activity to be a common feature of CTTS in general, whereas the respective level and importance differs strongly between the objects.

4. The presence of accretional X-rays is deduced from density analysis. It revealed higher densities than observed in any pure coronal source in all targets, where the O VII triplet that is used for this study is observable. Only for the heavily absorbed target SU Aur this was

not possible. The observed frequent flaring accompanied by a spectral hardening and the detection of a hot ($> 10\,\mathrm{MK}$) component indicate the presence of coronal activity in all targets.

5. We find that accretional X-rays dominate only in the well known case TW Hya, in the other three targets most of the X-ray emission originates from the coronal contribution. This is reflected in the emission measure distributions of the targets and likewise supported by abundance analysis and investigation of spectral changes during periods of variable X-ray brightness.

III. X-ray emission from Beta Pictoris

The young A5V star Beta Pictoris is well-known for its circumstellar disk. Broad emission lines, e.g. from O VI, typical for chromospheres and transition regions were detected in UV, therefore it was observed with XMM-Newton and the following results were derived:

1. Weak X-ray emission from the O VII triplet is detected. This is the first detection of Beta Pictoris in X-rays.

2. Two scenarios are capable to explain this detection. Either a cool corona with temperatures around $0.6\,\mathrm{MK}$ is present, despite its early spectral type, or accreted material in a boundary layer generates the X-ray emission.

IIII. Coronal activity cycles in solar-like stars

The analysis of nearby, moderate to low activity G and K stars, i.e. stars with an activity level comparable to the Sun, is presented. Using data from the first years of a dedicated monitoring program, a search for possible coronal activity cycles analogue to the one observed on the Sun was performed for the two binary systems Alpha Centauri A/B and 61 Cygni A/B. Related physical changes in their coronae are investigated. The findings are:

1. The strong darkening observed for the Alpha Cen A indicates the presence of an activity cycle with short period. It is the first-time detection of this kind of variability at any wavelength for Alpha Cen A, therefore an irregular

event cannot be ruled out completely. Alpha Cen A (G2V) is a nearly perfect solar twin and an ideal object for comparison with the Sun. While the cycle length of $3-4$ years would be much smaller than the solar one, the amplitude and the spectral behaviour during the cycle are comparable to solar values. We find variations in X-ray luminosity of at least an order of magnitude, that are mainly caused by a strong decrease in emission measure and accompanied by a moderate decrease in average coronal temperature.

2. The star 61 Cyg A (K5V) exhibits a persistent coronal activity cycle in phase with the ROSAT measurements performed in the 1990s and the chromospheric activity measurements, which exhibit a smooth cycle with a period of roughly 7 years. Its cycle amplitude is with a factor of about three much smaller than for Alpha Cen A.

3. The more active stars of the respective systems, Alpha Cen B (K1V) and 61 Cyg B (K7V), exhibit no clear trend within the XMM-Newton observations and a rather constant X-ray luminosity. Their X-ray behaviour is characterised by stronger short term variability, they exhibit more frequent flaring and have higher coronal temperatures compared to the respectively other component. For 61 Cyg B chromospheric activity measurements reflect the X-ray properties and the more irregular cycle with a period of around 12 years is visible only as long-term trend.

9.2 Outlook

The new generation X-ray missions already provided plenty of new insights in the field of stellar coronal astronomy. The further investigation of stellar coronae will help to more precisely understand the details of coronal physics and stellar activity. Some important topics to mention in this context that can be addressed by systematic studies are dynamo theory, coronal heating mechanisms, coronal structures, time evolution of coronae or interaction with the stellar environment. Relevant information to answer these questions can of course also be obtained at other wavelengths and the broad-band study of stellar properties will probably lead to a more comprehensive understanding of stellar activity.

This thesis has presented results of several classes of cool stars and is based on observations of individual targets. These observations have the advantage of providing medium and high resolution spectroscopy combined with high sensitivity. The number of sources, even in the investigated samples of stars, is of course not very large due to limited available observing time. Beside large sample studies that are e.g. possible for clustered sources, future dedicated observations are essential to check whether and how the observed properties of a certain type of cool stars are distributed within its class or have to be attributed to individual targets. Further on, a comparison with a determination of coronal properties derived with different methods, i.e. global models vs. line measurements could test the robustness of derived results. Another point that has to be addressed are the accuracy of parameters that are used as model input. On the aspect of metallicities even the solar photospheric abundances are under discussion and stellar photospheric abundances of a larger sample would be highly desirable. Of general value would be for example also a more precise knowledge of underlying atomic data.

Considering activity at the end of the main sequence, systematic studies in a broader range of spectral types are possible. An interesting program could be devoted to the detailed investigation of stellar X-ray properties in even later types of M dwarfs. Refined analysis based only on well known, individual emission lines in high resolution X-ray spectra may lead to a more precise determination of the coronal parameters and their temporal changes e.g. during flares. This requires long duration exposures, providing the possibility of time-resolved high resolution spectroscopy. In the interesting regimes where stars are becoming fully convective these observations should yield valuable data that help to constrain e.g. dynamo models. This could also be addressed by comparing the X-ray properties of low-mass stars at the end of the main sequence and very young stars.

The origin of X-ray emission of young pre main-sequence stars is at least in detail still controversial. For these classes of sources likewise a larger sample of sufficiently long exposures would improve the

definiteness of the conclusions. Very interesting is also the investigation of X-ray active young stars of higher mass, i.e. Herbig Ae/Be stars.

The study of coronal activity cycles with periods of several years is naturally a long-term project. The here presented analysis of the 61 Cyg data is only preliminary and a refined analysis analogue to the one presented for Alpha Cen is in preparation. Our observation program is ongoing and future observations are scheduled to further study cyclic activity in the present sample. The sampling of at least one full activity cycle with XMM-Newton is favourable. The accumulation of observation time in a large number of snapshots will also allow to study the spectral properties of inactive stars in more detail.

Acknowledgements

I would like to thank a number of people for making my PhD possible, for their contributions to this work and for enjoyable times at the Hamburger Sternwarte.

First of all I want to thank my supervisor Prof. Jürgen Schmitt who provided me with excellent support and inspiring ideas throughout my work. With his spirit and his broad experience he is a fruitful source of enthusiasm and motivation.

Further I thank my collaborators Fabio Favata, Marc Hempel, Alexander Hempelmann, Jan-Uwe Ness and Beate Stelzer who contributed to the publications, gave valuable comments and shared their ideas. Thanks goes as well to the various referees who improved the publications, to the PIs of the observations and all other people involved in operating XMM-Newton for providing the data.

I thank my collaegues Birgit Fuhrmeister, Moritz Günther, Marc Hempel, Carolin Liefke, Jan-Uwe Ness, Ansgar Reiners, Christian Schröder, Rainer Wichmann and Uwe Wolter for discussion, help and having a nice time.

Additional thanks to Birgit Fuhrmeister for proof-reading parts of this thesis.

Greeting and thank goes to all people from the Hamburger Sternwarte, from various conferences, workshops and other scientific occasions for a lot of fun in the field.

Also thanks to my family and friends for everything.